1-1-2015

Helmholtz Equation Least Squares Based Near-Field Acoustic Holography With Laser

Wu Zhu
Wayne State University,

HELMHOLTZ EQUATION LEAST SQUARES BASED NEAR-FIELD ACOUSTIC HOLOGRAPHY WITH LASER

by

WU ZHU

DISSERTATION

Submitted to the Graduate School

of Wayne State University,

Detroit, Michigan

in partial fulfillment of the requirements

for the degree of

DOCTOR OF PHILOSOPHY

2015

MAJOR: MECHANICAL ENGINEERING

Approved By:

_____

Advisor Date

_____

_____

_____

ACKNOWLEDGEMENTS

First of all, I would like to express my deepest thanks and gratitude to my advisor, Prof. Sean Wu. It was really a privilege to have the opportunity to work and study under his mentorship. Only with all his guidance, support and encouragement, it became possible for me to go through this long journey and enjoy myself during the process.

My gratitude also goes to Profs. Trilochan Singh. I have served as a teaching assistant in Dr. Singh's course for more than two years. Dr. Singh's passion and devotion to his courses and students influenced me enormously. I am grateful for all his supports and care.

I also would like to express my appreciation to Dr. Wenlong Li. Thanks for offering me the opportunity to study in Wayne State University. Thanks Profs. Chin-An Tan for providing advice and guidance in my research and detailed instruction in vibration courses. Thanks Dr. Celiker and Dr. Xin Wu kindly serve as my committee member.

I also want to thank Dr. Na Zhu and Dr. Logesh Natarajan for all the help and instructions in my life and experimental preparation. Thanks are also extended to my friends: Yazhong Lu, Lingguang Chen, Shahram Amoozegar for their support and discussion, and departmental secretaries: Willis Rosalind and Marshall Kayla for their invaluable assistance.

Finally, I would like to thank my family for their unconditioned love and sacrifices, and all my friends for their company and support.

TABLE OF CONTENTS

LIST OF TABLES

LIST OF FIGURES

CHAPTER 1

INTRODUCTION

1.1 Motivation

Noise and vibration problems have been a hot topic in both academic and engineering communities for a long time. In order to identify and eliminate a noise source, different types of measuring tools such as microphones and intensity probes are used to measure various acoustic quantities such as sound pressure and sound intensity. However, the information thus acquired is limited to the measurement locations. The same quantities at other locations, especially on the source surface cannot be obtained. As a result, it is hard to obtain a big picture of the sound generation mechanisms and the distribution of acoustic radiation from the sound source to the surrounding fluid medium.

Near-field acoustic holography (NAH) is able to reconstruct all acoustic quantities such as the acoustic pressure, particle velocity and acoustic intensity when the measurements of acoustic pressure take place in the near field of a target sound source. NAH also offers an important insight of the interrelationship between acoustic output and structural vibration, and it can reveal the modal vibration patterns and deflection shapes of a vibrating structure via reconstructing the normal velocity on the surface of the vibrating source. As a result, NAH provides a tremendous amount of information the acoustic and vibration characteristics of a sound source [1-5]. NAH attempts to capture as much near-field effects, namely the evanescent waves radiated by the sound source as possible. By including the near-field effects in the reconstruction process, NAH can yield an accurate reconstruction with high spatial resolution. When a vibrating structure surface is radiating sound waves, there are two different kinds of

waves produced: plane waves and evanescent waves. In the case of the wavelength of the structural waves on the surface being longer than the acoustic wavelength, sound plane waves takes a dominant percentage and radiates away from the vibrating structure. On the other hand, evanescent waves are the main parts with the wavelength of the structural waves shorter than the acoustic wavelength in air. Evanescent waves do not propagate effectively since their amplitude decay exponentially with respect to the distance from vibrating structure surface, and then no energy is delivered into far field [6-9].

NAH, theoretically, can overcome the limitation of wavelength resolution and obtain unlimited spatial resolution by capturing all the evanescent waves. Then, the experiment setups such as measurement distance and microphone spacing of the microphone array need to be smaller than half of the critical structural wavelength. In practice, however, such a requirement is hard to satisfy since the structural wavelengths can go to very small values which makes the microphone array is unrealistic to make [9-11]. In its original formulation, NAH was implemented by the Fourier transform [2, 3, 12]. The Fourier transform based NAH is highly attractive for its simplicity to implement, speed of calculation and accuracy of reconstruction. However, the Fourier transform based NAH is only applicable to source surfaces with separable geometry such as planar, cylindrical or spherical surfaces. Fourier transform based NAH becomes restrictive when it is applied to the field is generated by sources of arbitrarily-shaped geometry or by several spatially separated structures.

Instead of trying to obtain an analytic reconstruction of acoustic field, Helmholtz Equation Least Squares (HELS) seeks an approximate solution of acoustic field [13]. HELS based NAH utilizes a basis of spherical wave functions to do a least-squares fitting of the acoustic pressure measured by the hologram microphone array, and it is able to reconstruct the

acoustic field with much less measurements [14, 15]. Expansion coefficients of basis functions are decided by matching the reconstructed pressure with the measured value on selected positions. Least-squares method is adopted to find out the optimal number of expansion terms. Then, sound filed quantities could be reconstructed by using the same set of expansion coefficients. The sound field at other interested positions can be reconstructed either via forward propagation towards the far field or back propagation towards surfaces of the source. More importantly, HELS based NAH is able to reconstruct the vibro-acoustic response generated by sources with complex geometry and the error is limited by the least-squares process and regularization techniques.

Most of near-field holography theories rely on the acoustic pressure measurements exclusively on a hologram surface. Researchers and engineers get used to use sound pressures as input since the experiment setup and instruments for sound pressure measurement are straightforward. However, building a conformal array of microphones to attain accurate sound pressure measurements in the near field is not an easy task in practice. In recent years, laser Doppler vibrometer (LDV) turns out to be an effective and efficient technique to measure the normal surface velocity directly on source surface [16-19]. The primary objective of this thesis is to develop a modified NAH method: HELS based NAH with laser and to demonstrate that NAH can be based on normal surface velocity measurements using LDV instead of conventional acoustic pressure measurements. HELS method was selected over Fourier transform based NAH or other NAH techniques since it lifts the restriction of hologram requirement and it can be used to reconstruct sound field on any arbitrarily shaped source. Numerical simulation and Experiments will be conducted to examine the potential advantages of measurement principles and accuracy of this modified HELS based NAH method.

1.2 Structure of the thesis

The structure of this dissertation can be summed as follows:

Ch. 2 illustrates a detailed literature review of two typical NAH methods: Fourier transform based NAH and HELS based NAH. The theoretical knowledge and working principles of both methods are introduced. Simulation studies based on simple examples are also represented.

Ch.3 provides theoretical background of the HELS based NAH with laser. Two examples including a dilating sphere and an oscillating sphere show that HELS based NAH with laser is able to obtain the exactly same acoustic pressure as theoretical solutions. Moreover, error analysis is employed to demonstrate that the reconstruction error is bounded and HELS based NAH with laser is robust and reliable.

Ch.4 shows the simulation results about different ideal sound sources to validate the modified NAH method. Also, different simulation environments are explored to prove its capability. The impacts of reconstruction distance and expansion terms are studied.

Ch.5 tests several different regularization techniques since the sound field reconstruction is a severely ill-posed problem. The comparison and time-cost analysis are conducted to find out the proper regularization algorithm for HELS based NAH with laser.

Ch.6 uses the experimental results to verify the modified NAH method. The working principles of a LDV are introduced. Also, the experiment setup is explained in detail.

Ch.7 draws the conclusions of the work has been done in this thesis and possible future directions of research are also presented.

CHAPTER 2

LITERATURE REVIEW

Over the past three decades, there have been different theories and methodologies developed to implement NAH. This chapter aims to offer a detailed literature review on two typical NAH techniques: Fourier transform based NAH and HELS based NAH. Simulation studies are conducted to explore the process of NAH methods in sound field reconstruction.

2.1 Fourier transform based NAH

2.1.1 The development of Fourier transform based NAH

NAH is a powerful sound source identification tool and noise diagnostics technique. The sound pressure radiations of a point source and a center-driven rectangular plate were reconstructed using NAH and compared with theoretical values [20, 21]. In a subsequent paper, Earl G. Williams and J. D. Maynard fully illustrated the capability of NAH to exploit the fundamental principles of holography and offered detailed instructions for experimental implementation [22].

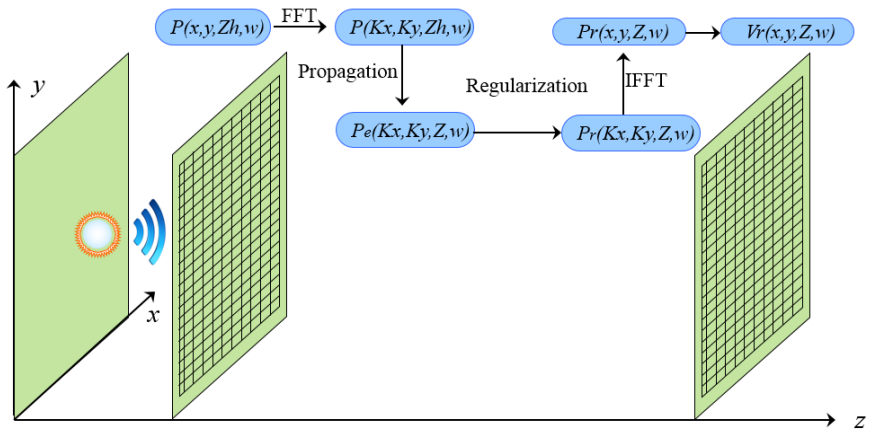

Figure 2.1 Diagram of NAH

To deal with noise sources with cylindrical shapes, Earl G. Williams and Henry D. Dardy further developed the planar NAH theory into the so-called generalized near-filed acoustic holography (GENAH). Correspondingly, the relationship between the location of conformal measurement surface and the desired reconstruction spatial resolution was given. Therefore, it was possible to reconstruct sound field for a cylindrical structure with super resolution under the guidance [23]. The application of GENAH was extended to broadband excitation of cylindrical structures and it circumvented the workloads of deploying different highly dense measurement grids for each interested frequency. An experiment of global reconstruction of sound field of an underwater cylinder was conducted to validate the GENAH [24, 25]. Another significant improvement of NAH was achieved by Giorgio V. Borgiotti et al in 1990. They applied NAH on reconstructing the normal surface velocity of an axisymmetric shell. Since the curved target cannot be represented by a separable coordinate system, normal NAH was failed to obtain satisfying reconstruction results. Instead, a conformal measurement grid was placed as close as possible to the source and a least mean square algorithm based on Singular Value Decomposition (SVD) was adopted to deal with the inverse transfer function. As a result, the boundary normal velocity field of the axisymmetric surface was attained with a fine spatial resolution [26]. Subsequently, the energy exchange between a cylindrical shell and acoustic radiation was studied, and the radiation pattern was observed and analyzed in time domain [27]. Tomlinson broadened the application range of NAH into discriminating partial source [28].

More than often the real NVH problems have more than one noise source, then it is very necessary to figure out the contribution of each source. Kyoung-Uk Nam and Yang-Hann Kim applied NAH on visualization and contribution analysis of multiple incoherent sources with no prior knowledge on source positions. A numerical study of two incoherent monopoles was

conducted to demonstrate the effectiveness of NAH in dealing with multiple sources condition [29].

Most of NAH only consider the acoustic radiation in a homogeneous and stationary medium. However, when the environment has been changed into a moving medium, a wave number Doppler Effect will emerge and the conventional NAH will have a significant error in reconstruction results. Ruhala and Swanson extended the application range of planar NAH by modifying the wave number. Different cases with different flow directions were discussed in detail. Also, the influence of velocity of flow was checked using several sets of numerical analysis examples [30]. For spherical acoustic radiation problems, J.C. Lee presented a spherical acoustic holography method and applied it to reconstruct acoustic radiation problem in low frequency range. The separation of variables method was used in solving wave equation in spherical coordinate system. The harmonic coefficients were determined under a group of orthogonal functions, and then the set of coefficients could be used for both prediction problems and reconstruction issues [31, 32].

NAH requires the aperture be infinite theoretically. Otherwise, wraparound errors would be introduced in calculation [33]. To alleviate the wraparound errors, the measurements need to be taken on a very large hologram surface. NAH is cumbersome to be applied on a large size vibrating structure. A new type of modified NAH named patch NAH loosened the requirement of complete surface measurement from conventional NAH. The analytic continuation of the patch pressure enabled patch NAH to only take measurements on interested parts of surface. To deal with the inverse process of NAH, the SVD was used for the transfer function connecting source surface and measurement surface. Subsequently, Patch NAH was applied for cylindrical cases [34-37].

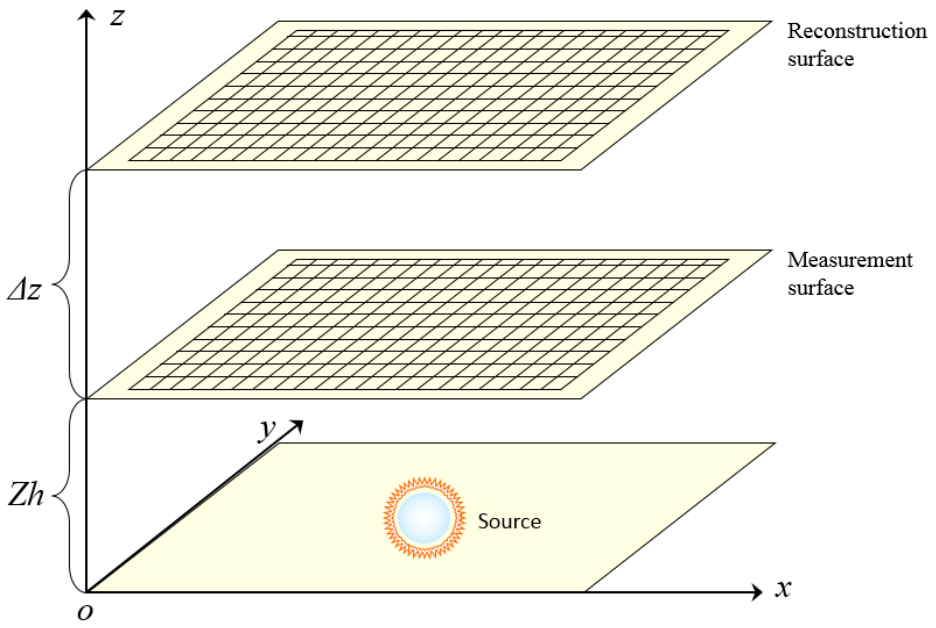

Figure 2.2 Positions of measurement and reconstruction planes

2.1.2 Numerical simulations of Fourier transform based NAH

The following is the algorithm of the Fourier transform based near-field acoustic holography.

The measurement grid is defined as follows:

(a) Number of microphones in the x-axis direction: N_x (N_x is an even number and a power of 2, for example, N_x = 32.)

(b) Microphone spacing in the x-axis direction: Δx

$$\Delta x = \frac{L_x}{N_x} \tag{2.1}$$

where L_x is the total length of microphone array in x axis. Once the number of microphones and microphone spacing in the x axis direction are selected, the total length of the microphone array in the x axis direction is set.

(c) Number of microphones in the y-axis direction: N_y (N_y is an even number and a power of 2, for example, N_y= 32.)

(d) Microphone spacing in the y-axis direction: Δy

$$\Delta y = \frac{L_y}{N_y} \tag{2.2}$$

where L_y is the total length of microphone array in y axis. Once the number of microphones and microphone spacing in the y axis direction are selected, the total length of the microphone array in the y axis direction is set.

(e). Difference in distances $\Delta z = z - zh$ between the hologram plane *zh* and any plane *z*. A negative value of Δz indicates moving toward the source, whereas a positive value of Δz implies moving away from the source. Note that the Fourier transform based NAH is valid in a source-free region. Hence the reconstruction plane must be in the region $\Delta z > -zh$.

The acoustic pressures are measured on the hologram plane at *zh.* In numerical simulations, the acoustic pressure on a hologram surface may be generated by, say, a point source.

$$\hat{p}(x, y, z_h; \omega) = -i \frac{\rho_0 c k \hat{Q}_s e^{ikR_h}}{4\pi R_h} \tag{2.3}$$

where $\hat{Q}_s$is the source strength and a constant, $R_h = \sqrt{(x - x_1)^2 + (y - y_1)^2 + (z - z_1)^2}$ is the distance between the source at (x_1, y_1, z_1) and receiver on a hologram surface (x, y, z_h), k is the acoustic wave number $k = \frac{\omega}{c}$, c is the speed of sound (c=343 *m/s*), ω is the angular frequency $\omega = 2\pi f$, where f is the frequency that is specified in the input. When reconstruction is conducted on the source plane, there is a singularity at position (0, 0, 0). In order to circumvent this difficulty in numerical simulations, reconstruction should be performed on a plane at z >0. However, this singularity difficulty does not exist in practice.

The spatial Fourier transform of the acoustic pressure is used to find the angular spectrum of the acoustic pressure measured on z_h plane. The Fourier based NAH formula is listed as below [38]:

$$P\left(k_x, k_y, z_h;\ \omega\right) = \int_{-\frac{L_x}{2}}^{\frac{L_x}{2}} \int_{-\frac{L_y}{2}}^{\frac{L_y}{2}} \hat{p}(x, y, z_h; \omega) H(x, y) e^{-i\left(k_x x + k_y y\right)} dx dy \tag{2.4}$$

where $\hat{p}(x, y, z_h; \omega)$ represents the acoustic pressure measured on the hologram surface z_h, $H(x, y)$ is the spatial window designed to minimize the impact of a finite measurement aperture on reconstruction results.

$$H(x, y) =$$

$$\begin{cases} 1, (|x| \le \frac{L_x}{2} - W_x)\ and\ (|y| \le \frac{L_y}{2} - W_x) \\ \frac{1}{4}\{1 - cos\left[\frac{\pi\left(x - \frac{L_x}{2}\right)}{W_x}\right]\}\{1 - cos\left[\frac{\pi\left(y - \frac{L_y}{2}\right)}{W_y}\right]\}, (\frac{L_x}{2} - W_x < |x| < \frac{L_x}{2})\ or\ (\frac{L_y}{2} - W_y < |y| < \frac{L_y}{2}) \\ 0, (|x| \ge \frac{L_x}{2})\ or\ (|y| \ge \frac{L_y}{2}) \end{cases}$$

(2.5)

where Δx and Δy are the step sizes in the x and y axis directions respectively; W_x and W_y are the side lengths of the aperture.

The spatial wave number k_x is $k_x = n_x \Delta k_x$ and $\Delta k_x = \frac{2\pi}{\Delta x N_x}$. Similarly, $k_y = n_y \Delta k_y$ and $\Delta k_y = \frac{2\pi}{\Delta y N_y}$. Eq. (2.4) can be evaluated by using discrete Fourier transform for programming.

$$P\left(n_x \Delta k_x, n_y \Delta k_y, z_h;\ \omega\right) = \Delta x \Delta y \times$$

$$\left(\sum_{m_x=-\frac{N_x}{2}}^{\frac{N_x}{2}-1} \sum_{m_y=-\frac{N_y}{2}}^{\frac{N_y}{2}-1} \hat{p}\left(m_x \Delta x, m_y \Delta y, z_{h;} \omega\right) H\left(m_x \Delta x, m_y \Delta y\right) e^{-\frac{i2\pi n_x m_x}{N_x}} e^{-\frac{i2\pi n_y m_y}{N_y}}\right) \tag{2.6}$$

The angular spectrum at any other plane z is reconstructed through multiplying the angular spectrum at $z_h$by the propagator.

$$P(k_x, k_y, z;\ \omega) = P(k_x, k_y, z_h;\ \omega)e^{-ik_z\Delta z} \tag{2.7}$$

where Δz is the difference in distance between the hologram plane $z_h$and a reconstruction plane z, which is specified in the input, and k_z is given by

$$k_z = \sqrt{k^2 - ({k_x}^2 + {k_y}^2)} \tag{2.8}$$

if $k^2 > ({k_x}^2 + {k_y}^2)$, $k_z = \sqrt{k^2 - ({k_x}^2 + {k_y}^2)}$ is real. If $k^2 < ({k_x}^2 + {k_y}^2)$, $k_z = i\sqrt{({k_x}^2 + {k_y}^2) - k^2}$ will be purely imaginary, and the amplitude of the angular spectrum will decay exponentially (evanescent waves) when Δz is positive; or increase exponentially (the near-field effects) when Δz is negative.

The reconstructed acoustic pressure on z plane is obtained by taking the inverse spatial Fourier transform of the angular spectrum in frequency domain.

$$\hat{p}(x, y, z; \omega) = \frac{1}{4\pi^2}\int_{-k_{max,x}}^{+k_{max,x}}\int_{-k_{max,y}}^{+k_{max,y}} P(k_x, k_y, z; \omega)W(k_x, k_y)e^{i(k_x x + k_y y)}dk_x dk_y \tag{2.9}$$

where $W(k_x, k_y)$ is the k-space filter designed to minimize the impact of high wave numbers due to the sharp cutoffs of the acoustic pressures on the edges of a measurement aperture.

$$W(k_x, k_y) = \begin{cases} 1 - \frac{1}{2}e^{\frac{(1-\frac{|k_x|}{k_{cr,x}})}{\alpha}} \times e^{\frac{(1-\frac{|k_y|}{k_{cr,y}})}{\alpha}}, |k_x| < k_{cr,x}\ and\ |k_y| < k_{cr,y} \\ \frac{1}{2}e^{\frac{(1-\frac{|k_x|}{k_{cr,x}})}{\alpha}} \times e^{-\frac{(1-\frac{|k_y|}{k_{cr,y}})}{\alpha}}, |k_x| \geq k_{cr,x}\ and\ |k_y| < k_{cr,y} \\ \frac{1}{2}e^{-\frac{(1-\frac{|k_x|}{k_{cr,x}})}{\alpha}} \times e^{\frac{(1-\frac{|k_y|}{k_{cr,y}})}{\alpha}}, |k_x| < k_{cr,x}\ and\ |k_y| \geq k_{cr,y} \\ \frac{1}{2}e^{\frac{(1-\frac{|k_x|}{k_{cr,x}})}{\alpha}} \times e^{\frac{(1-\frac{|k_y|}{k_{cr,y}})}{\alpha}}, |k_x| \geq k_{cr,x}\ and\ |k_y| \geq k_{cr,y} \end{cases} \tag{2.10}$$

where α=0.05~0.1. $k_{cr,x}$ and $k_{cr,y}$ are given by

$$k_{cr,x} = \frac{4\pi}{5\Delta x} \text{ and } k_{cr,y} = \frac{4\pi}{5\Delta y} \tag{2.11}$$

For the convenience of programming, Eq. (2.9) can be evaluated by using discrete Fourier transform.

$$\hat{p}(m_x\Delta x, m_y\Delta y, z;\ \omega) = \frac{1}{N_x N_y \Delta x \Delta y} \times$$

$$\left(\sum_{n_x=-\frac{N_x}{2}}^{\frac{N_x}{2}-1} \sum_{n_y=-\frac{N_y}{2}}^{\frac{N_y}{2}-1} P(n_x\Delta k_x, n_y\Delta k_y, z_h;\ \omega) W(n_x\Delta k_x, n_y\Delta k_y) e^{ik_z\Delta z} e^{\frac{i2\pi n_x m_x}{N_x}} e^{\frac{i2\pi n_y m_y}{N_y}}\right) \tag{2.12}$$

The particle velocity on the z plane can be reconstructed by

$$\hat{v}(m_x\Delta x, m_y\Delta y, z;\ \omega) = \frac{1}{\rho_0 ck N_x N_y \Delta x \Delta y} \times$$

$$\left(\sum_{n_x=-\frac{N_x}{2}}^{\frac{N_x}{2}-1} \sum_{n_y=-\frac{N_y}{2}}^{\frac{N_y}{2}-1} k_z P(n_x\Delta k_x, n_y\Delta k_y, z_h;\ \omega) W(n_x\Delta k_x, n_y\Delta k_y) e^{ik_z\Delta z} e^{\frac{i2\pi n_x m_x}{N_x}} e^{\frac{i2\pi n_y m_y}{N_y}}\right) \tag{2.13}$$

where ρ_0 is the ambient density of the air. The acoustic intensity can then be calculated as

$$\hat{I}(x, y, z;\ \omega) = \frac{1}{2} Re[\hat{p}(x, y, z;\ \omega) \times \hat{v}_z^*(x, y, z;\ \omega)] \tag{2.14}$$

where $\hat{v}_z^*(x, y, z;\ \omega)$implies the complex conjugate of particle velocity.

To validate of NAH formulations, the reconstructed sound filed quantities including acoustic pressure, particle velocity and sound intensity are compared with the theoretical values at the same coordinates. Two examples including point sound source and dipole sound source are simulated.

The size of measurement surface is 40×40 *mm*, and then the number of microphones is set as 32 in both *x* and *y* axis directions. Correspondingly, microphone space is decided as 0.0125 meter in both *x* and *y* axis directions.

Example 1: Consider the acoustic pressure field generated by a monopole using Eq. (2.3). Next, use Eq. (2.6) to produce the angular spectrum at any plane in a source-free region, followed by Eq. (2.12) to reconstruct the acoustic pressure on this plane. The results are compared with those given by

$$\hat{p}(x, y, z + z_h;\ \omega) = -i\frac{\rho_0 ck\hat{Q}_s e^{ikR}}{4\pi R} \tag{2.15}$$

where $R = \sqrt{(x - x_1)^2 + (y - y_1)^2 + (z + z_h - z_1)^2}$. The particle velocity can be reconstructed by Eq. (2.13) and the results are compared with those given by

$$\hat{v}_z(x, y, z + z_h;\ \omega) = \frac{(\Delta z + z_h)\hat{Q}_s e^{ikR}}{4\pi R^2}(1 - ikR) \tag{2.16}$$

Finally, we can use Eq. (2.14) to reconstruct acoustic intensity and compare the result with the theoretical value given by

$$\hat{I}_{av,z}(x, y, z_h + \Delta z;\ \omega) = \frac{\rho_0 ck^2|\hat{Q}_s|^2}{32\pi^2 R^3} \tag{2.17}$$

Figure 2.3 shows the pressure is obtained on measurement plane *Zh*, and these measurements will be used as input for reconstruction process.

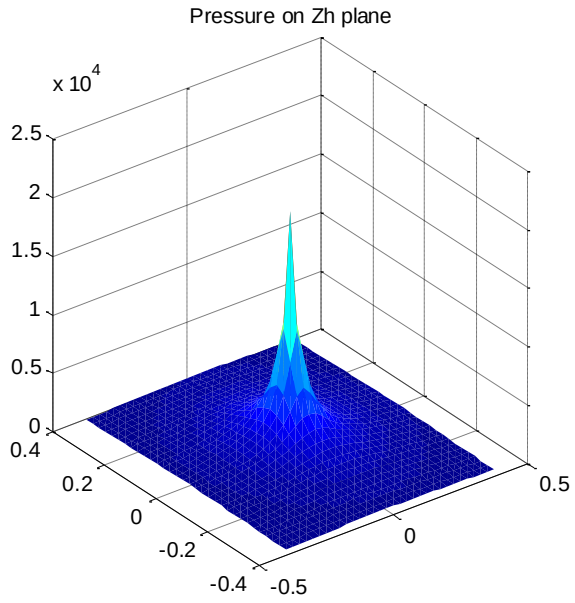

Figure 2.3 Acoustic pressure on measurement surface by a monopole

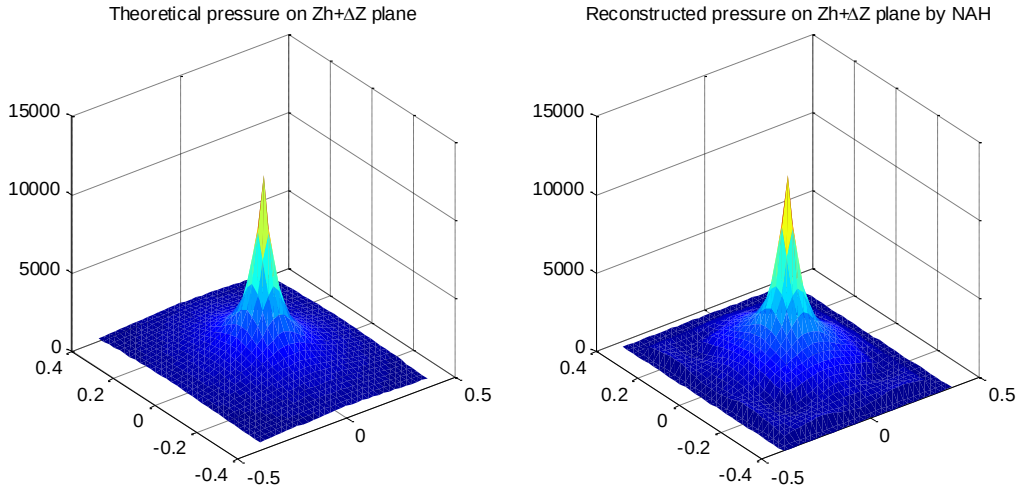

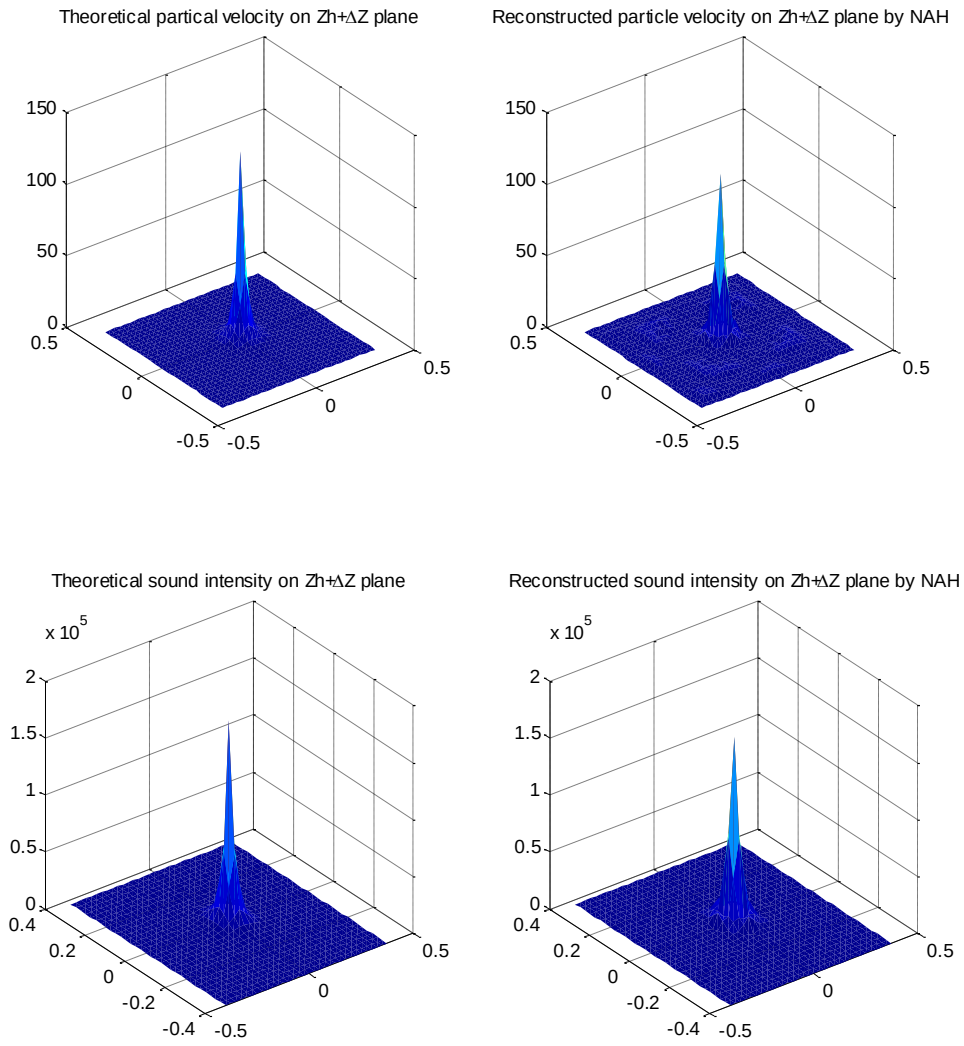

Figure 2.4 Analysis of reconstructed sound field generated by a monopole using Fourier based NAH

Example 2: Consider the acoustic pressure field generated by a dipole along the x-axis:

$$\hat{p}(x, y, z + z_h;\ \omega) = -k^2\left(1 + \frac{i}{kR}\right)\frac{\rho_0 c(\hat{Q}_s d)e^{ikR}}{4\pi R} \tag{2.18}$$

where *d* is the distance between two monopoles of opposite signs.

Eq. (2.18) is used to obtain the input data with $\Delta Z = 0$ and then Eq. (2.12) is used to reconstruct the acoustic pressure on a plane in the source free region. The results should be

compared with those at any ($Zh + \Delta Z$). Next we can use Eq. (2.13) to reconstruct the particle velocity and compare them with those given by

$$\hat{v}_{z(x,y,z+z_h;\,\omega)} = \frac{-k^2(\hat{Q}_s d)e^{ikR}}{4\pi R}\left[1 + \frac{2i}{kR} - \frac{2}{k^2R^2}\right] \tag{2.19}$$

Similarly, we can use Eq. (2.14) to reconstruct acoustic intensity and compare the results with those given by theoretical results. Figure 2.5 shows the pressure is obtained on measurement plane *Zh*, and these measurements will be used as input for reconstruction process.

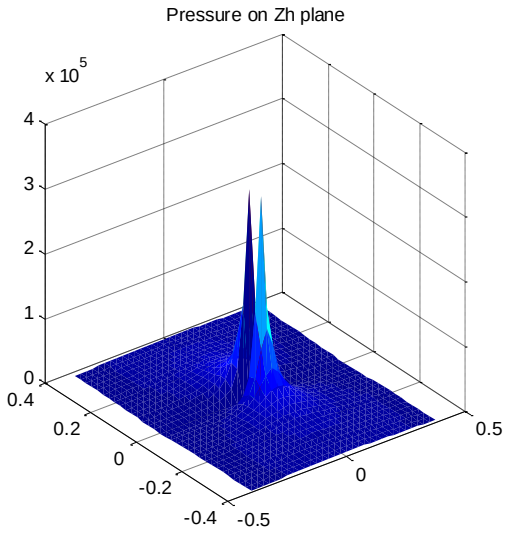

Figure 2.5 Acoustic pressure on measurement surface by a dipole

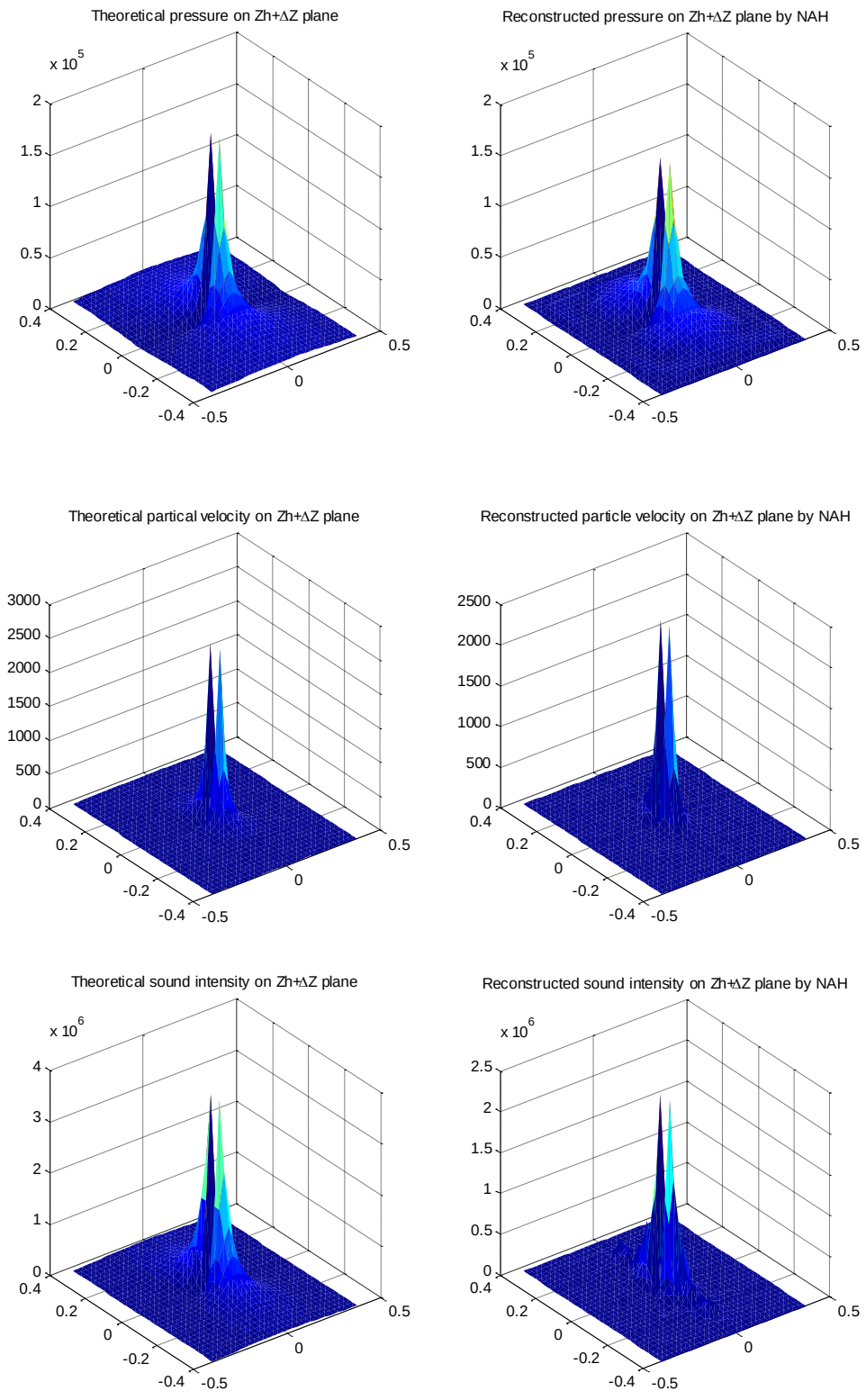

Figure 2.6 Analysis of reconstructed sound field generated by a dipole using Fourier based NAH

2.2 HELS based NAH

2.2.1 The development of HELS based NAH

Instead of looking for analytic solutions for Helmholtz equation, HELS innovatively solves the Helmholtz equation by approximate approaches. The acoustic pressure is presented as the summation of a series of spherical wave functions generated by the Gram-Schmidt orthonormalization. Sound pressure is measured on a measurement hologram with respect to the vibrating source. Then, the coefficients correlated with the spherical basis functions can be determined by minimizing the errors between the approximate solutions and the measured pressure. The flexibility and efficiency of HELS is outstanding compared with other NAH methods [13, 39].

The capability of HELS was extended further into reconstructing acoustic pressure field inside the cavity of a vibrating body. HELS was used to reconstruct sound pressure radiated by a vibrating cylinder with different aspect ratios, then it has been demonstrated that HELS could get satisfactory reconstruction results both in interior and exterior fields. Also, there was no restriction on the shape of vibrating sources, and HELS was eligible to yield relatively accurate results even for non-spherical or elongated objects [40].

An experiment was conducted on the structure with similar geometry to a real passenger vehicle. The reconstructed acoustic pressures from HELS method was compared with measured values on a planar grid. Also, this experiment testified the importance to find an optimal number of expansion terms which could be used to secure the reconstruction accuracy [41]. Another test was done for a full size four cylinders engine to examine the effectiveness of HELS method when it dealt with a complex structure. The comparison of reconstructed acoustic pressure with

the results from Boundary Element Method (BEM) demonstrated that HELS method could finish the sound field reconstruction of complex structures with a high accuracy [42].

Three different expansion functions including localized spherical waves, distributed spherical waves and distributed point sources were discussed under the same experimental test. Also, the impacts of locations of auxiliary surfaces, regularization methods and penalty functions were discussed. Distributed spherical waves were the best choice for HELS method to stay robust and get highly accurate reconstruction results over a wide range of frequency [43]. As a consecutive research project, the interrelationship between HELS method with the Rayleigh Hypothesis was investigated. The necessary number of measurements was dependent on the validity of the Rayleigh hypothesis. Only a few measurements were needed once the Rayleigh hypothesis was valid. Otherwise, the number of measurements should be at least twice of the expansion order [15].

A combined HELS method was presented for reconstructing acoustic field from an arbitrarily shaped object. HELS method was used to generate acoustic pressures as the input for BEM [44]. Subsequently, the HELS method was mathematically justified by proving that the errors in reconstruction process were bounded. Experiment using an office filing cabinet demonstrated that HELS method worked well for a highly non-spherical surface with limited errors [45]. A hybrid NAH based on HELS method was introduced by way of expressing acoustic pressure using incoming and outgoing waves. The experiment studies were conducted both in a free and confined field [46]. Numerical studies on reconstructing the vibro-acoustic field of an engine block and a highly elongated cylinder demonstrated that hybrid NAH based on HELS could serve as a great diagnostic tool [47]. Furthermore, a modified HELS was developed to reconstruct acoustic field on the surface of a vibrating body in half space [48].

An experiment study was conducted to reconstruct the structure-borne sound responses on a small scale model of the automobile passenger compartment. A shaker was used to excite the structure. The linear microphone array measured near field sound pressure following the geometry contour of the model. The HELS method took the measured acoustic pressure as input to reconstruct the sound field. The contributions of the individual panels over the frequency spectrum were analyzed. The major contributor of sound pressure level at occupant's ear position was decided [51]. HELS method was employed to reconstruct normal surface velocity and operational deflection shapes of a baffled thin steel plate. The reconstructed operational deflection shapes were decided including the first 18 flexible natural modes of the plate. It presented that HELS method could work as an effective tool to identify the critical panels causing noise radiation [52-54].

2.2.2 Numerical study of HELS

Aiming to get an approximate solution of Helmholtz equation, acoustic pressure from a sound source is expressible as an expansion of the spheroidal functions. Therefore, the radiated acoustic pressure can be presented mathematically as follows:

$$\hat{p}(x;w) = \sum_{j=1}^{J} C_j \Psi_j(x;w) \tag{2.20}$$

$\hat{p}$: the complex amplitude of acoustic pressure;

J : number of expansion terms;

Ψ_j: basis functions that are particular solutions to the Helmholtz equation;

C_j : the coefficients associated with basis functions Ψ_j.

From Eq. (2.20), the associated coefficients can be solved as:

$$\{C(w)\}_{J\times 1} = [\Psi_j(x_m; w)]^{\dagger}_{J\times M}\{\hat{p}(\vec{x}_m^{meas}; \omega)\}_{M\times 1} \tag{2.21}$$

where $[\Psi_j(x_m; w)]^{\dagger}_{J\times M}$ is the pseudo inversion of basis functions. Similarly, the expansion functions are calculated at reconstruction positions. Then, the reconstructed pressure can be obtained as follows:

$$\hat{p}(x_r; w)_{M\times 1} = [\Psi(x_r; w)\Psi_j(x_m; w)^{\dagger}]_{M\times M}\{\hat{p}(\vec{x}_m^{meas}; \omega)\}_{M\times 1} \tag{2.22}$$

By way of Euler's equation, the particle velocity can be obtained immediately.

$$\hat{v}(x_r; w)_{M\times 1} = \frac{1}{iw\rho}[\frac{\partial\Psi(x_r;w)}{\partial n}\Psi_j(x_m; w)^{\dagger}]_{M\times M}\{\hat{p}(\vec{x}_m^{meas}; \omega)\}_{M\times 1} \tag{2.23}$$

Accordingly, the acoustic intensity can be calculated using Eq. (2.14).

The same examples and numerical test setup are used as shown in section 2.1.2.

Example 1: acoustic fields generated by a monopole sound source

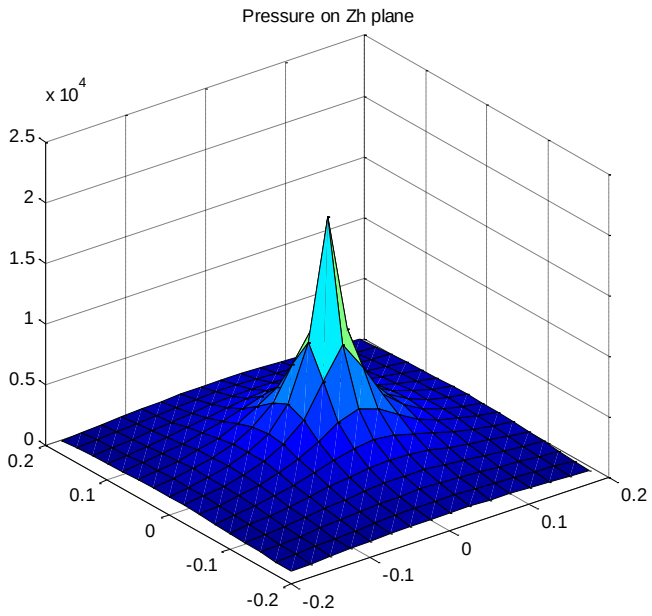

Figure 2.7 Acoustic pressure on measurement surface of a monopole as input for HELS based NAH

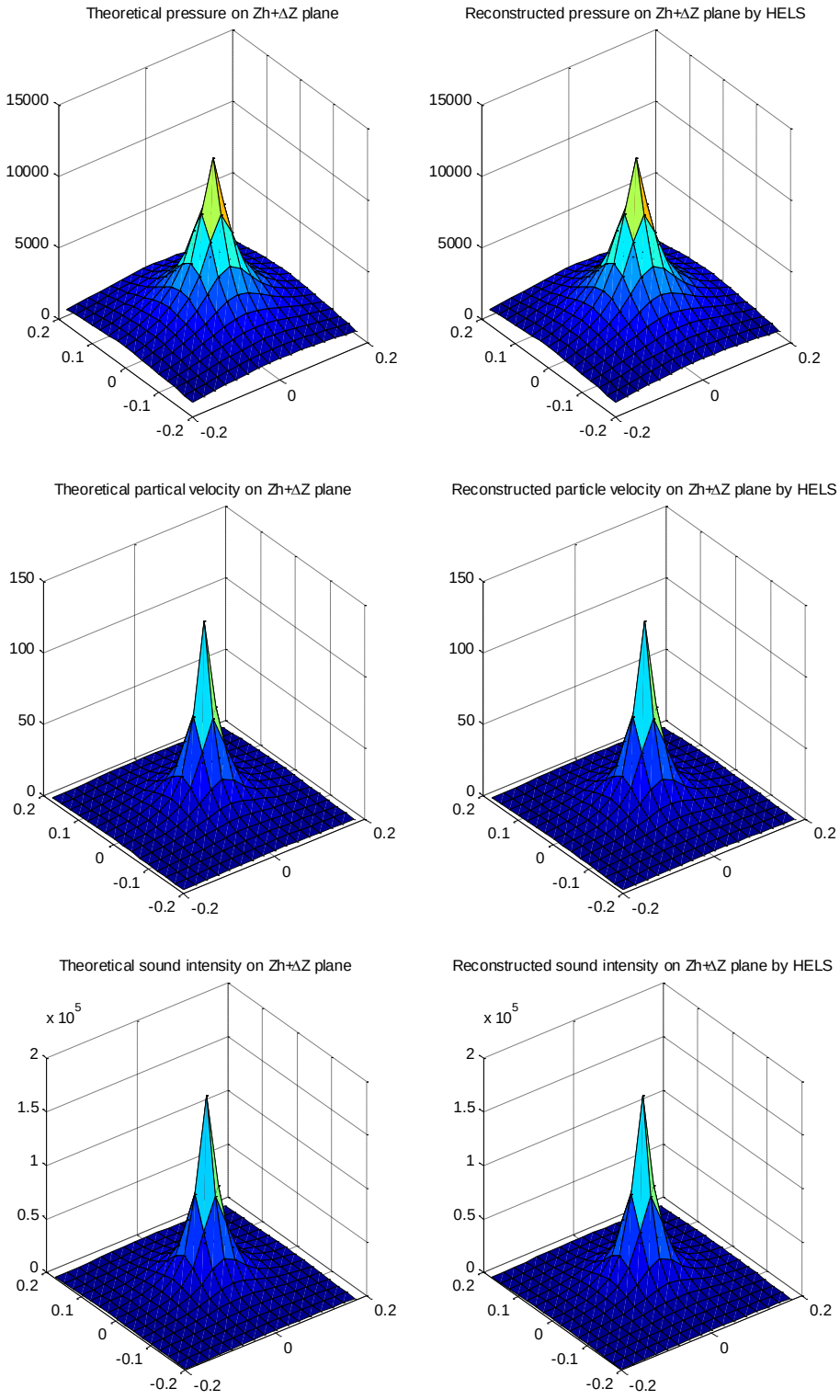

Figure 2.8 Analysis of reconstructed sound field generated by a monopole using HELS based NAH

Example 2: acoustic fields generated by a dipole sound source

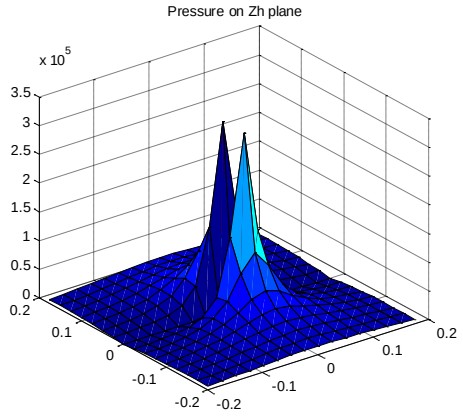

Figure 2.9 Acoustic pressure of a dipole as input for HELS based NAH

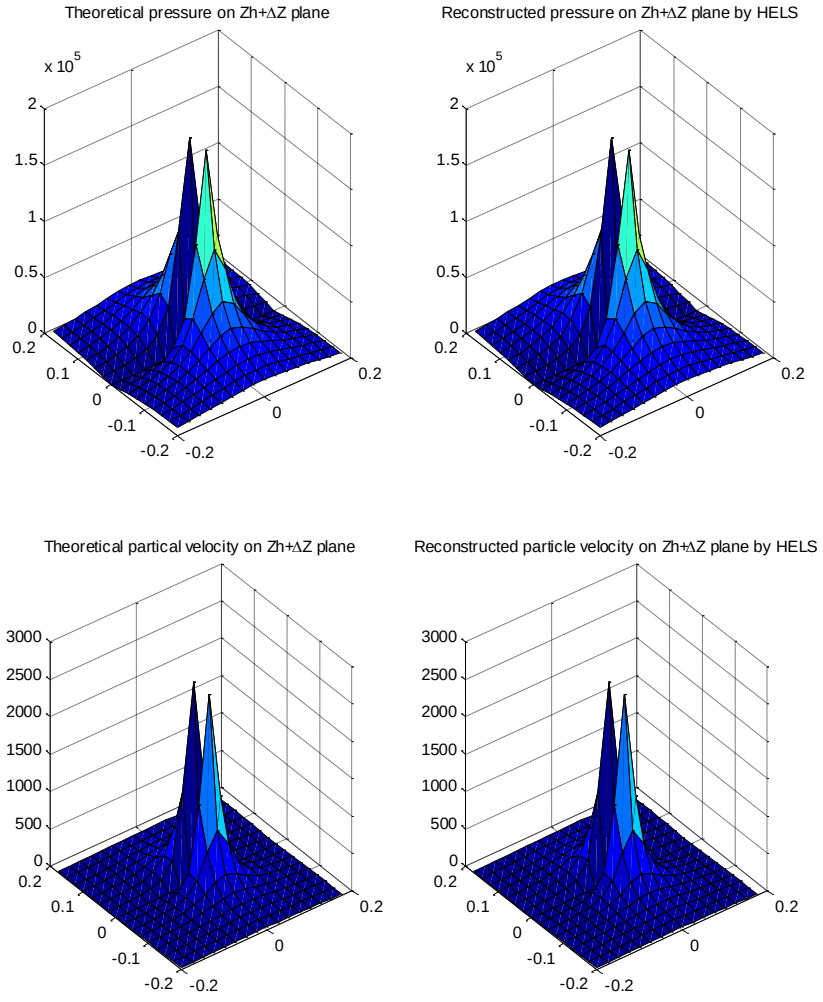

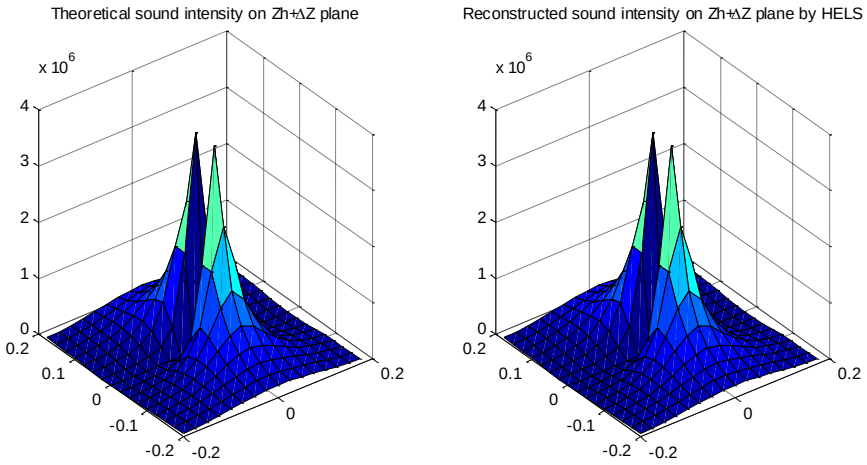

Figure 2.10 Analysis of reconstructed sound field generated by a dipole using HELS based NAH

2.3 Conclusion

In this chapter, a literature review of Fourier transform based NAH and conventional HELS based NAH are discussed in detail. The guidance and theoretical background are provided for both methods. Simulation studies show that both methods are capable of achieving relatively accurate sound field reconstruction for ideal sound sources.

CHAPTER 3

HELS BASED NAH WITH LASER

Most of NAH techniques use sound pressure as input to reconstruct sound field. The obvious reasons are that sound pressure is easy to measurement and the NAH theories are mature. A new acoustic sensor named Microflown is able to measure acoustic particle velocity directly. [55-59]. Finn Jacobsen and Yang Liu attempted to combine the Microflown instrument with NAH method. The particle velocity was measured by Miroflown sensors and then served as the input of NAH. Compared with the conventional NAH method, the particle velocity based NAH method demonstrated a larger dynamic range and a better accuracy on backward reconstruction [60, 61]. Furthermore, Finn Jacobsen and Virginie Jaud developed statistically optimized NAH based on particle velocity transducers. The accuracy of velocity-to-pressure predictions of the particle velocity based NAH method was much better than the accuracy of pressure-to-velocity predictions of conventional NAH method [62-64].

Yong-bin Zhang etc. studied the advantage of NAH based on the equivalent source method when the particle velocity instead of sound pressure was used as the input. The case was also considered that measured particle velocity data was contaminated by errors. It has demonstrated that NAH based on equivalent source method using particle velocity as input data was robust. Meanwhile, two experiments including sound field reconstructions of a box of heavy fiberboard and two sound sources were conducted [65, 66]. Patch near field acoustic holography (PNAH) based on particle velocity was developed. Compared with PNAH based on measured sound pressure, PNAH using particle velocity as input has a better computational efficiency because less iterations were needed to obtain a satisfying measurement aperture [67]. When it comes to an interior reconstruction problem, the conventional NAH showed its limitations since

sound pressure was scalar quantity and it failed to distinguish the difference between directly radiating sound and the reflections. NAH based on particle velocity was employed to reconstruct sound fields in a vehicle cabin. Due to the vector nature of particle velocity, the new method presented huge potential in complex interior problems [68].

3.1 Theoretical development

The acoustic pressure from a vibrating source is expressible as a superposition of the basis functions Ψ_j. Mathematically, this can be written in a matrix form as [13]

$$\hat{p}(x;w) = \sum_{j=1}^{J} C_j \Psi_j(\vec{x};w) \tag{3.1}$$

where $\hat{p}$ represents the complex amplitude of the radiated acoustic pressure at the point $\vec{x}_v$, v =1, 2, …, N, Ψ indicates the basis function, and $\{C_j\}_{J\times 1}$ is the unknown expansion coefficient. Note that there is no restriction whatsoever on the choice of the coordinate system to describe the basis functions. A practical choice is the spherical coordinate system since the analytic formulations for the corresponding spherical wave functions are readily available. Using the spherical coordinate system, the basis functions for an exterior acoustic radiation problem are expressible in terms of the spherical Hankel functions and spherical harmonics,

$$\Psi_j(\vec{x};w) = \Psi_{nl}(r,\theta,\varphi;w) = h_n^{(1)}(kr)Y_n^l(\theta,\varphi) \tag{3.2}$$

where k represents the acoustic wave number, $h_n^{(1)}(kr)$ is the spherical Hankel functions of order n of the first kind.

$$h_n^{(1)}(kr) = (-i)^{n+1}\frac{e^{ikr}}{kr}\sum_{m=0}^{n}\frac{i^m(n+m)!}{m!(2kr)^m(n-m)!} \tag{3.3}$$

For an interior problem, Ψ_j is given by the spherical Bessel functions and spherical harmonics,

$$\Psi_j(\vec{x};w) = \Psi_{nl}(r,\theta,\varphi;w) = h_n^{(2)}(kr)Y_n^l(\theta,\varphi) \tag{3.4}$$

where $h_n^{(2)}(kr)$ is the spherical Hankel functions of order n of the second kind, and $Y_n^l(\theta,\varphi)$ is the spherical harmonics.

$$Y_n^l(\theta,\varphi) = \sqrt{\frac{(2n+1)(n-l)!}{4\pi(n+l)!}}P_n^l(cos\theta)e^{il\varphi} \tag{3.5}$$

where $P_n^l(cos\theta)$ are the Legendre polynomials.

The indices *j*, *n*, and *l* in Eq. (3.2) and (3.3) are related via $j = n^2 + n + l + 1$, with *n* starting from 0 to *N* and *l* varying from –*n* to +*n*. Thus for each *n* and *l*, we have *j* = 1 to *J*, where *J* = (*N+1*) is the number of expansion functions for a given value of *N*.

In this invention, we use a laser scanner or laser vibrometer to measure the normal surface velocity of a vibrating structure, and take these measured data as input to reconstruct the radiated acoustic pressure field. To this end, we take the normal derivative of Eq. (3.1), and apply the Euler's equation to express the expansion coefficients $\{C\}_{J\times1}$ in terms of the normal surface velocity.

$$iw\rho_0\{\hat{v}_v(\vec{x}_m;w)\}_{M\times1} = \left[\frac{\partial\Psi(\vec{x}_m;w)}{\partial n}\right]_{M\times J}\{C\}_{J\times1} \tag{3.6}$$

where $\hat{v}_v(\vec{x}_m;w)$ is the normal surface velocity measured at $\vec{x}_m$, *m*=1, 2, ..., *M*, on the surface of a vibrating structure, $\rho_0$is the ambient density of the fluid medium, and the unknown coefficients $\{C\}_{J\times1}$can be obtained by taking a pseudo inversion of Eq. (3.6).

$$\{C\}_{J\times1} = iw\rho_0\left[\frac{\partial\Psi(\vec{x}_m;w)}{\partial n}\right]^{\dagger}_{J\times M}\{\hat{v}_v(\vec{x}_m;w)\}_{M\times1} \tag{3.7}$$

where the pseudo inversion in Eq. (3.7) is defined as

$$\left[\frac{\partial\Psi(\vec{x}_m;w)}{\partial n}\right]^{\dagger}_{J\times M} = \left(\left[\frac{\partial\Psi(\vec{x}_m;w)}{\partial n}\right]^{H}_{J\times M}\left[\frac{\partial\Psi(\vec{x}_m;w)}{\partial n}\right]_{M\times J}\right)^{-1}\left[\frac{\partial\Psi(\vec{x}_m;w)}{\partial n}\right]^{H}_{J\times M} \tag{3.8}$$

where a superscript *H* implies a Hermitian transpose of a matrix, and the above equation can be rewritten as follows:

$$\left[\frac{\partial\Psi(\vec{x};w)}{\partial n}\right] = \left(\hat{r}\,\frac{\partial}{\partial r} + \frac{1}{r}\hat{\theta}\,\frac{\partial}{\partial\theta} + \frac{1}{rsin\theta}\hat{\varphi}\,\frac{\partial}{\partial\varphi}\right)\Psi(\vec{x};w) \tag{3.9}$$

From Eq. (3.4) and (3.5), only the Hankel functions have the variable *r*, therefore, the partial differentiation of $\Psi(\vec{x};w)$ to variable *r* could be calculated as follows:

$$\frac{\partial\Psi(\vec{x};w)}{\partial r} = \frac{\partial}{\partial r}[h_n(kr)]Y_n^l(\theta,\varphi) \tag{3.10}$$

where

$$\frac{\partial}{\partial r}[h_n(kr)] = \begin{cases} k\left[h_{n-1}(kr) - \frac{n+1}{kr}h_n(kr)\right](n\geq 1) \\ kh_0(kr)\left(-\frac{1}{kr}+i\right)(n=0) \end{cases} \tag{3.11}$$

Similarly, the other two parts can be derived as follows:

$$\frac{\partial\Psi(\vec{x};w)}{\partial\theta} = \frac{\partial}{\partial\theta}[Y_n^l(\theta,\varphi)h_n(kr)] = h_n(kr)\frac{\partial}{\partial\theta}[Y_n^l(\theta,\varphi)] =$$

$$h_n(kr)\frac{\partial}{\partial\theta}\left[\sqrt{\frac{(2n+1)(n-l)!}{4\pi(n+l)!}}P_n^l(cos\theta)e^{il\varphi}\right] = \sqrt{\frac{(2n+1)(n-l)!}{4\pi(n+l)!}}h_n(kr)e^{il\varphi}\frac{\partial}{\partial\theta}[P_n^l(cos\theta)] =$$

$$\sqrt{\frac{(2n+1)(n-l)!}{4\pi(n+l)!}}h_n(kr)e^{il\varphi}\left[\frac{-(n+1)cos\theta P_n^l(cos\theta)+(n-m+1)P_{n+1}^l(cos\theta)}{sin\theta}\right] \tag{3.12}$$

$$\frac{\partial\Psi(\vec{x};w)}{\partial\varphi} = \frac{\partial}{\partial\varphi}[Y_n^l(\theta,\varphi)h_n(kr)] = h_n(kr)\frac{\partial}{\partial\varphi}[Y_n^l(\theta,\varphi)] =$$

$$h_n(kr)\frac{\partial}{\partial\varphi}\left[\sqrt{\frac{(2n+1)(n-l)!}{4\pi(n+l)!}}P_n^l(cos\theta)e^{il\varphi}\right] = \sqrt{\frac{(2n+1)(n-l)!}{4\pi(n+l)!}}h_n(kr)P_n^l(cos\theta)\frac{\partial}{\partial\varphi}\left[e^{il\varphi}\right] =$$

$$\sqrt{\frac{(2n+1)(n-l)!}{4\pi(n+l)!}}h_n(kr)P_n^l(cos\theta)ile^{il\varphi} \tag{3.13}$$

Therefore, the gradient of $\Psi(\vec{x};w)$ is listed as below:

$$\left[\frac{\partial\Psi(\vec{x};w)}{\partial n}\right]=\frac{1}{r}\sqrt{\frac{(2n+1)(n-l)!}{4\pi(n+l)!}}h_n(kr)e^{il\varphi}\left[\frac{-(n+1)cos\theta P_n^l(cos\theta)+(n-m+1)P_{n+1}^l(cos\theta)}{sin\theta}\right]+$$

$$\frac{1}{rsin\theta}\sqrt{\frac{(2n+1)(n-l)!}{4\pi(n+l)!}}h_n(kr)P_n^l(cos\theta)ile^{il\varphi}+\sqrt{\frac{(2n+1)(n-l)!}{4\pi(n+l)!}}P_n^l(cos\theta)e^{il\varphi}\frac{\partial}{\partial r}[h_n(kr)] \quad (3.14)$$

Substituting Eq. (3.7) into (3.1) leads to the main formulation of this invention to reconstruct the acoustic pressure.

$$\{\hat{p}_v(\vec{x}_v;w)\}_{N\times1}=[G_v(\vec{x}_v|\vec{x}_m)]_{N\times M}\{\hat{v}_v(\vec{x}_m;w)\}_{M\times1} \quad (3.15)$$

where $[G_v(\vec{x}_v|\vec{x}_m)]_{N\times M}$stands for the transfer function that correlates the normal surface velocity to the acoustic pressure field, which is given by

$$[G_v(\vec{x}_v|\vec{x}_m)]_{N\times M}=iw\rho_0[\Psi(\vec{x}_n;w)]_{N\times J}\left[\frac{\partial\Psi(\vec{x}_m;w)}{\partial n}\right]^{\dagger}_{J\times M} \quad (3.16)$$

The particle velocity can be derived:

$$\{\hat{v}_v(\vec{x}_v;w)\}_{N\times1}=[T_v(\vec{x}_v|\vec{x}_m)]_{N\times M}\{\hat{v}_v(\vec{x}_m;w)\}_{M\times1} \quad (3.17)$$

where $[T_v(\vec{x}_v|\vec{x}_m)]_{N\times M}$ represents the transfer function that correlates the measured normal surface velocity to the reconstructed particle velocity, which is given by

$$[T_v(\vec{x}_v|\vec{x}_m)]_{N\times M}=\left[\frac{\partial\Psi(\vec{x}_v;w)}{\partial n}\right]_{N\times J}\left[\frac{\partial\Psi(\vec{x}_m;w)}{\partial n}\right]^{\dagger}_{J\times M} \quad (3.18)$$

Consequently, the reconstructed intensity can be calculated as:

$$\left\{\hat{I}_v(\vec{x}_v;w)\right\}_{N\times1}=\frac{1}{2}Re(\{\hat{p}_v(\vec{x}_v;w)\}_{N\times1}\{\hat{v}_v(\vec{x}_v;w)\}^{*}_{N\times1}) \quad (3.19)$$

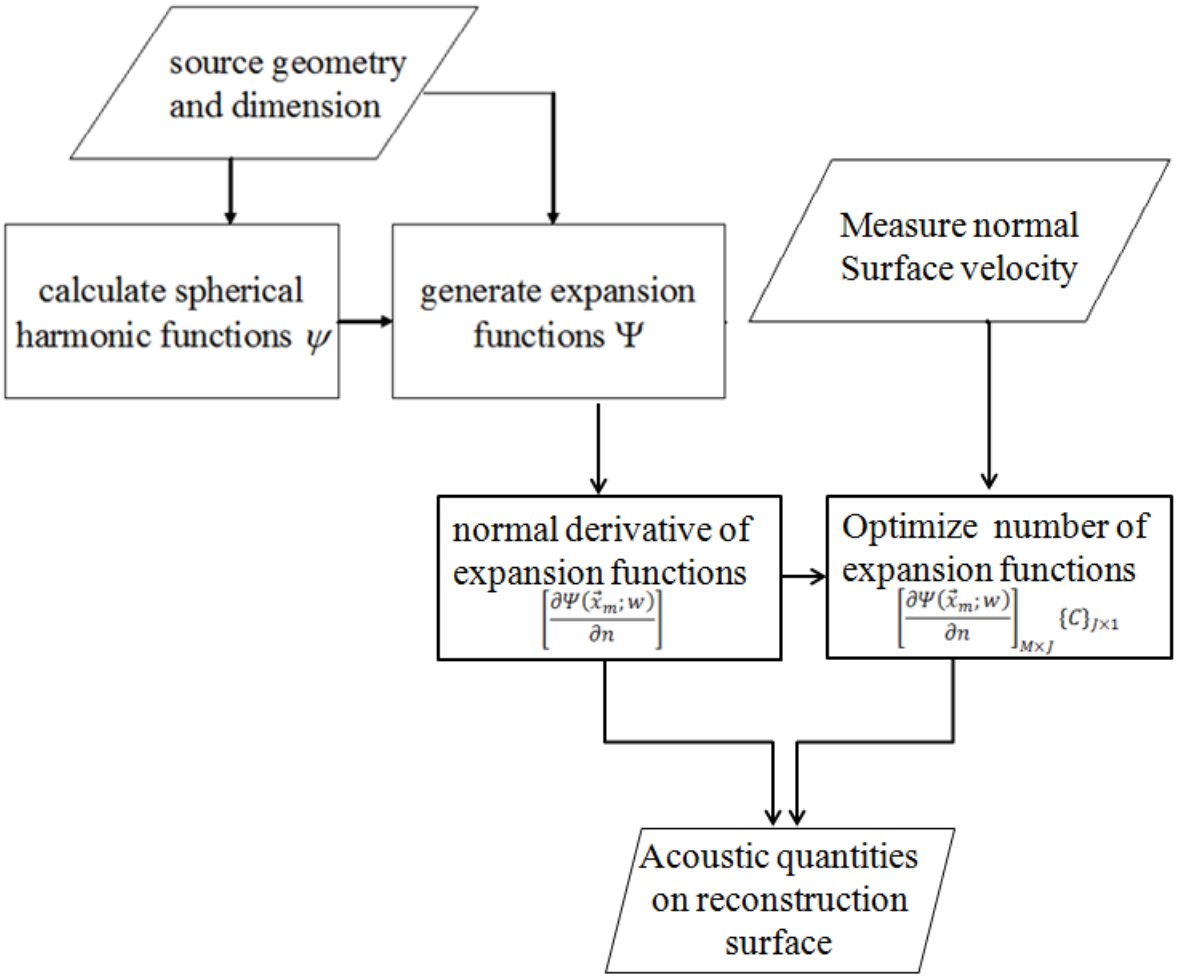

Figure 3.1 Flow chart of HELS based NAH with laser

3.2 Theoretical examples

For simplicity yet without loss of generality, a dilating sphere is considered which involves two expansion functions. Moreover, the normal surface velocity is measured at two points on the surface of a vibrating sphere of radius $\xi_m = a$, and the acoustic pressure is to be reconstructed at two arbitrary points in space leading to a square matrix equation that can be inverted directly. Accordingly, Eq. (3.15) can be rewritten as

$$\begin{Bmatrix}\hat{p}_1\\ \hat{p}_2\end{Bmatrix}=\begin{bmatrix}\Psi_{11} & \Psi_{21}\\ \Psi_{12} & \Psi_{22}\end{bmatrix}\begin{bmatrix}+\frac{\partial\Psi_{22}}{\partial\xi_1}\Big|_{\xi_{1=a}} & -\frac{\partial\Psi_{21}}{\partial\xi_1}\Big|_{\xi_{1=a}}\\ -\frac{\partial\Psi_{12}}{\partial\xi_2}\Big|_{\xi_{2=a}} & +\frac{\partial\Psi_{11}}{\partial\xi_2}\Big|_{\xi_{2=a}}\end{bmatrix}\frac{\begin{Bmatrix}iw\rho_0\hat{v}_1\\ iw\rho_0\hat{v}_2\end{Bmatrix}}{det\left(\frac{\partial\Psi}{\partial\xi_m}\Big|_{\xi_{m=a}}\right)} \tag{3.20}$$

where the determinant is:

$$det\left(\frac{\partial\Psi}{\partial\xi_m}\Big|_{\xi_{m=a}}\right)=\left(\frac{\partial\Psi_{11}}{\partial\xi_1}\Big|_{\xi_{1=a}}\ \ \frac{\partial\Psi_{22}}{\partial\xi_2}\Big|_{\xi_{2=a}}-\frac{\partial\Psi_{21}}{\partial\xi_1}\Big|_{\xi_{1=a}}\ \ \frac{\partial\Psi_{12}}{\partial\xi_2}\Big|_{\xi_{2=a}}\right) \tag{3.21}$$

The determinant of the square matrix is given by Eq. (3.4), the first subscript in the expansion functions implies the order of expansion functions, the second subscript stands for the sequence of measurement points, and arguments in the expansion functions are omitted for brevity. These expansion functions and their derivatives are given by [69]

$$\Psi_{11}=-i\frac{1}{\sqrt{4\pi}}\frac{e^{ikr_1}}{kr_1} \tag{3.22a}$$

$$\Psi_{21}=-\sqrt{\frac{3}{4\pi}}\frac{(kr_1+i)e^{ikr_1}}{(kr_1)^2}\cos(\theta_1) \tag{3.22b}$$

$$\Psi_{12}=-i\frac{1}{\sqrt{4\pi}}\frac{e^{ikr_2}}{kr_2} \tag{3.22c}$$

$$\Psi_{22}=-\sqrt{\frac{3}{4\pi}}\frac{(kr_2+i)e^{ikr_2}}{(kr_2)^2}\cos(\theta_2) \tag{3.22d}$$

$$\frac{\partial\Psi_{11}}{\partial\xi_1}\Big|_{\xi_{1=a}}=\frac{1}{\sqrt{4\pi}}\frac{(ka+i)e^{ika}}{ka^2} \tag{3.22e}$$

$$\frac{\partial\Psi_{22}}{\partial\xi_2}\Big|_{\xi_{2=a}}=\sqrt{\frac{3}{4\pi}}\frac{[2ka+i(2-k^2a^2)]e^{ika}}{k^2a^3}cos\theta_{meas,2} \tag{3.22f}$$

$$\frac{\partial\Psi_{21}}{\partial\xi_1}\Big|_{\xi_{1=a}}=\sqrt{\frac{3}{4\pi}}\frac{[2ka+i(2-k^2a^2)]e^{ika}}{k^2a^3}cos\theta_{meas,1} \tag{3.22g}$$

$$\frac{\partial\Psi_{12}}{\partial\xi_2}\Big|_{\xi_{2=a}}=\frac{1}{\sqrt{4\pi}}\frac{(ka+i)e^{ika}}{ka^2} \tag{3.22h}$$

where $\theta_{meas,1}$ and $\theta_{meas,2}$ are the polar angles at the measurement points.

Then, the Eq. (3.22) is substituted into Eq. (3.21) and the determinant becomes:

$$det\left(\frac{\partial\Psi}{\partial\xi_m}\Big|_{\xi_m=a}\right)=\sqrt{\frac{3}{4\pi}}\frac{(ka+i)[2ka+i(2-k^2a^2)]e^{i2ka}}{k^3a^5}(cos\theta_{meas,2}-cos\theta_{meas,1}) \tag{3.23}$$

In the case of a dilating sphere, the normal surface velocity is a constant. Then, $\hat{v}_1$ and $\hat{v}_2$ in Eq. (3.20) can be substituted into one constant *v*. Consequently, the reconstructed pressure could be calculated as follows:

$$\begin{Bmatrix}\hat{p}_1\\ \hat{p}_2\end{Bmatrix}=\begin{bmatrix}\Psi_{11} & \Psi_{21}\\ \Psi_{12} & \Psi_{22}\end{bmatrix}\begin{bmatrix}+\frac{\partial\Psi_{22}}{\partial\xi_1}\Big|_{\xi_{1=a}} & -\frac{\partial\Psi_{21}}{\partial\xi_1}\Big|_{\xi_{1=a}}\\ -\frac{\partial\Psi_{12}}{\partial\xi_2}\Big|_{\xi_{2=a}} & +\frac{\partial\Psi_{11}}{\partial\xi_2}\Big|_{\xi_{2=a}}\end{bmatrix}\frac{\begin{Bmatrix}iw\rho_0\hat{v}\\ iw\rho_0\hat{v}\end{Bmatrix}}{det\left(\frac{\partial\Psi}{\partial\xi_m}\Big|_{\xi_m=a}\right)}=$$

$$\begin{bmatrix}-i\frac{1}{\sqrt{4\pi}}\frac{e^{ikr_1}}{kr_1} & -\sqrt{\frac{3}{4\pi}}\frac{(kr_1+i)e^{ikr_1}}{(kr_1)^2}\cos(\theta_1)\\ -i\frac{1}{\sqrt{4\pi}}\frac{e^{ikr_2}}{kr_2} & -\sqrt{\frac{3}{4\pi}}\frac{(kr_2+i)e^{ikr_2}}{(kr_2)^2}\cos(\theta_2)\end{bmatrix}\times$$

$$\begin{bmatrix}\sqrt{\frac{3}{4\pi}}\frac{[2ka+i(2-k^2a^2)]e^{ika}}{k^2a^3}cos\theta_{meas,2} & -\sqrt{\frac{3}{4\pi}}\frac{[2ka+i(2-k^2a^2)]e^{ika}}{k^2a^3}cos\theta_{meas,1}\\ -\frac{1}{\sqrt{4\pi}}\frac{(ka+i)e^{ika}}{ka^2} & \frac{1}{\sqrt{4\pi}}\frac{(ka+i)e^{ika}}{ka^2}\end{bmatrix}\times$$

$$\frac{\begin{Bmatrix}iw\rho_0\hat{v}\\ iw\rho_0\hat{v}\end{Bmatrix}}{\sqrt{\frac{3}{4\pi}}\frac{(ka+i)[2ka+i(2-k^2a^2)]e^{i2ka}}{k^3a^5}(cos\theta_{meas,2}-cos\theta_{meas,1})}=\begin{bmatrix}-i\frac{1}{\sqrt{4\pi}}\frac{e^{ikr_1}}{kr_1} & -\sqrt{\frac{3}{4\pi}}\frac{(kr_1+i)e^{ikr_1}}{(kr_1)^2}\cos(\theta_1)\\ -i\frac{1}{\sqrt{4\pi}}\frac{e^{ikr_2}}{kr_2} & -\sqrt{\frac{3}{4\pi}}\frac{(kr_2+i)e^{ikr_2}}{(kr_2)^2}\cos(\theta_2)\end{bmatrix}\times$$

$$\begin{Bmatrix}iw\rho_0\left(\frac{\sqrt{4\pi}ka^2e^{-ika}}{ka+i}\right)\\ 0\end{Bmatrix}=\begin{Bmatrix}\rho_0\hat{v}c\left(\frac{ka}{ka+i}\right)(\frac{a}{r_1})e^{-ika+ikr_1}\\ \rho_0\hat{v}c\left(\frac{ka}{ka+i}\right)(\frac{a}{r_2})e^{-ika+ikr_2}\end{Bmatrix} \tag{3.24}$$

The reconstructed pressure from HELS based NAH using normal surface velocity as input is the same as the analytic solution [70].

Another case of an oscillating sphere is considered. The normal surface velocity is expressible as $\hat{v}_0 cos\theta_{meas,m}$, *m*=1 and 2.

$$\begin{Bmatrix}\hat{p}_1\\ \hat{p}_2\end{Bmatrix}=\begin{bmatrix}\Psi_{11} & \Psi_{21}\\ \Psi_{12} & \Psi_{22}\end{bmatrix}\begin{bmatrix}+\frac{\partial\Psi_{22}}{\partial\xi_1}\Big|_{\xi_{1=a}} & -\frac{\partial\Psi_{21}}{\partial\xi_1}\Big|_{\xi_{1=a}}\\ -\frac{\partial\Psi_{12}}{\partial\xi_2}\Big|_{\xi_{2=a}} & +\frac{\partial\Psi_{11}}{\partial\xi_2}\Big|_{\xi_{2=a}}\end{bmatrix}\frac{\begin{Bmatrix}iw\rho_0\hat{v}_0 cos\theta_{meas,1}\\ iw\rho_0\hat{v}_0 cos\theta_{meas,2}\end{Bmatrix}}{det\left(\frac{\partial\Psi}{\partial\xi_m}\Big|_{\xi_m=a}\right)}=$$

$$\begin{bmatrix}-i\frac{1}{\sqrt{4\pi}}\frac{e^{ikr_1}}{kr_1} & -\sqrt{\frac{3}{4\pi}}\frac{(kr_1+i)e^{ikr_1}}{(kr_1)^2}\cos(\theta_1)\\ -i\frac{1}{\sqrt{4\pi}}\frac{e^{ikr_2}}{kr_2} & -\sqrt{\frac{3}{4\pi}}\frac{(kr_2+i)e^{ikr_2}}{(kr_2)^2}\cos(\theta_2)\end{bmatrix}\times$$

$$\begin{bmatrix}\sqrt{\frac{3}{4\pi}}\frac{[2ka+i(2-k^2a^2)]e^{ika}}{k^2a^3}cos\theta_{meas,2} & -\sqrt{\frac{3}{4\pi}}\frac{[2ka+i(2-k^2a^2)]e^{ika}}{k^2a^3}cos\theta_{meas,1}\\ -\frac{1}{\sqrt{4\pi}}\frac{(ka+i)e^{ika}}{ka^2} & \frac{1}{\sqrt{4\pi}}\frac{(ka+i)e^{ika}}{ka^2}\end{bmatrix}\times$$

$$\frac{\begin{Bmatrix}iw\rho_0\hat{v}\\ iw\rho_0\hat{v}\end{Bmatrix}}{\sqrt{\frac{3}{4\pi}}\frac{(ka+i)[2ka+i(2-k^2a^2)]e^{i2ka}}{k^3a^5}(cos\theta_{meas,2}-cos\theta_{meas,1})}=\begin{bmatrix}-i\frac{1}{\sqrt{4\pi}}\frac{e^{ikr_1}}{kr_1} & -\sqrt{\frac{3}{4\pi}}\frac{(kr_1+i)e^{ikr_1}}{(kr_1)^2}\cos(\theta_1)\\ -i\frac{1}{\sqrt{4\pi}}\frac{e^{ikr_2}}{kr_2} & -\sqrt{\frac{3}{4\pi}}\frac{(kr_2+i)e^{ikr_2}}{(kr_2)^2}\cos(\theta_2)\end{bmatrix}\times$$

$$\begin{Bmatrix}0\\ iw\rho_0\hat{v}_0\sqrt{\frac{4\pi}{3}}\left(\frac{k^2a^3e^{-ika}}{2ka+i(2-k^2a^2)}\right)\end{Bmatrix}=\begin{Bmatrix}\rho_0\hat{v}c\left(\frac{ka(kr_1+i)e^{ikr_1-ika}}{k^2a^2-2+i2ka}\right)(\frac{a}{r_1})^2\cos(\theta_1)\\ \rho_0\hat{v}c\left(\frac{ka(kr_2+i)e^{ikr_2-ika}}{k^2a^2-2+i2ka}\right)(\frac{a}{r_2})^2\cos(\theta_2)\end{Bmatrix} \quad (3.25)$$

The results are the same with the analytic solutions [70].

3.3 Error Analysis

To study the impacts of the errors in measured normal surface velocities, we conduct an in-depth error analysis of the general solution. The errors imbedded in the measurements of the normal surface velocity are spatially uncorrelated Gaussian noise and are expressible as $\hat{v}_m + \xi_m$. Again, we consider the case involving two expansion functions and assume that measurements of the normal surface velocity are taken on the surface of a sphere of radius *a* at ξ_m, m = 1 and 2. The explicit solution Eq. (3.7) can be written as

$$\begin{Bmatrix}\hat{p}_1\\ \hat{p}_2\end{Bmatrix}=\begin{bmatrix}\Psi_{11} & \Psi_{21}\\ \Psi_{12} & \Psi_{22}\end{bmatrix}\begin{bmatrix}+\frac{\partial\Psi_{22}}{\partial\xi_1}\Big|_{\xi_{1=a}} & -\frac{\partial\Psi_{21}}{\partial\xi_1}\Big|_{\xi_{1=a}}\\ -\frac{\partial\Psi_{12}}{\partial\xi_2}\Big|_{\xi_{2=a}} & +\frac{\partial\Psi_{11}}{\partial\xi_2}\Big|_{\xi_{2=a}}\end{bmatrix}\frac{\begin{Bmatrix}iw\rho_0\hat{v}_1+\varepsilon_1\\ iw\rho_0\hat{v}_2+\varepsilon_2\end{Bmatrix}}{det\left(\frac{\partial\Psi}{\partial\xi_m}\Big|_{\xi_m=a}\right)} \tag{3.26}$$

where the determinant $det\left(\frac{\partial\Psi}{\partial\xi_m}\Big|_{\xi_m=a}\right)$ is decided as the same as Eq. (3.21).

The case of a dilating sphere in which the normal surface velocity is constant, then $\hat{v}_1$ and $\hat{v}_2$ in Eq. (3.26) can be substituted by one constant *v*. Consequently, Eq. (3.26) can be rewritten as

$$\begin{Bmatrix}\hat{p}_1\\ \hat{p}_2\end{Bmatrix}=\begin{bmatrix}\Psi_{11} & \Psi_{21}\\ \Psi_{12} & \Psi_{22}\end{bmatrix}\begin{bmatrix}+\frac{\partial\Psi_{22}}{\partial\xi_1}\Big|_{\xi_{1=a}} & -\frac{\partial\Psi_{21}}{\partial\xi_1}\Big|_{\xi_{1=a}}\\ -\frac{\partial\Psi_{12}}{\partial\xi_2}\Big|_{\xi_{2=a}} & +\frac{\partial\Psi_{11}}{\partial\xi_2}\Big|_{\xi_{2=a}}\end{bmatrix}\frac{\begin{Bmatrix}iw\rho_0(\hat{v}+\varepsilon_1)\\ iw\rho_0(\hat{v}+\varepsilon_2)\end{Bmatrix}}{det\left(\frac{\partial\Psi}{\partial\xi_m}\Big|_{\xi_m=a}\right)}=$$

$$\begin{bmatrix}-i\frac{1}{\sqrt{4\pi}}\frac{e^{ikr_1}}{kr_1} & -\sqrt{\frac{3}{4\pi}}\frac{(kr_1+i)e^{ikr_1}}{(kr_1)^2}\cos(\theta_1)\\ -i\frac{1}{\sqrt{4\pi}}\frac{e^{ikr_2}}{kr_2} & -\sqrt{\frac{3}{4\pi}}\frac{(kr_2+i)e^{ikr_2}}{(kr_2)^2}\cos(\theta_2)\end{bmatrix}\times$$

$$\begin{bmatrix}\sqrt{\frac{3}{4\pi}}\frac{[2ka+i(2-k^2a^2)]e^{ika}}{k^2a^3}cos\theta_{meas,2} & -\sqrt{\frac{3}{4\pi}}\frac{[2ka+i(2-k^2a^2)]e^{ika}}{k^2a^3}cos\theta_{meas,1}\\ -\frac{1}{\sqrt{4\pi}}\frac{(ka+i)e^{ika}}{ka^2} & \frac{1}{\sqrt{4\pi}}\frac{(ka+i)e^{ika}}{ka^2}\end{bmatrix}\times$$

$$\frac{\begin{Bmatrix}iw\rho_0(\hat{v}+\varepsilon_1)\\ iw\rho_0(\hat{v}+\varepsilon_2)\end{Bmatrix}}{\sqrt{\frac{3}{4\pi}}\frac{(ka+i)[2ka+i(2-k^2a^2)]e^{i2ka}}{k^3a^5}(cos\theta_{meas,2}-cos\theta_{meas,1})}=\begin{Bmatrix}\rho_0\hat{v}c\left(\frac{kae^{(ikr_1-ika)}}{ka+i}\right)\left(\frac{a}{r_1}\right)+O(\varepsilon_1,\varepsilon_2)\\ \rho_0\hat{v}c\left(\frac{kae^{(ikr_2-ika)}}{ka+i}\right)\left(\frac{a}{r_2}\right)+O(\varepsilon_1,\varepsilon_2)\end{Bmatrix} \tag{3.27}$$

where the error terms can be calculated as follows:

$$O(\varepsilon_1,\varepsilon_2)=\rho_0c\left(\frac{kae^{(ikr_1-ika)}}{ka+i}\right)\left(\frac{a}{r_1}\right)\frac{1}{(cos\theta_{meas,2}-cos\theta_{meas,1})}(\mu_1\varepsilon_1+\mu_2\varepsilon_2)+$$

$$\rho_0c\frac{ka(kr+i)e^{(ikr_2-ika)}}{[(k^2a^2-2)+2ika]}\left(\frac{a}{r_2}\right)^2\frac{cos\theta}{(cos\theta_{meas,2}-cos\theta_{meas,1})}(v_1\varepsilon_1+v_2\varepsilon_2) \tag{3.28}$$

where μ_m and v_m, *m*=1 and 2, are defined as

$$\mu_1 = cos\theta_{meas,2} \tag{3.29a}$$

$$\mu_2 = -cos\theta_{meas,1} \tag{3.29b}$$

$$v_1 = 1 \tag{3.29c}$$

$$v_2 = -1 \tag{3.29d}$$

Then, the case of an oscillating sphere is studied in which the normal surface velocities are given by $\hat{v}_m cos\theta_{meas,m}, m = 1 and\ 2$,

$$\begin{Bmatrix}\hat{p}_1\\ \hat{p}_2\end{Bmatrix} = \begin{bmatrix}\Psi_{11} & \Psi_{21}\\ \Psi_{12} & \Psi_{22}\end{bmatrix}\begin{bmatrix}+\frac{\partial\Psi_{22}}{\partial\xi_1}\Big|_{\xi_{1=a}} & -\frac{\partial\Psi_{21}}{\partial\xi_1}\Big|_{\xi_{1=a}}\\ -\frac{\partial\Psi_{12}}{\partial\xi_2}\Big|_{\xi_{2=a}} & +\frac{\partial\Psi_{11}}{\partial\xi_2}\Big|_{\xi_{2=a}}\end{bmatrix}\frac{\begin{Bmatrix}iw\rho_0(\hat{v}_0 cos\theta_{meas,1}+\varepsilon_1)\\ iw\rho_0(\hat{v}_0 cos\theta_{meas,2}+\varepsilon_2)\end{Bmatrix}}{det\left(\frac{\partial\Psi}{\partial\xi_m}\Big|_{\xi_{m=a}}\right)} =$$

$$\begin{bmatrix}-i\frac{1}{\sqrt{4\pi}}\frac{e^{ikr_1}}{kr_1} & -\sqrt{\frac{3}{4\pi}}\frac{(kr_1+i)e^{ikr_1}}{(kr_1)^2}\cos(\theta_1)\\ -i\frac{1}{\sqrt{4\pi}}\frac{e^{ikr_2}}{kr_2} & -\sqrt{\frac{3}{4\pi}}\frac{(kr_2+i)e^{ikr_2}}{(kr_2)^2}\cos(\theta_2)\end{bmatrix}\times$$

$$\begin{bmatrix}\sqrt{\frac{3}{4\pi}}\frac{[2ka+i(2-k^2a^2)]e^{ika}}{k^2a^3}cos\theta_{meas,2} & -\sqrt{\frac{3}{4\pi}}\frac{[2ka+i(2-k^2a^2)]e^{ika}}{k^2a^3}cos\theta_{meas,1}\\ -\frac{1}{\sqrt{4\pi}}\frac{(ka+i)e^{ika}}{ka^2} & \frac{1}{\sqrt{4\pi}}\frac{(ka+i)e^{ika}}{ka^2}\end{bmatrix}\times$$

$$\frac{\begin{Bmatrix}iw\rho_0(\hat{v}_0 cos\theta_{meas,1}+\varepsilon_1)\\ iw\rho_0(\hat{v}_0 cos\theta_{meas,2}+\varepsilon_2)\end{Bmatrix}}{\sqrt{\frac{3}{4\pi}}\frac{(ka+i)[2ka+i(2-k^2a^2)]e^{i2ka}}{k^3a^5}(cos\theta_{meas,2}-cos\theta_{meas,1})} = \begin{Bmatrix}\rho_0\hat{v}c\left(\frac{kae^{(ikr_1-ika)}}{ka+i}\right)\left(\frac{a}{r_1}\right)^2 + O(\varepsilon_1,\varepsilon_2)\\ \rho_0\hat{v}c\left(\frac{kae^{(ikr_2-ika)}}{ka+i}\right)\left(\frac{a}{r_2}\right)^2 + O(\varepsilon_1,\varepsilon_2)\end{Bmatrix} \tag{3.30}$$

The error term is listed as follows:

$$O(\varepsilon_1,\varepsilon_2) = \rho_0 c\left(\frac{kae^{(ikr_1-ika)}}{ka+i}\right)\left(\frac{a}{r_1}\right)\frac{1}{(cos\theta_{meas,2}-cos\theta_{meas,1})}(\mu_1\varepsilon_1+\mu_2\varepsilon_2) +$$

$$\rho_0 c\frac{ka(kr+i)e^{(ikr_2-ika)}}{[(k^2a^2-2)+2ika]}\left(\frac{a}{r_2}\right)^2\frac{cos\theta}{(cos\theta_{meas,2}-cos\theta_{meas,1})}(v_1\varepsilon_1+v_2\varepsilon_2) \tag{3.31}$$

The error term turns out to be exactly the same as those in Eq. (3.27). These examples indicate that errors in the reconstructed acoustic pressures are independent of the normal surface

velocity distributions. They are mainly determined by expansion functions and are bounded everywhere. The asymptotic behaviors of errors in these cases are, respectively, given by

$$O(\varepsilon_1, \varepsilon_2) \propto \left(\frac{a}{r}\right)(\gamma_1\varepsilon_1 + \gamma_2\varepsilon_2), \quad as\ r \to \infty, ka \gg 1\ and\ kr \gg 1 \tag{3.32a}$$

$$O(\varepsilon_1, \varepsilon_2) \propto ka\left(\frac{a}{r}\right)(\gamma_1\varepsilon_1 + \gamma_2\varepsilon_2), \quad as\ r \to \infty, ka \ll 1\ and\ kr \gg 1 \tag{3.32b}$$

$$O(\varepsilon_1, \varepsilon_2) \propto (\gamma_1\varepsilon_1 + \gamma_2\varepsilon_2), \quad as\ r \to a, ka \gg 1\ and\ kr \gg 1 \tag{3.32c}$$

$$O(\varepsilon_1, \varepsilon_2) \propto (ka)(\gamma_1\varepsilon_1 + \gamma_2\varepsilon_2), \quad as\ r \to a, ka \ll 1\ and\ kr \ll 1 \tag{3.32d}$$

where r_1 and r_2 are finite and independent of *ka* and *kr*.

The above results may be extended to any order of the expansion solution given by the Eq. (3.15). The elements of the transfer matrix has the following characteristics.

$$G_v(\vec{x}_v|\vec{x}_m) \propto \frac{\Psi(\vec{x};w)}{\partial\Psi(\vec{x};w)/\partial n} \tag{3.33}$$

For an exterior problem, we can use Eq. (3.2) to express the expansion function and its derivative. Therefore, for a spherical surface the elements of the transfer matrix in Eq. (3.15) is expressible as

$$G_v(\vec{x}_v|\vec{x}_m) \propto \frac{h_n^{(1)}(\chi)Y_n^l(\theta,\varphi)}{\left[\partial h_n^{(1)}(\chi_m)/\partial\chi_m\right]Y_n^l(\theta_m,\varphi_m)} \tag{3.34}$$

where χ=*kr* and $\chi_m = k\xi_m$.

The characteristics of Eq. (3.27) are reflected in Eq. (3.26) for the general form of error term. In fact, it can be shown that the errors involved in the general solution for a spherical surface are proportional to

$$O(\varepsilon) \propto$$

$$\sum_{n=0}^{N}\sum_{l=-n}^{n}\sum_{m=1}^{M}\frac{h_n^{(1)}(\chi)Y_n^l(\theta,\varphi)}{\left[\partial h_n^{(1)}(\chi_m)/\partial\chi_m\right]Y_n^l(\theta_m,\varphi_m)}\gamma_{nm}\varepsilon_m = \sum_{n=0}^{N}\sum_{m=1}^{M}\frac{h_n^{(1)}(\chi)Y_n^l(\theta,\varphi)}{\left[dh_n^{(1)}(\chi_m)/d\chi_m\right]_{\xi_m=a}}\varsigma_{nm}\varepsilon_m$$

(3.35)

$$\varsigma_{nm} = \sum_{l=-n}^{n}\frac{Y_n^l(\theta,\varphi)}{Y_n^l(\theta_m,\varphi_m)}\gamma_{nm} \tag{3.36}$$

The asymptotic behaviors of the spherical Hankel function and their derivatives at large argument $\chi \gg 1$ are given by[12]

$$h_n^{(1)}(\chi) \approx (-1)^{(n+1)}\frac{e^{i\chi}}{\chi} \tag{3.37}$$

$$\left.\frac{dh_n^{(1)}(\chi_m)}{d\chi_m}\right|_{\xi_m=a} \approx (-1)^n\frac{e^{i\chi}}{\chi} \tag{3.38}$$

Meanwhile, the quantities given by Eq. (3.36) are ratios of angular spectra multiplied by constants, which are independent of the frequency and distance. Therefore, in the far field ($kr >> 1$) and at the high frequency ($ka >> 1$) limit, the magnitude of the errors involved in Eq. (3.15) is bounded by

$$O(\varepsilon) \propto N\left(\frac{a}{r}\right)e^{ikr}\sum_{m=1}^{M}\varsigma_m\varepsilon_m \le N\left(\frac{a}{r}\right)\sum_{m=1}^{M}|\varsigma_m\varepsilon_m| \tag{3.39}$$

where *N* represents the total number of the spherical Hankel functions involved in the expansion.

On the other hand, in the far field ($kr >> 1$) under at the low frequency ($ka << 1$) limit, the magnitude of the errors involved in the general solution is bounded by

$$O(\varepsilon) \propto (ka)\left(\frac{a}{r}\right)e^{ikr}\sum_{m=1}^{M}\varsigma_m\varepsilon_m \le ka\left(\frac{a}{r}\right)\sum_{m=1}^{M}|\varsigma_m\varepsilon_m| \tag{3.40}$$

In a similar manner, we can obtain the asymptotic behaviors of the errors involved in Eq. (3.15) in the near field. For example, in the near field ($r \to a$) and high frequency ($ka >> 1$) limit, the errors in the general solution are bounded by

$$O(\varepsilon) \propto ka \sum_{m=1}^{M} |\varsigma_m \varepsilon_m| \tag{3.41}$$

These general results are consistent with the asymptotic behaviors given by Eq. (3.32) for a two-term expansion. Eq. (3.39) to (3.41) demonstrate that the acoustic pressures reconstructed by using the general solution Eq. (3.15) are bounded. In fact, the magnitudes of errors in reconstructions decrease monotonically as r $\to\infty$, which means that Eq. (3.15) is robust in reconstructing the acoustic pressure field.

3.4 Extension to arbitrary geometry

Eq. (3.15) may be extended to an arbitrarily shaped, convex, and blunt structure, whose aspect ratio is close to (1:1:1). Under this condition, it is no longer possible to expand the normal surface velocity exactly in terms of the spherical Hankel functions and spherical harmonics, since the source geometry is not spherical. The errors involved in using such an expansion will depend on the level of deviations of the source geometry from a sphere. The smoother and the closer of a source surface to a spherical one is, the smaller the errors in the resultant expansion solutions are, and vice versa. In engineering applications, it is permissible to use the spherical Hankel functions and spherical harmonics to approximate the acoustic quantities on a non-spherical, yet smooth and convex surface whose aspect ratio is close to (1:1:1).

Accordingly, the normal surface velocity can be written as

$$iw\rho_0\{\hat{v}_v(\vec{x}_v; w)\}_{M\times 1} = \left[\frac{\partial \Psi(\vec{x}_v; w)}{\partial v}\right]_{M\times J} \{C\}_{J\times 1} + iw\rho_0\{\Delta\hat{v}_v(\vec{x}_v; w)\}_{M\times 1} \tag{3.42}$$

where the left side of Eq. (3.42) implies the actual normal surface velocity on a non-spherical source geometry, the first term on the right side is the exact solution to the normal surface velocity when the source geometry is spherical, and the second term depicts the discrepancies between the actual normal surface velocity and the exact solution via an expansion of the spherical Hankel functions and spherical harmonics on a non-spherical source geometry.

To determine the unknown coefficients $\{C\}_{J\times 1}$ in Eq. (3.42), we measure the normal surface velocity $\hat{v}_v$ on the source surface at $\hat{x}_v$, $v = 1, 2, \ldots, N$, and take a pseudo inversion.

$$\{C\}_{J\times 1} = iw\rho_0 \left[\frac{\partial \Psi(\vec{x}_v;w)}{\partial v}\right]^{\dagger}_{J\times M} \langle \{\hat{v}_v(\vec{x}_v;w)\}_{M\times 1} - \{\Delta\hat{v}_v(\vec{x}_v;w)\}_{M\times 1}\rangle \tag{3.43}$$

where $\{\Delta\hat{v}_v(\vec{x}_v;w)\}_{M\times 1}$ on the right side of Eq.(3.43) represents the errors involved in the expansion solution. Substituting Eq.(3.43) into (3.1) then yields,

$$\{\hat{p}(\vec{x}_v;w)\}_{N\times 1} = [G_v(\vec{x}_v|\vec{x}_m)]_{N\times M}\{\hat{v}_v(\vec{x}_m;w)\}_{M\times 1} + \{\Delta\hat{p}(\vec{x}_v;w)\}_{N\times 1}\} \tag{3.44}$$

where $[G_v(\vec{x}_v|\vec{x}_m)]_{N\times M}$ is the transfer function given by Eq.(3.16) and $\{\Delta\hat{p}(\vec{x}_v;w)\}_{N\times 1}\}$ represents the errors in the reconstructed acoustic pressure given by,

$$\{\Delta\hat{p}(\vec{x}_v;w)\}_{N\times 1}\} = [G_v(\vec{x}_v|\vec{x}_m)]_{N\times M}\{\Delta\hat{v}_v(\vec{x}_v;w)\}_{M\times 1} \tag{3.45}$$

Substituting Eq. (3.45) into (3.44) leads to

$$\{\hat{p}(\vec{x}_v;w)\}_{N\times 1} = [G_v(\vec{x}_v|\vec{x}_m)]_{N\times M}\langle\{\hat{v}_v(\vec{x}_m;w)\}_{M\times 1} + \{\varepsilon(\vec{x}_m;w)\}_{M\times 1}\rangle \tag{3.46}$$

where $\{\varepsilon(\vec{x}_m;w)\}_{M\times 1}$ is defined as

$$\{\varepsilon(\vec{x}_m;w)\}_{M\times 1} = \{\Delta\hat{v}_v(\vec{x}_v;w)\}_{M\times 1} \tag{3.47}$$

Eq. (3.46) has the same form as Eq. (3.26). The error analyses have shown that the magnitudes of errors are bounded and decrease monotonically as $r \to \infty$. This means that it is possible to extend the general solution (3.15) to a non-spherical surface whose aspect ratio is close to (1:1:1).

Once the acoustic pressure is determined, the particle velocity anywhere in the space can be reconstructed

$$\{\hat{v}_v(\vec{x}_m;w)\}_{N\times 1} = \frac{1}{iw\rho_0}[\nabla G_v(\vec{x}_v|\vec{x}_m)]_{N\times M}\langle\{\hat{v}_v(\vec{x}_m;w)\}_{M\times 1} + \{\varepsilon(\vec{x}_m;w)\}_{M\times 1}\rangle \quad (3.48)$$

Accordingly, the time-averaged acoustic intensity anywhere is given by

$$\hat{I}_{av}(\vec{x}_v;w) = \frac{1}{2}Re[\hat{p}(\vec{x}_v;w)\hat{v}_v^*(\vec{x}_v;w)] \quad (3.49)$$

Since the normal surface velocities are measured, the radiated acoustic power can be determined by multiplying them with the reconstructed acoustic pressure on the source surface.

$$P(w) = \frac{1}{2}Re\sum_{m=1}^{M}\langle\{\hat{p}(\vec{x}_m;w)\}_{1\times M}^{H}\{\hat{v}_v(\vec{x}_m;w)\}_{M\times 1}\rangle =$$

$$\frac{1}{2}Re\sum_{m=1}^{M}(\{\hat{p}(\vec{x}_m;w)\}_{1\times M}^{H})\,[G(\vec{x}_m|\vec{x}_m)]_{M\times M}\langle\{\hat{v}_v(\vec{x}_m;w)\}_{M\times 1} + \{\varepsilon(\vec{x}_m;w)\}_{M\times 1}\rangle \quad (3.50)$$

In this way, all acoustic quantities in the three-dimensional space are completely determined.

3.5 Comparison to traditional NAH method

In traditional NAH, input data is the acoustic pressure measured around a target source surface in the near field. Suppose that *M* measurement points are taken on a hologram surface that encircles the source surface. Then the acoustic pressure anywhere in the three-dimensional space can be written as

$$\{\hat{p}(\vec{x}_v;w)\}_{N\times 1} = \left[G_p(\vec{x}_v|\vec{x}_m;w)\right]_{N\times M}\{\hat{p}(\vec{x}_m;w)\}_{M\times 1} \quad (3.51)$$

where $\left[G_p(\vec{x}_v|\vec{x}_m;w)\right]_{N\times M}$ stands for the transfer function that correlates the acoustic pressure on the hologram surface to that in the three-dimensional space including the source surface, which is given by

$$\left[\mathrm{G_p}(\vec{\mathrm{x}}_\mathrm{v}|\vec{\mathrm{x}}_\mathrm{m};\mathrm{w})\right]_{\mathrm{N\times M}} = [\Psi(\vec{\mathrm{x}}_\mathrm{v};w)]_{N\times J}[\Psi(\vec{\mathrm{x}}_\mathrm{m};w)]^{\dagger}_{J\times M} \tag{3.52}$$

where the pseudo inversion in above equation is defined as

$$[\Psi(\vec{\mathrm{x}}_\mathrm{m};w)]^{\dagger}_{J\times M} = \left([\Psi(\vec{\mathrm{x}}_\mathrm{m};w)]^{H}_{J\times M}[\Psi(\vec{\mathrm{x}}_\mathrm{m};w)]_{M\times J}\right)^{-1}[\Psi(\vec{\mathrm{x}}_\mathrm{m};w)]^{H}_{J\times M} \tag{3.53}$$

The main difference between NAH method and HELS based NAH with laser could be summed as

(1) The NAH method has a transfer function that consists of the basis functions only, while surface velocity based HELS method involves a transfer function that contains both the basis functions and their normal derivatives;

(2) The former takes the acoustic pressures measured in the near field as its input data, whereas the latter utilizes the normal surface velocities measured directly on the source surface as its input data.

These differences have direct impacts on the characteristics of the reconstructed acoustic quantities.

Following the same procedures as outlined in Section 3.4, we can analyze the errors in the reconstructed acoustic pressure. In this case, the elements of the transfer function in the Eq. (3.51) are proportional to

$$G_p(\vec{x}_v|\vec{x}_m;w) \propto \frac{h_n^{(1)}(\chi)Y_n^l(\theta,\varphi)}{h_n^{(1)}(\chi_m)Y_n^l(\theta_m,\varphi_m)} \tag{3.54}$$

where $\chi = kr$ *and* $\chi_m = k\xi_m$.

CHAPTER 4

NUMERICAL SIMULATIONS

In this chapter, numerical simulations will be conducted to demonstrate the outstanding advantages and effectiveness of this modified HELS method based on laser. The simulation setup is showed as follows:

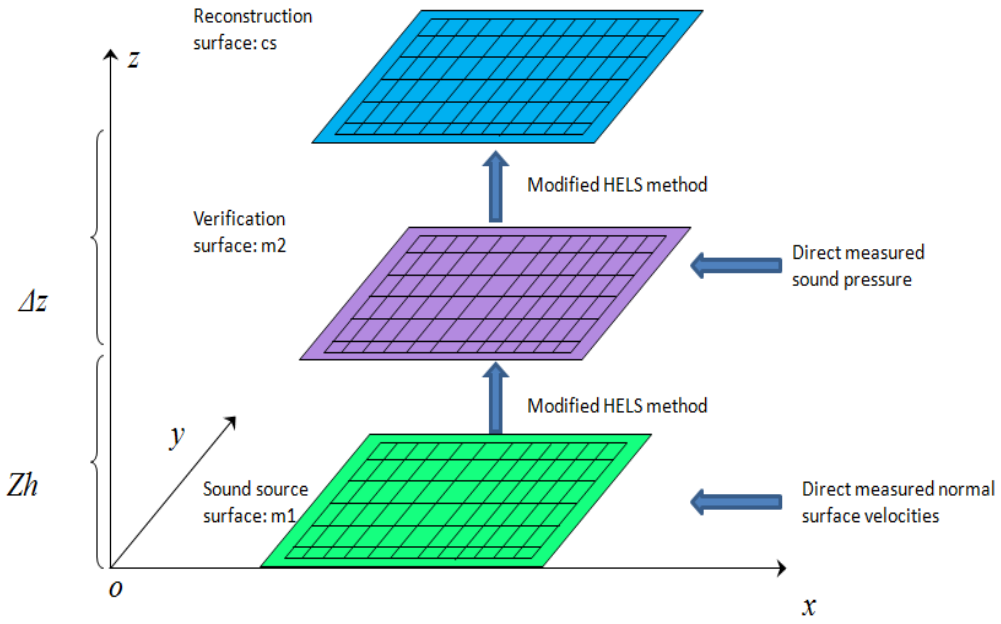

Figure 4.1 Diagram of simulation setup

The figure illustrates the simulation setup of HELS based NAH with laser. The target sound source is placed in the center. Normal surface velocity distribution on this sound source surface is measured by laser vibrometer. Meanwhile, the sound pressure and particle velocity on verification surface will be used as benchmarks for reconstruction. Subsequently, the modified HELS based NAH is employed to reconstruct the sound field on verification surface *m2* using the normal surface velocity as input. Least square method minimizes the errors and then the

optimal number of expansion terms is decided consequently. Finally, HELS based NAH with laser can be applied to reconstruct sound field on interested surface.

4.1 Numerical validation on a monopole

Acoustic monopole is a simple sound source. This kind of sound source alternately expands and contracts to change its volume periodically. Sound and energy radiated from an acoustic monopole will distribute uniformly in every direction. Practically, those sound sources whose dimensions and sizes are very small compared with the wavelength of the sound will be treated as monopoles to simplify the process of modeling and calculation [71-74].

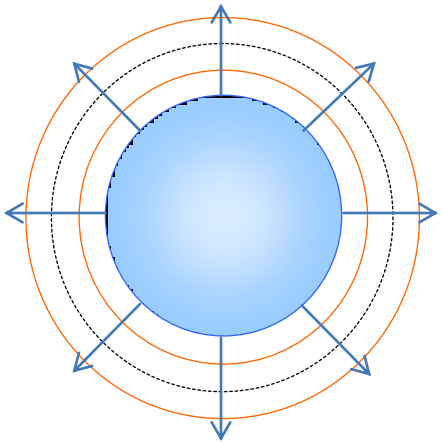

Figure 4.2 Monopole sound source

The acoustic pressure field radiated by a point monopole source at the frequency $\omega = 2\pi f$ could be presented as [74]:

$$\hat{P}(r) = -\frac{iQk\rho c}{4\pi r} e^{ik(r-ct)} = -\frac{iQk\rho c}{4\pi r} e^{ikr} e^{-iwt} \tag{4.1}$$

where k is the wave number, w is the frequency, $k=w/c$, ρ is the density of media, c is the speed of sound, and r is the radius from source to observation point. Q is the complex source strength

and a constant which can be calculated as the product of the surface area and the normal surface velocity of the monopole.

The sound pressure radiation by the monopole is presented in a polar figure as follows:

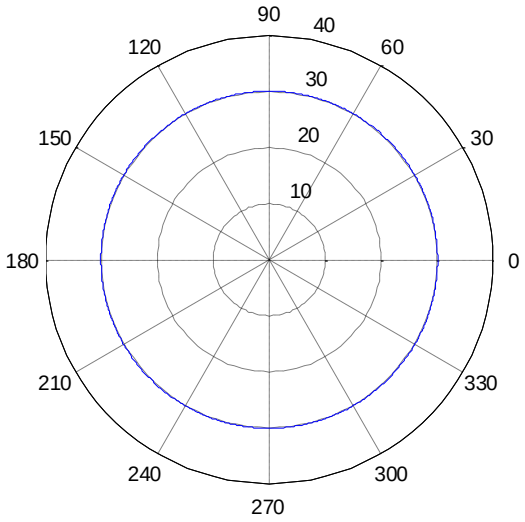

Figure 4.3 Acoustic pressure field generated by a monopole

When $\rho = 1.2041\ kg/m^3$, $c = 343.26\ m/s$, $r = 1\ m$, $f = 50\ Hz$. For the convenience of calculation, the complex source strength is set as 1.

From Euler's formula, the particle velocity of the monopole sound source can be derived as follows:

$$\widehat{U}_r = -\frac{1}{iw\rho}\frac{\partial \hat{p}(r)}{\partial r} = \frac{(1-ikr)Q}{4\pi r^2}e^{ik(r-ct)} = \frac{(1-ikr)Q}{4\pi r^2}e^{ikr}e^{-iwt} \tag{4.2}$$

HELS based NAH with laser is employed to reconstruct the acoustic sound field for a monopole in 4 different cases.

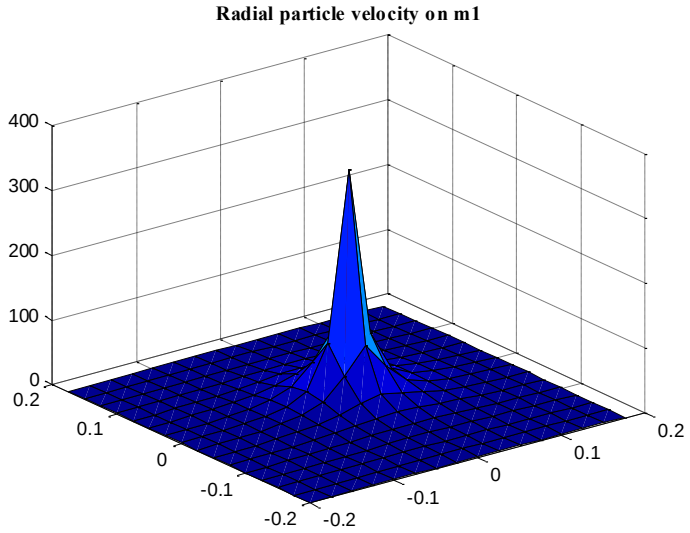

Figure 4.4 Particle velocity on m1 surface generated by a monopole

Case 1: near field, no back ground noise, frequency=50 Hz;

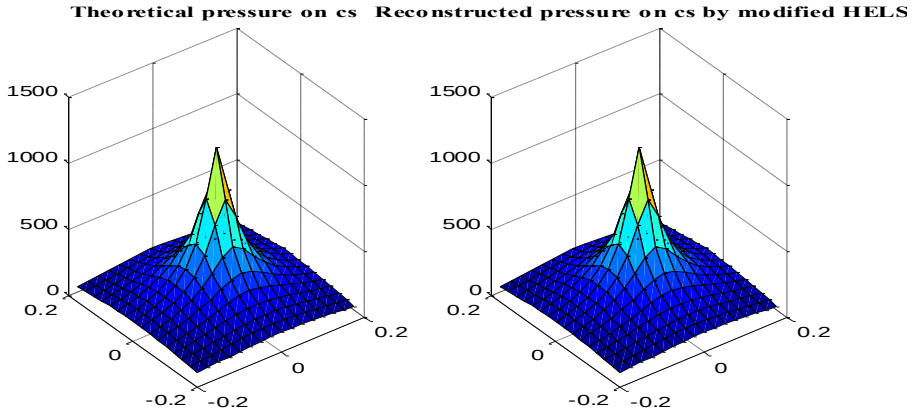

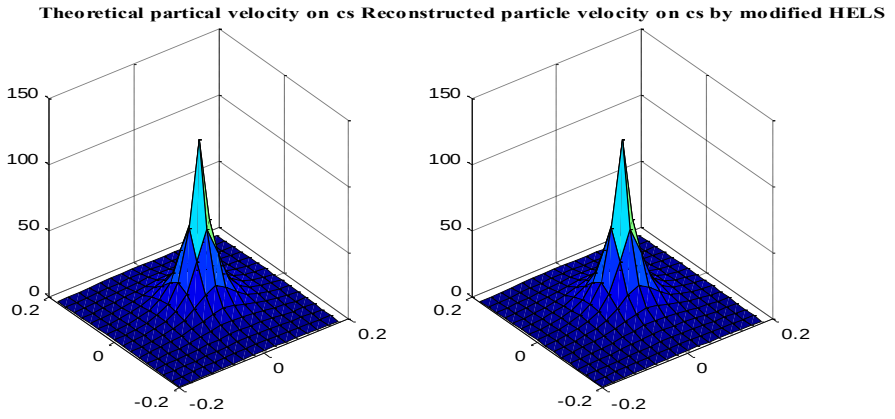

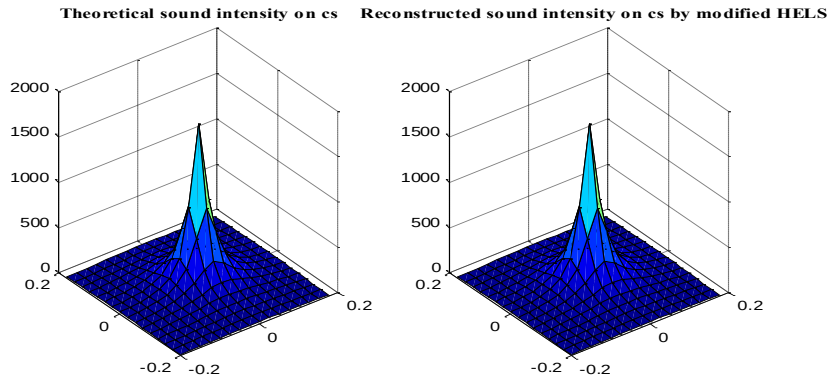

Figure 4.5 Analysis of reconstructed sound field from a monopole (case 1: near field, no back ground noise, frequency=50 Hz ;)

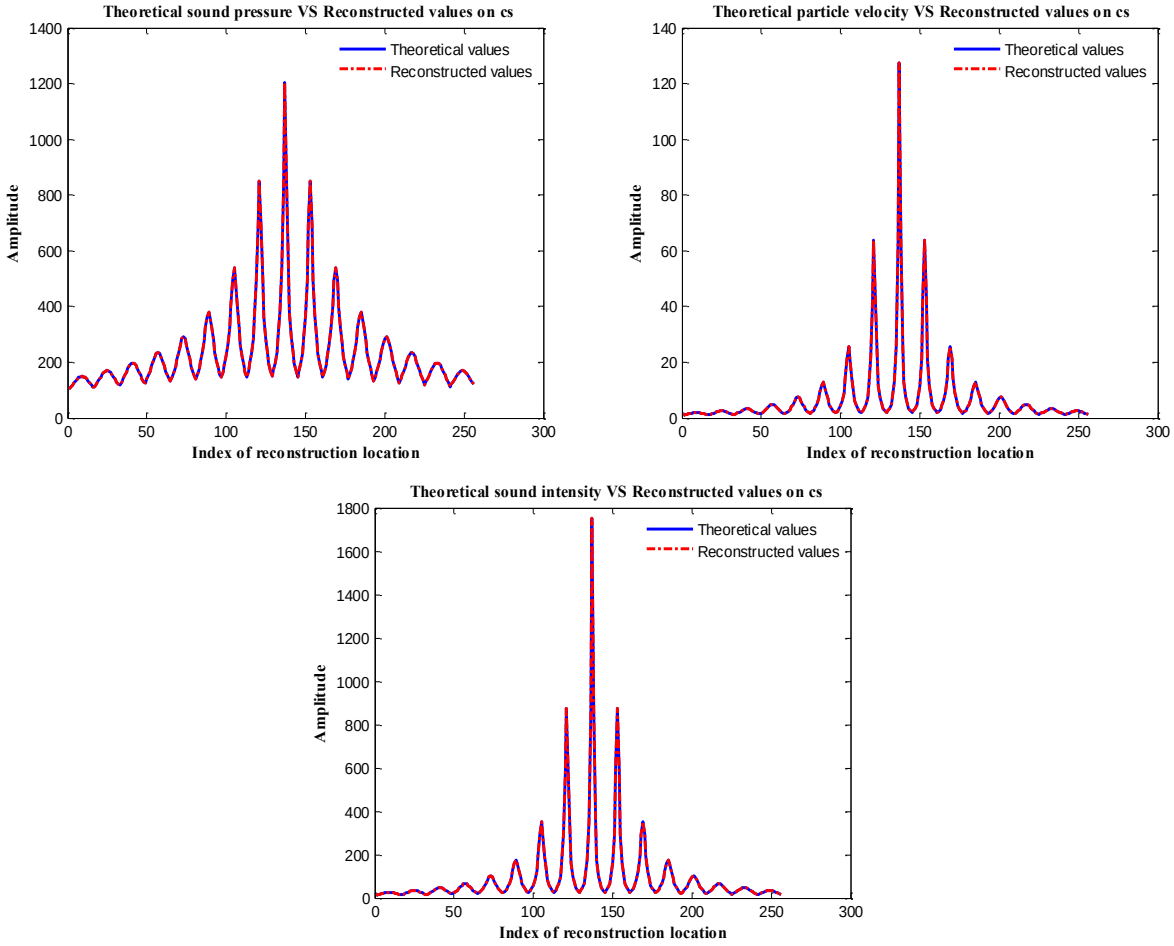

Figure 4.6 Comparison of reconstructed sound field from a monopole by point index (case 1: near field, no back ground noise, frequency=50 Hz ;)

Case 2: far field, no back ground noise, frequency=50 Hz;

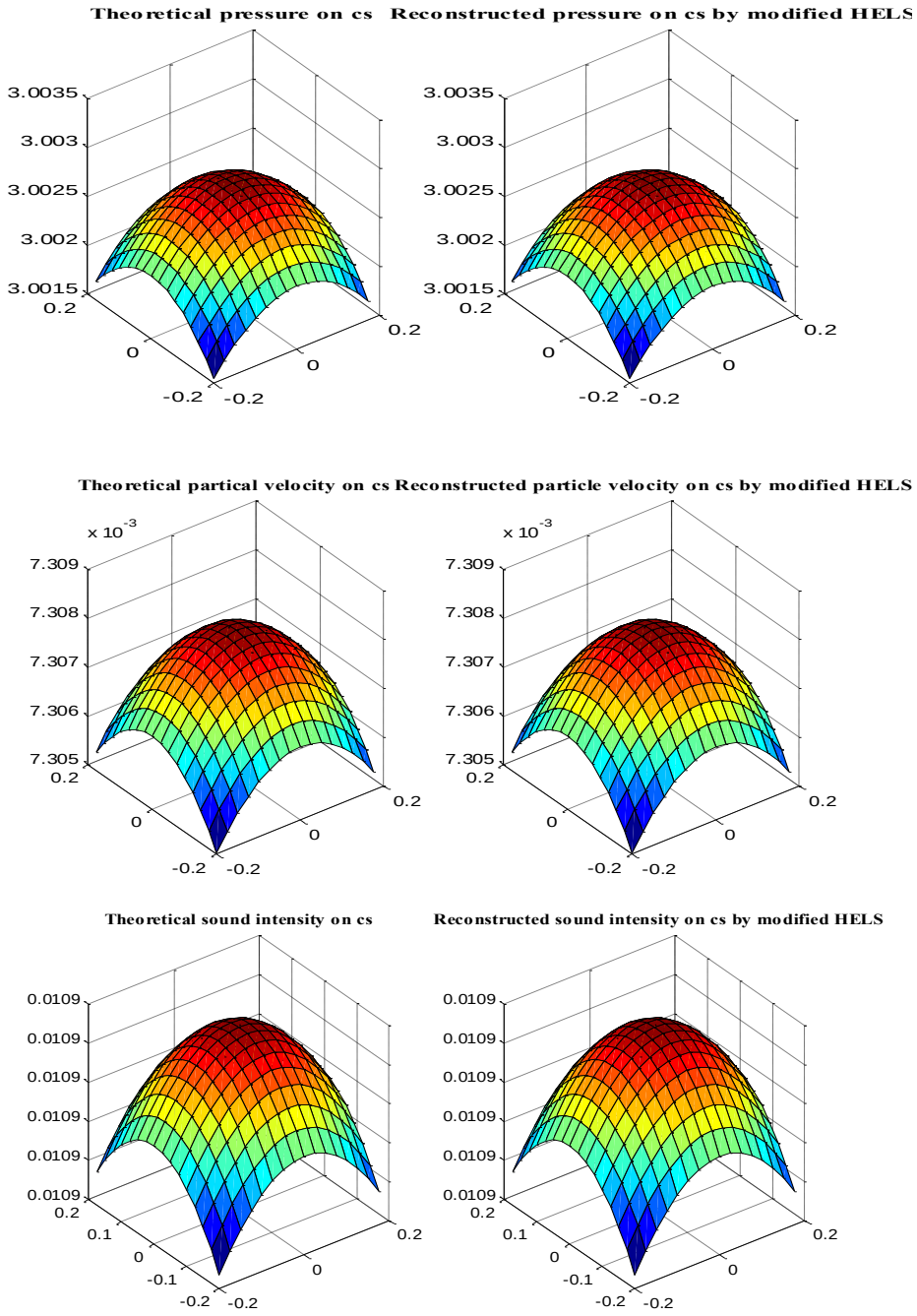

Figure 4.7 Analysis of reconstructed sound field from a monopole (case 2: far field, no back ground noise, frequency=50 Hz ;)

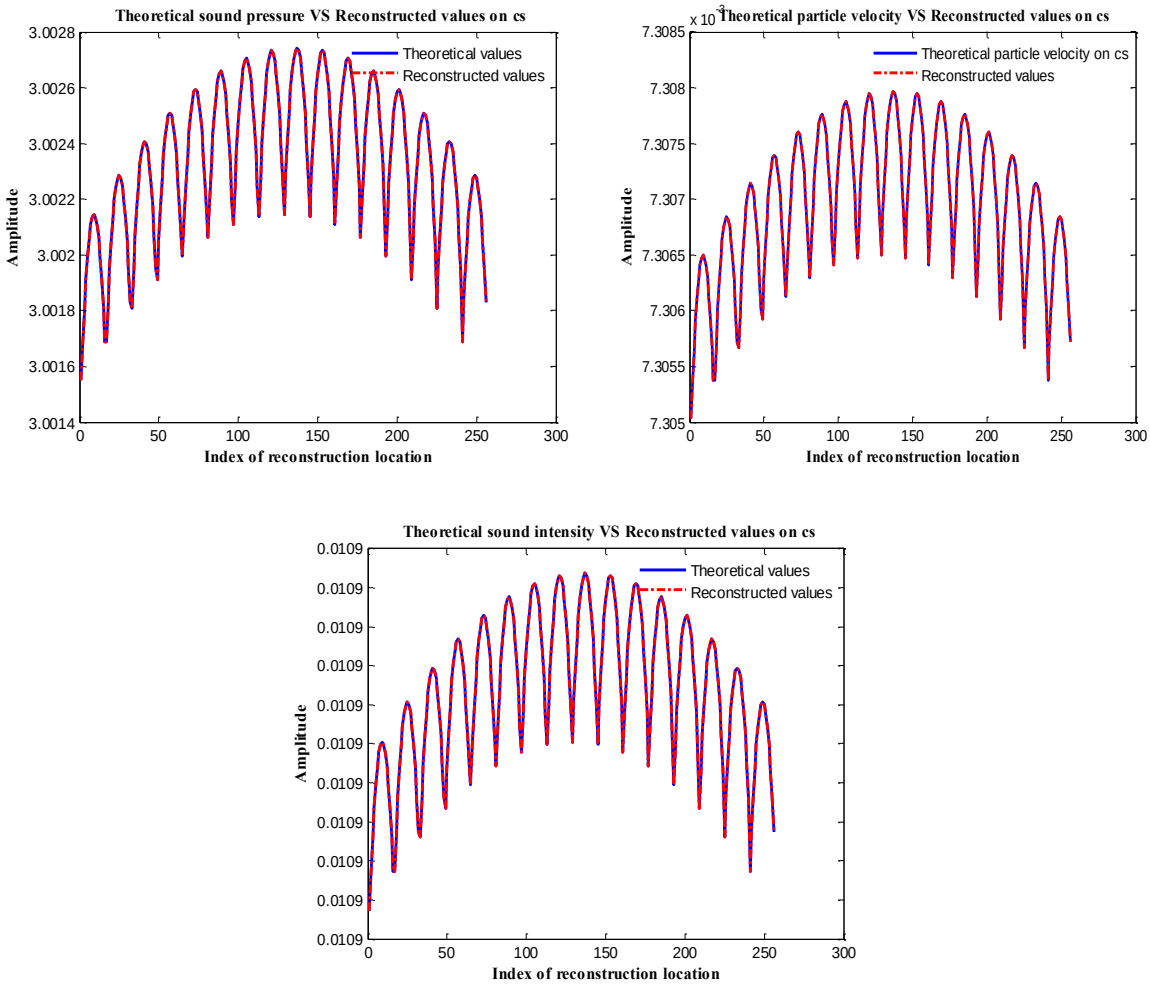

Figure 4.8 Comparison of reconstructed sound field from a monopole by point index (case 2: far field, no back ground noise, frequency=50 Hz ;)

Case 3: near field, back ground noise, frequency=50 Hz;

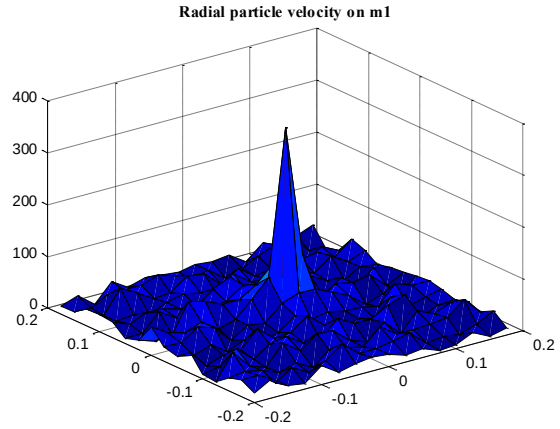

Figure 4.9 Particle velocity on m1 surface with back ground noise generated by a monopole

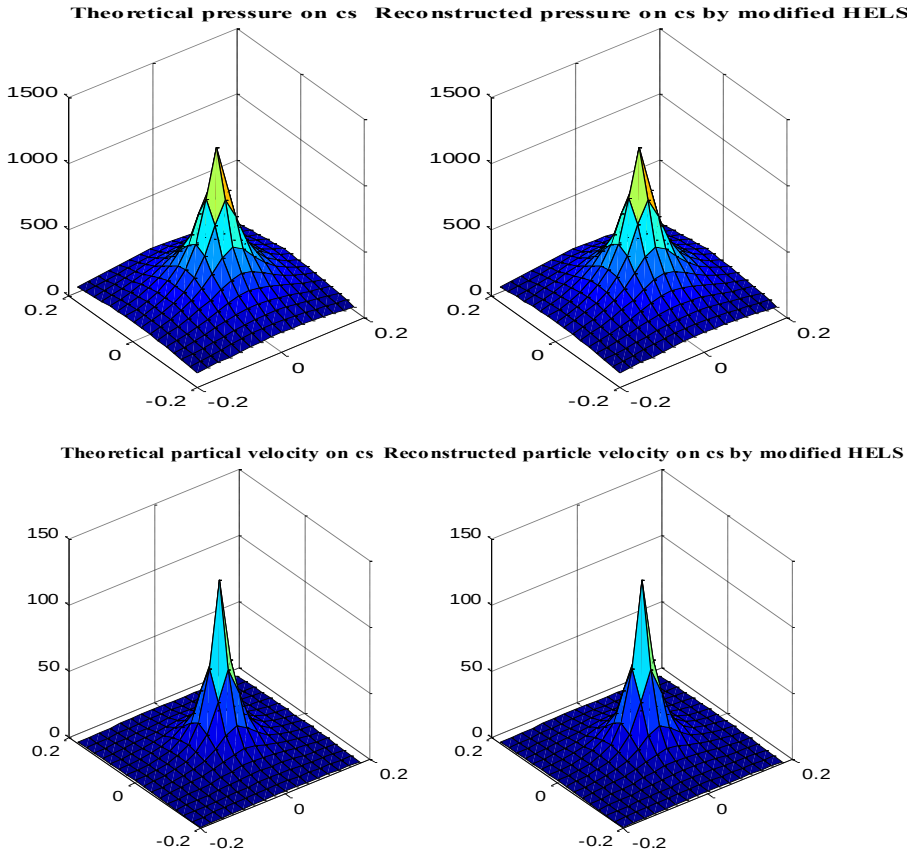

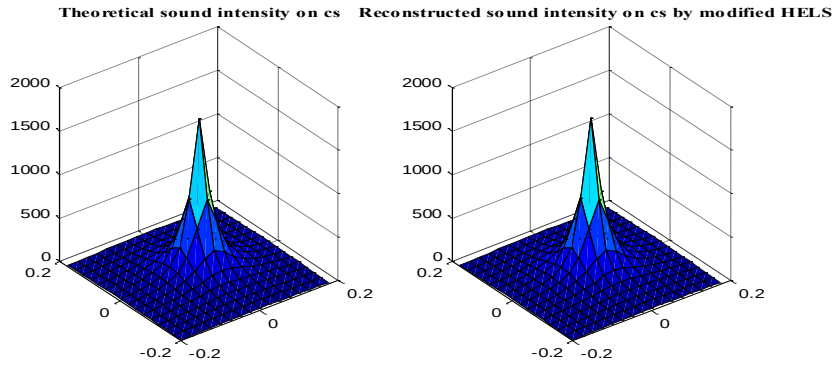

Figure 4.10 Analysis of reconstructed sound field from a monopole (case 3: near field, back ground noise, frequency=50 Hz ;)

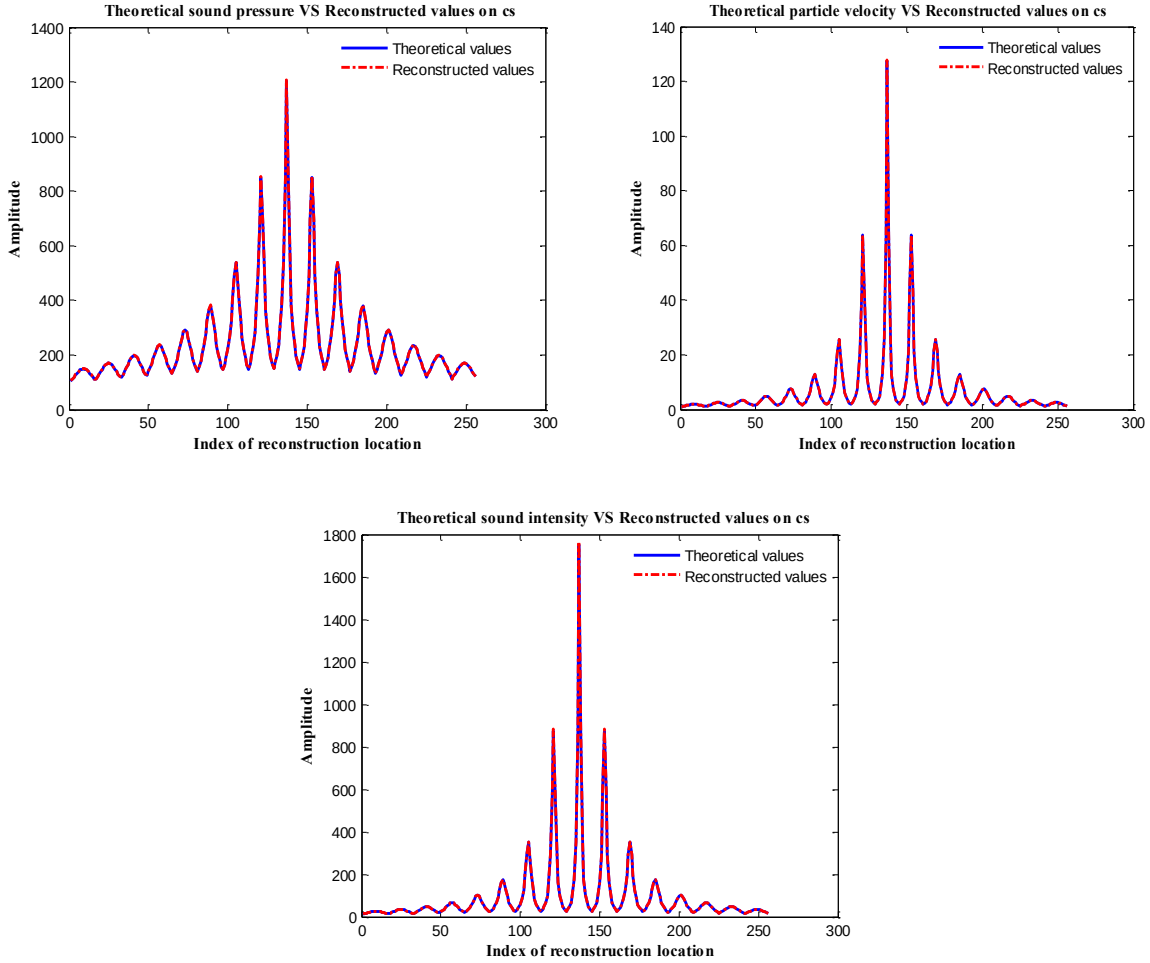

Figure 4.11 Comparison of reconstructed sound field from a monopole by point index (case 3: near field, back ground noise, frequency=50 Hz ;)

Case 4: far field, back ground noise, frequency=50 Hz;

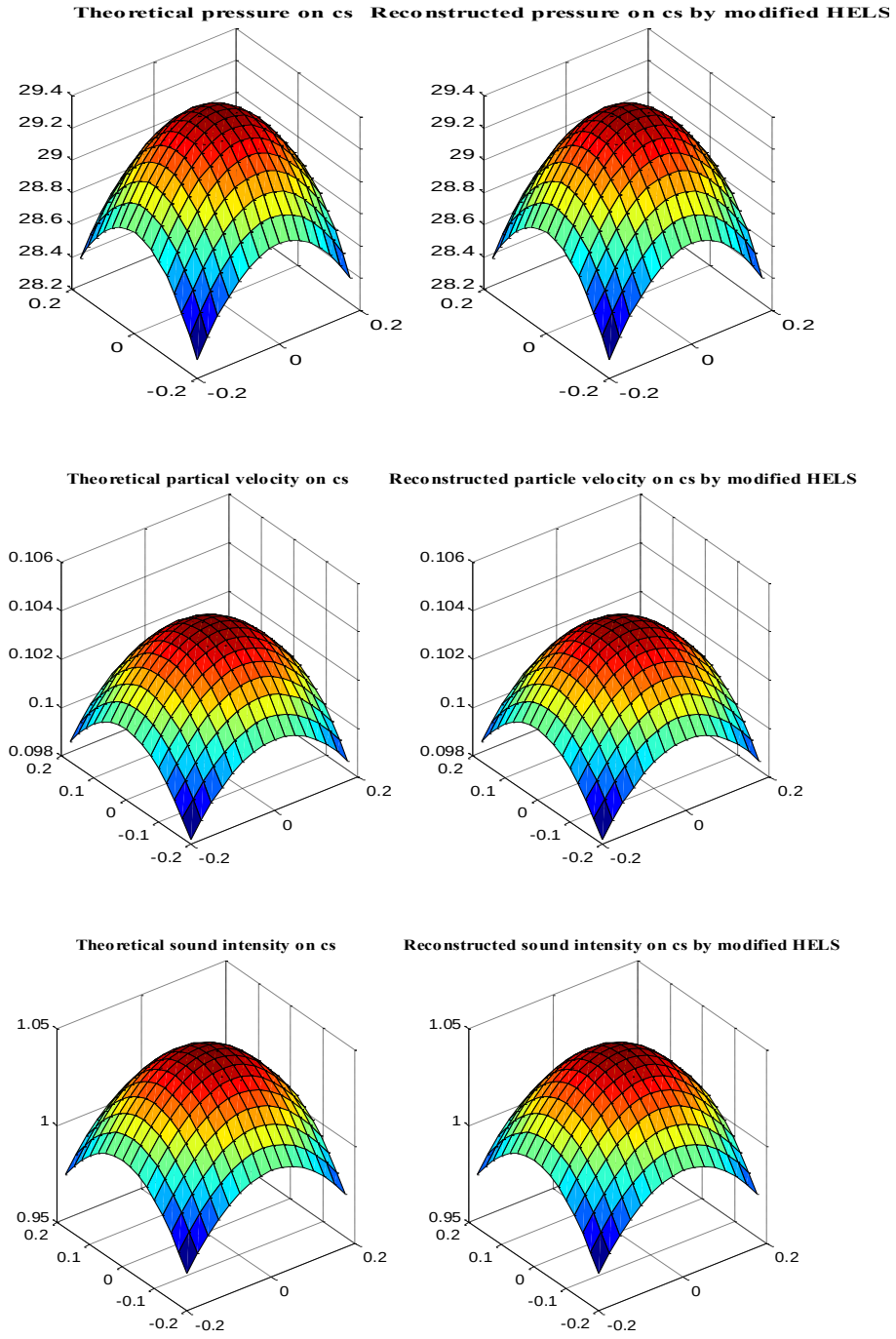

Figure 4.12 Analysis of reconstructed sound field from a monopole (case 4: far field, back ground noise, frequency=50 Hz ;)

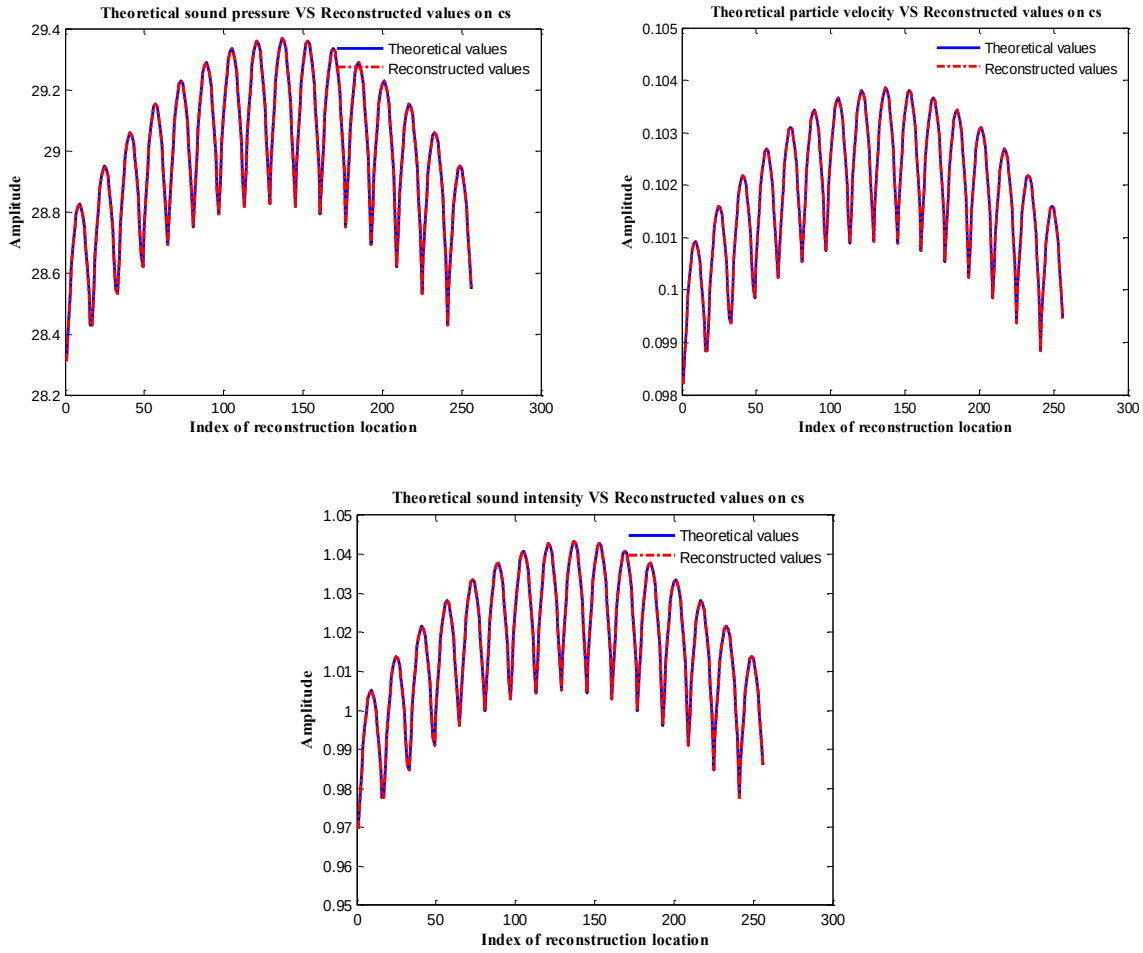

Figure 4.13 Comparison of reconstructed sound field from a monopole by point index (case 4: far field, back ground noise, frequency=50 Hz ;)

From the simulation study of the above 4 different cases, HELS based NAH with laser is able to reconstruct the sound field of a monopole with a high accuracy in different scenarios. By the comparison of case 1 and 2, the new method can finish the reconstruction in both near-field and far-field. Through the comparison between case 1 and 3 or case 2 and 4, it shows that the HELS based NAH with laser is robust even when background noise is presented.

4.2 Numerical validation on a dipole

When two monopoles of equal sound strength are placed together with a small distance to separate them, this combination forms a point dipole source. There is a phase difference between these two monopoles. When one monopole radiates forward, the other source contracts backward. Then, the fluid is introduced and withdrawn between these two sources.

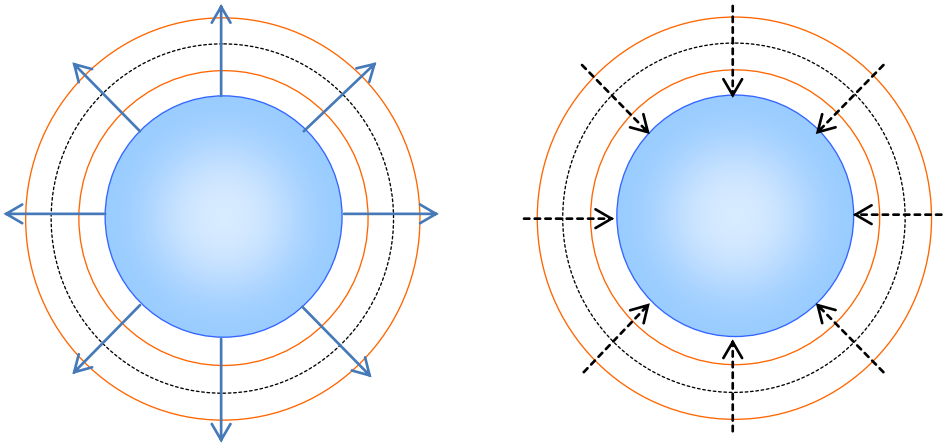

Figure 4.14 Dipole sound source

The acoustic pressure field radiated by a point dipole sound source at the frequency $\omega = 2\pi f$ could be presented as [71, 74, 75]:

$$\hat{P}(r) = -\frac{Qk^2\rho c}{4\pi r}\left(1+\frac{i}{kr}\right)\cos(\vartheta)\, e^{ik(r-ct)}$$

$$= -\frac{Qk^2\rho c}{4\pi r}\left(1+\frac{i}{kr}\right)\cos(\vartheta) e^{ik(r-ct)} e^{ikr} e^{-iwt} \tag{4.3}$$

The particle velocity of the dipole sound source could be derived like following:

$$\hat{U}_r = -\frac{1}{iw\rho}\frac{\partial \hat{p}(r)}{\partial r} = \frac{-Qk^2}{4\pi r}\cos(\vartheta)\left(1+\frac{2i}{kr}-\frac{2}{k^2r^2}\right)e^{ik(r-ct)}$$

$$= \frac{-Qk^2}{4\pi r}\cos(\vartheta)\left(1+\frac{2i}{kr}-\frac{2}{k^2r^2}\right)e^{ikr}e^{-iwt} \tag{4.4}$$

The sound pressure radiation by the dipole is presented in a polar figure as follows:

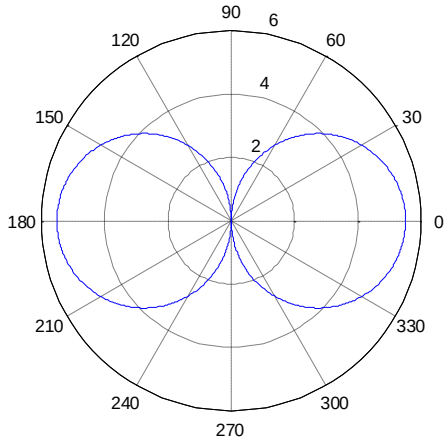

Figure 4.15 Acoustic pressure field generated by a dipole

HELS based NAH with laser is used to reconstruct the transient acoustic sound field from a dipole source.

Case 1: near-field, no back ground noise, frequency=50 Hz;

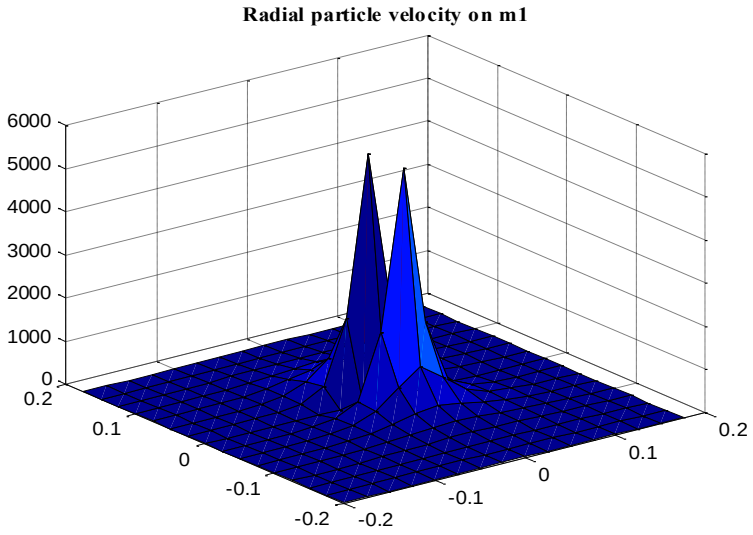

Figure 4.16 Particle velocity on m1 surface generated by a dipole

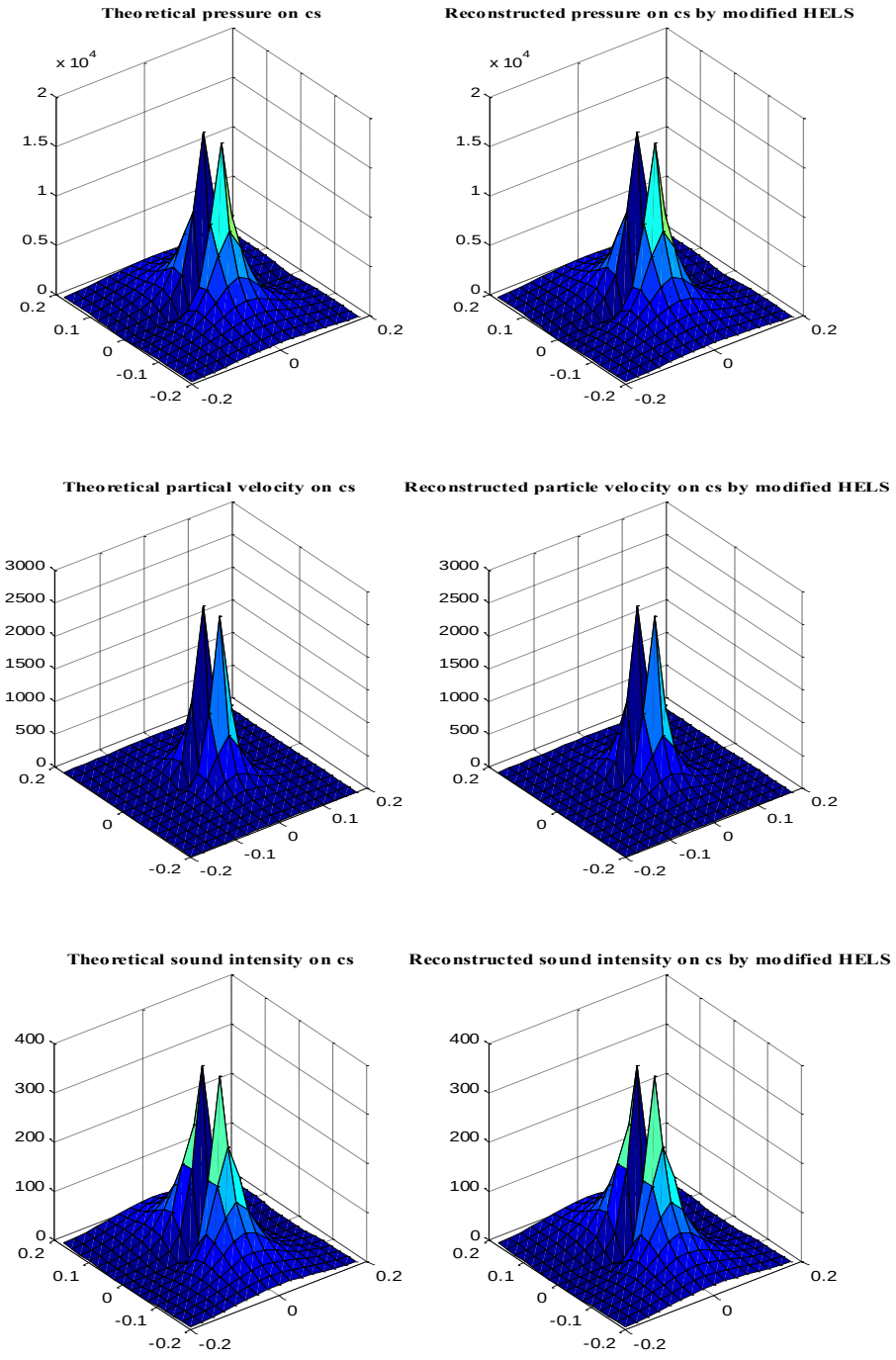

Figure 4.17 Comparison of reconstructed sound field from a dipole by point index (case 1: near-field, no back ground noise, frequency=50 Hz ;)

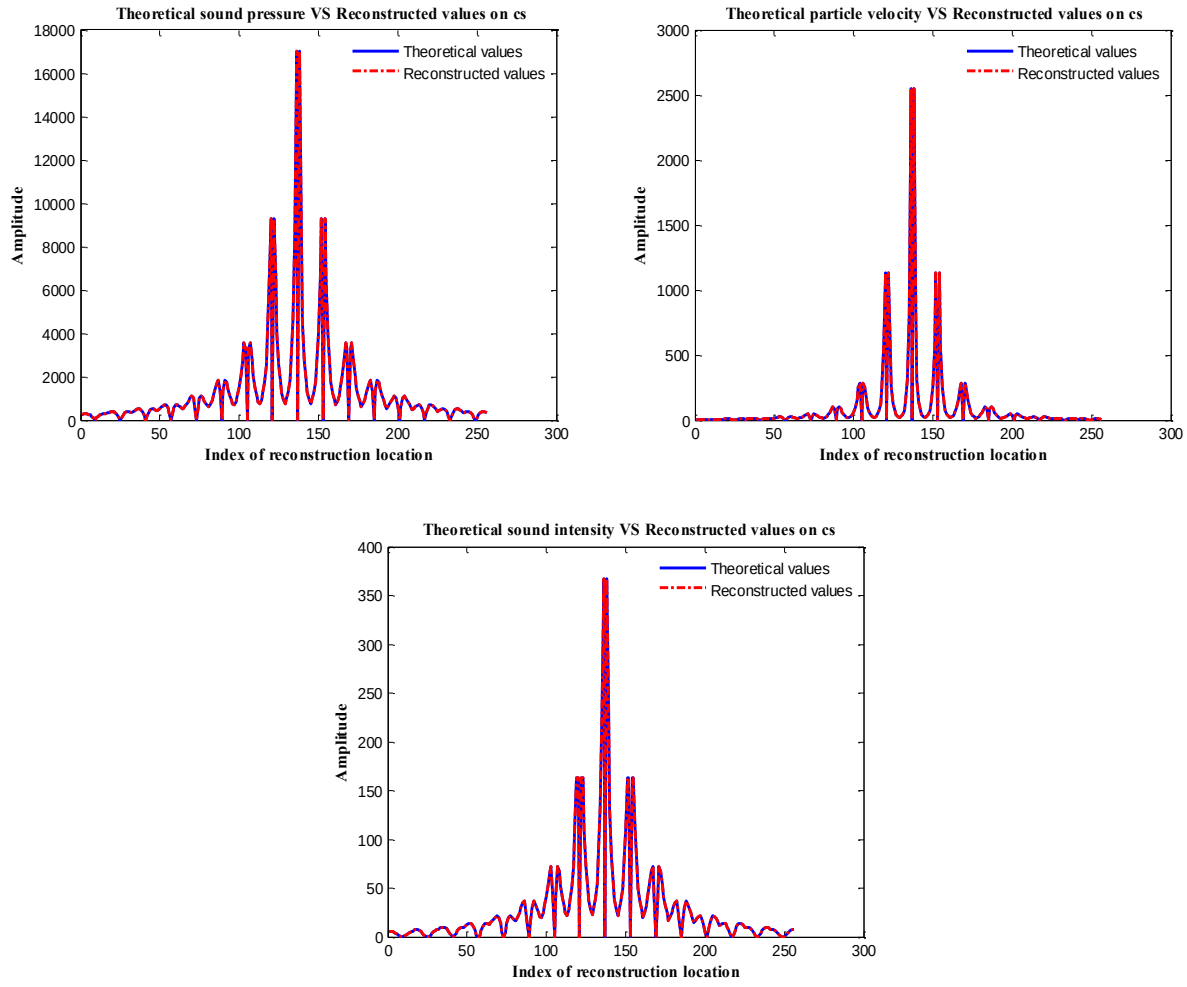

Figure 4.18 Comparison of reconstructed sound field from a dipole by point index (case 1: near-field, no back ground noise, frequency=50 Hz ;)

Case 2: far field, no back ground noise, frequency=50 Hz;

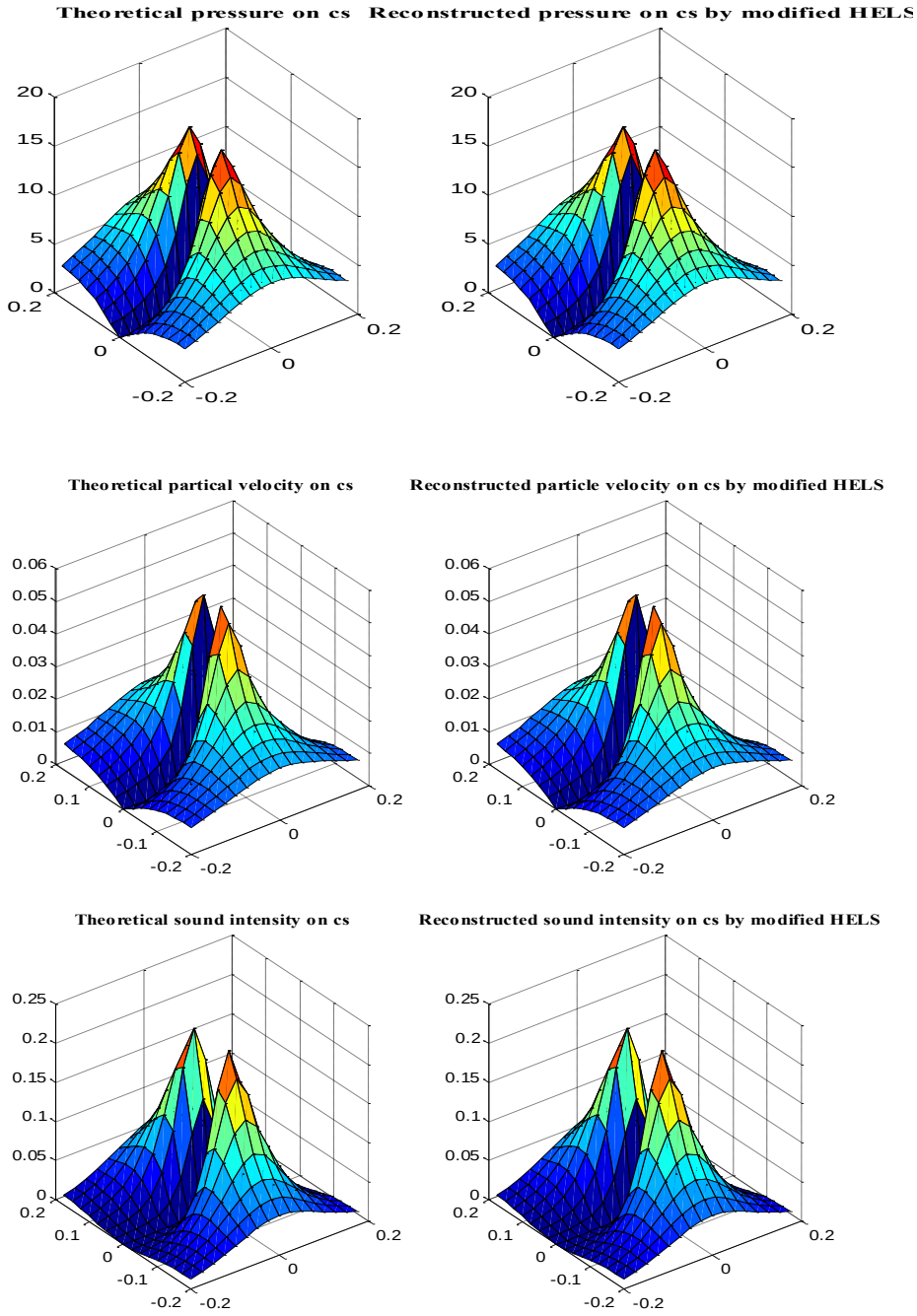

Figure 4.19 Analysis of reconstructed sound field from a dipole (case 2: far field, no back ground noise, frequency=50 Hz ;)

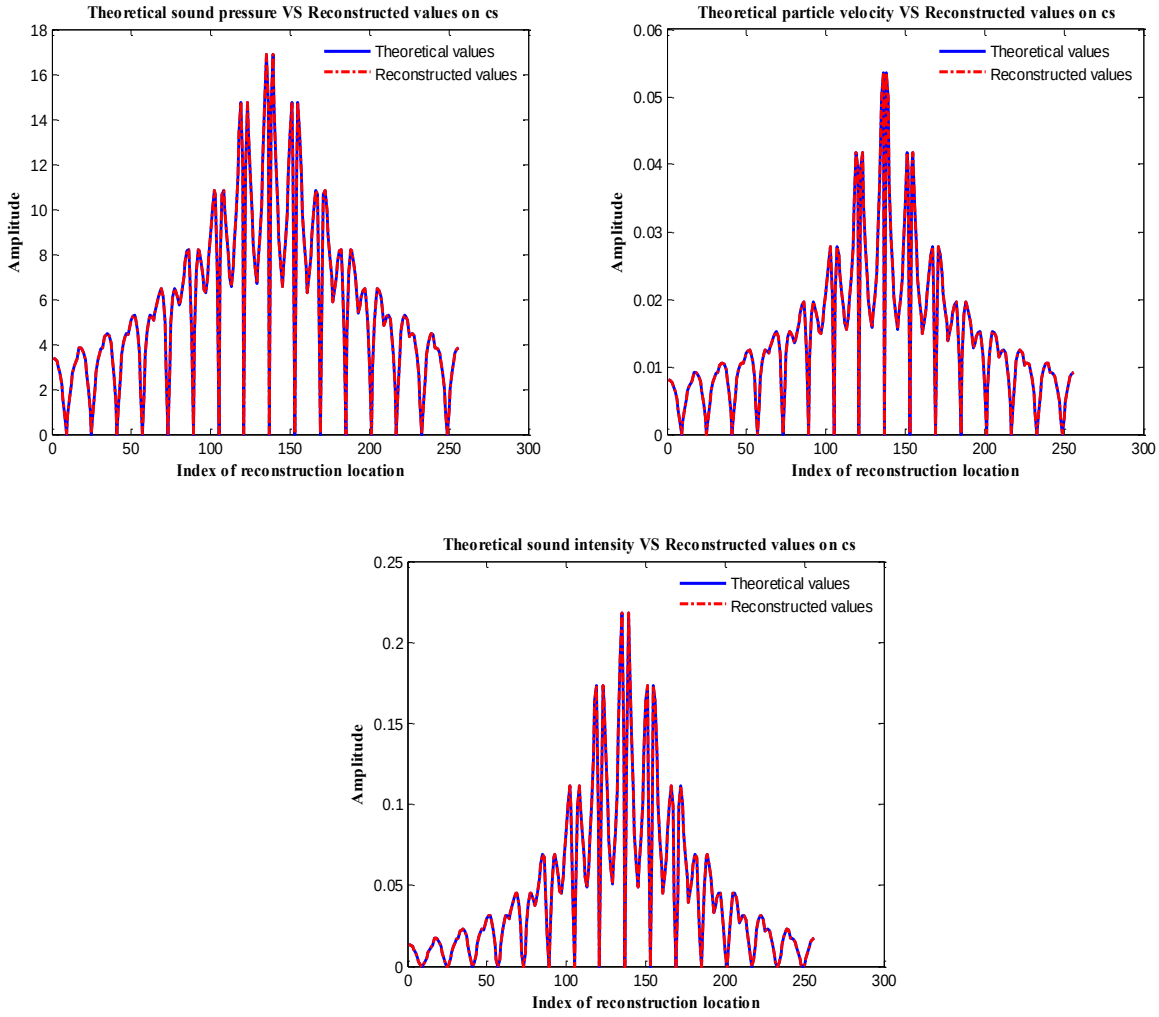

Figure 4.20 Comparison of reconstructed sound field from a dipole by point index (case 2: far field, no back ground noise, frequency=50 Hz ;)

Case 3: near field, back ground noise, frequency=50 Hz;

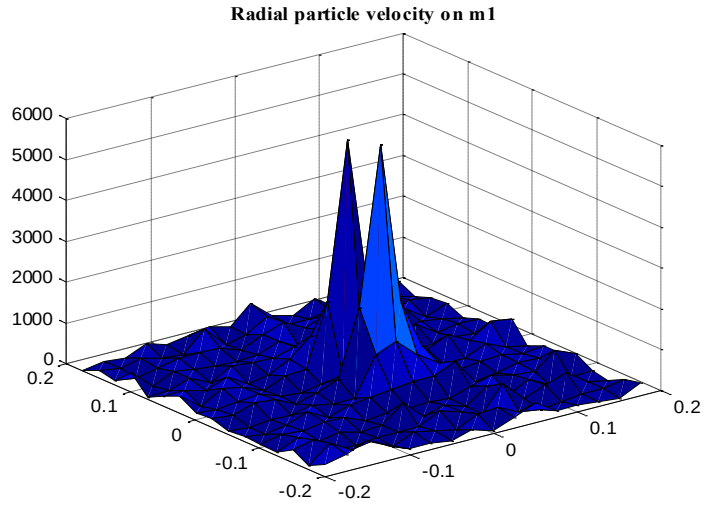

Figure 4.21 Particle velocity on m1 surface with background noise from a dipole

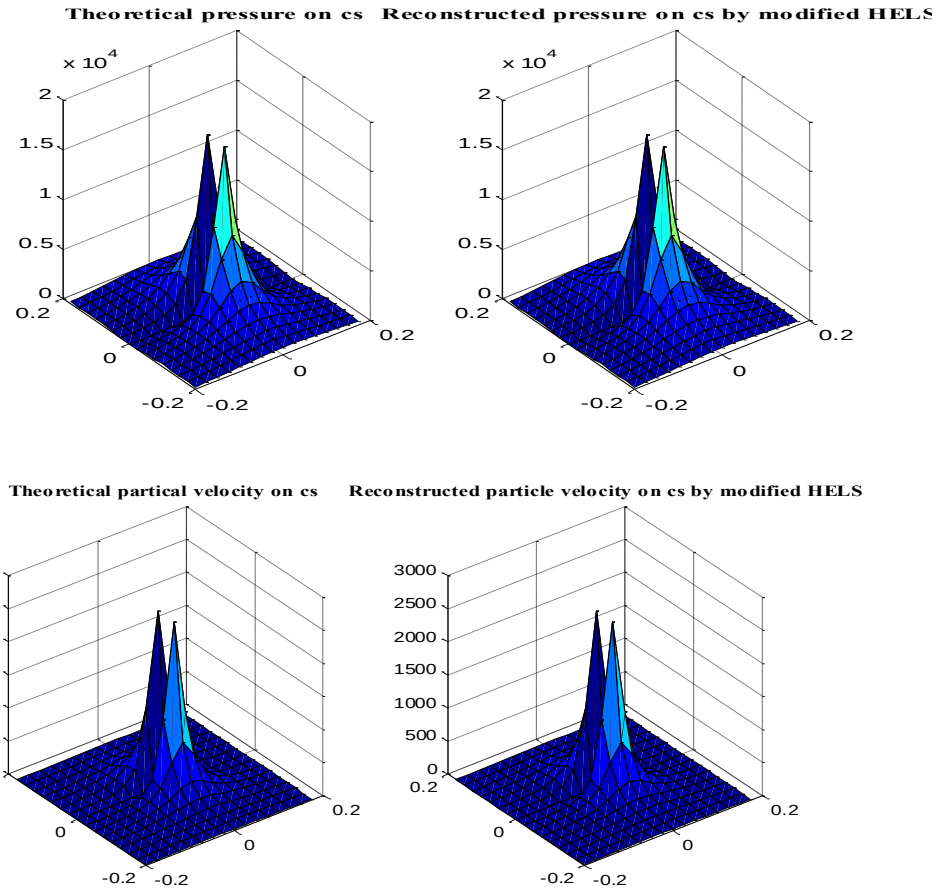

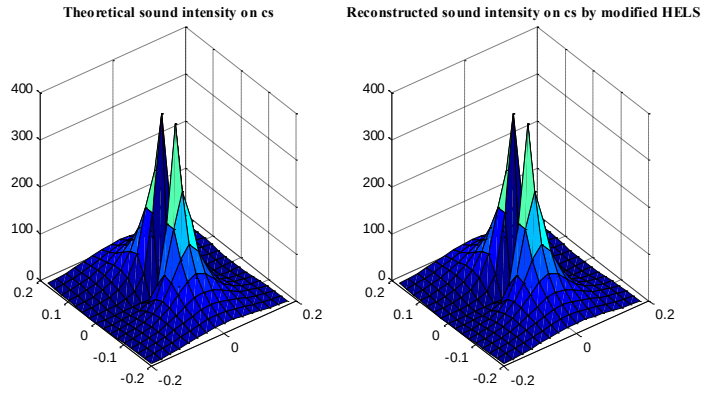

Figure 4.22 Analysis of reconstructed sound field from a dipole (case 3: near field, back ground noise, frequency=50 Hz ;)

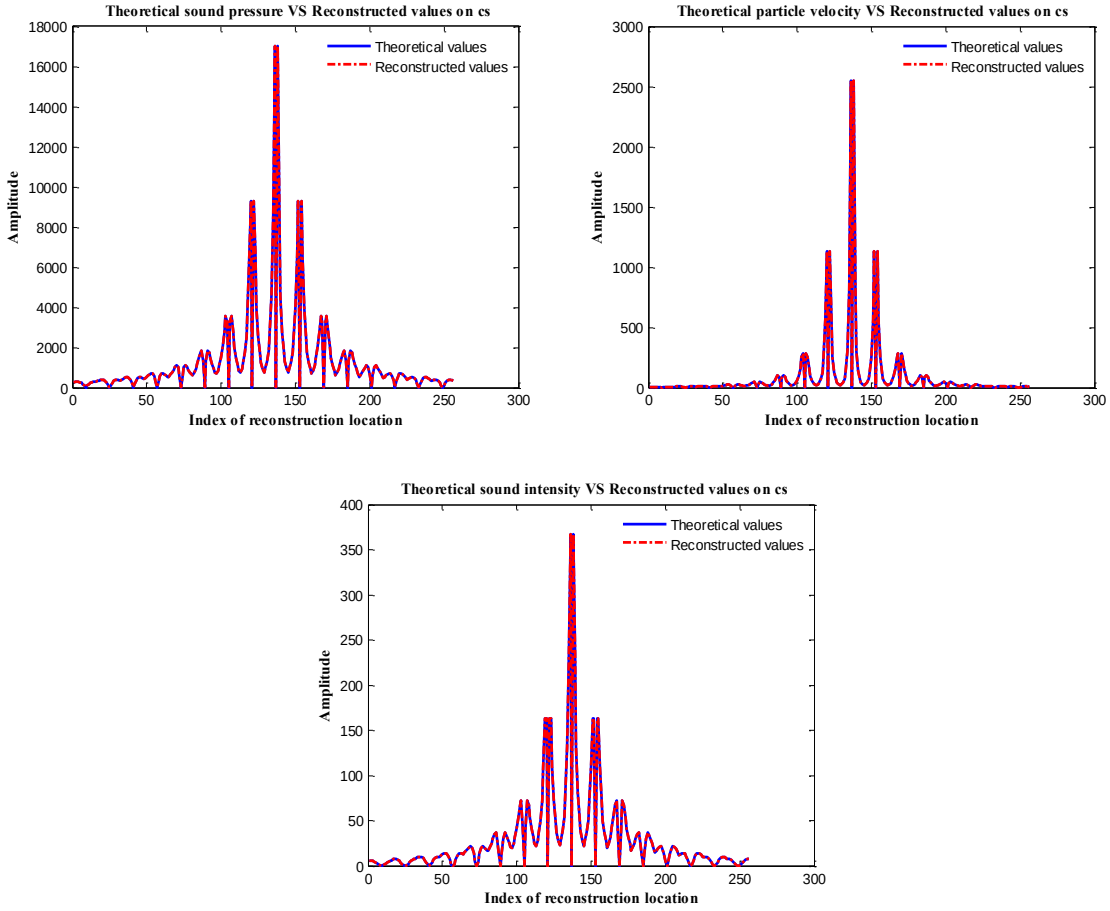

Figure 4.23 Comparison of reconstructed sound field from a dipole by point index (case 3: near field, back ground noise, frequency=50 Hz ;)

Case 4: far field, back ground noise, frequency=50 Hz;

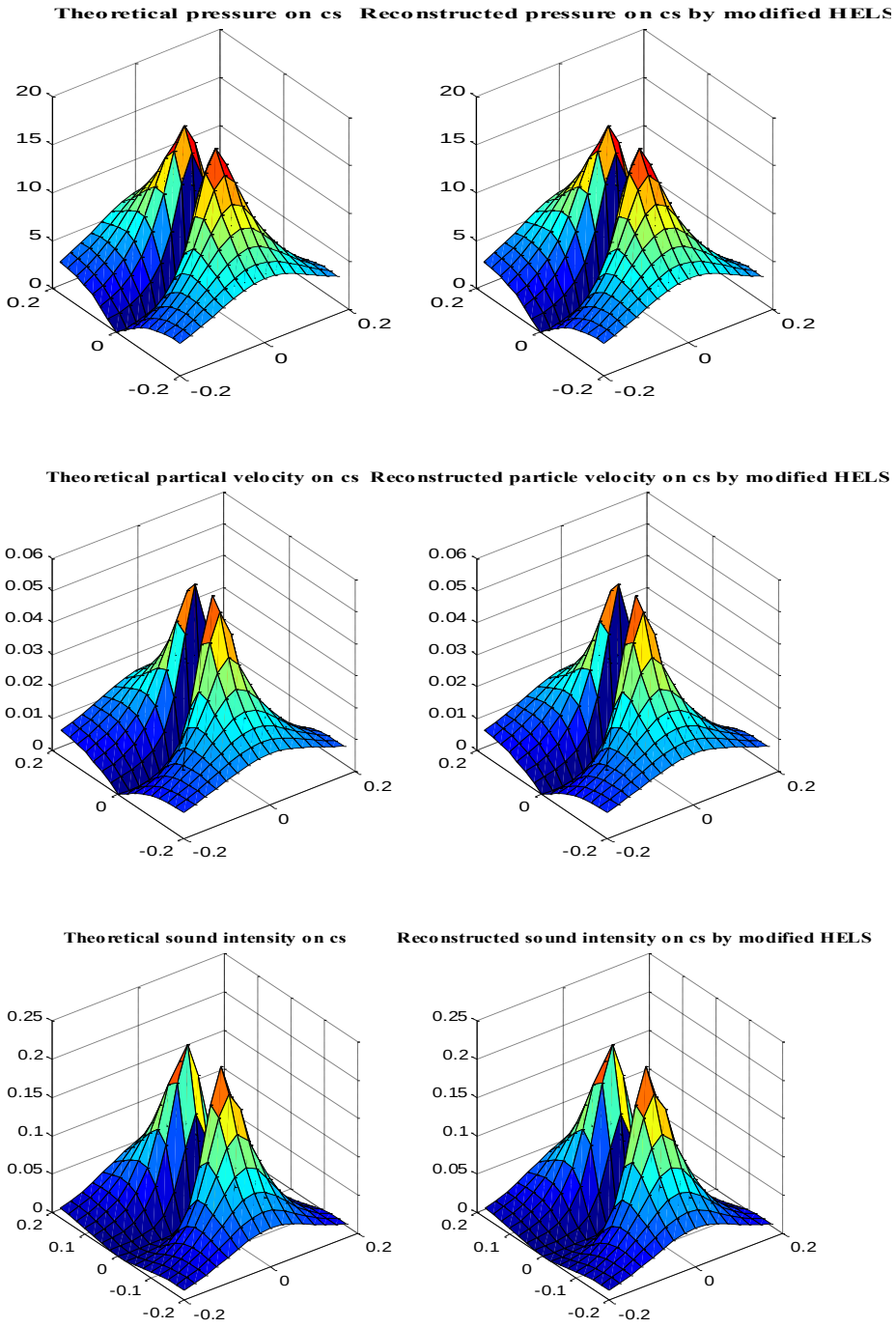

Figure 4.24 Analysis of reconstructed sound field from a dipole (case 4: far field, back ground noise, frequency=50 Hz ;)

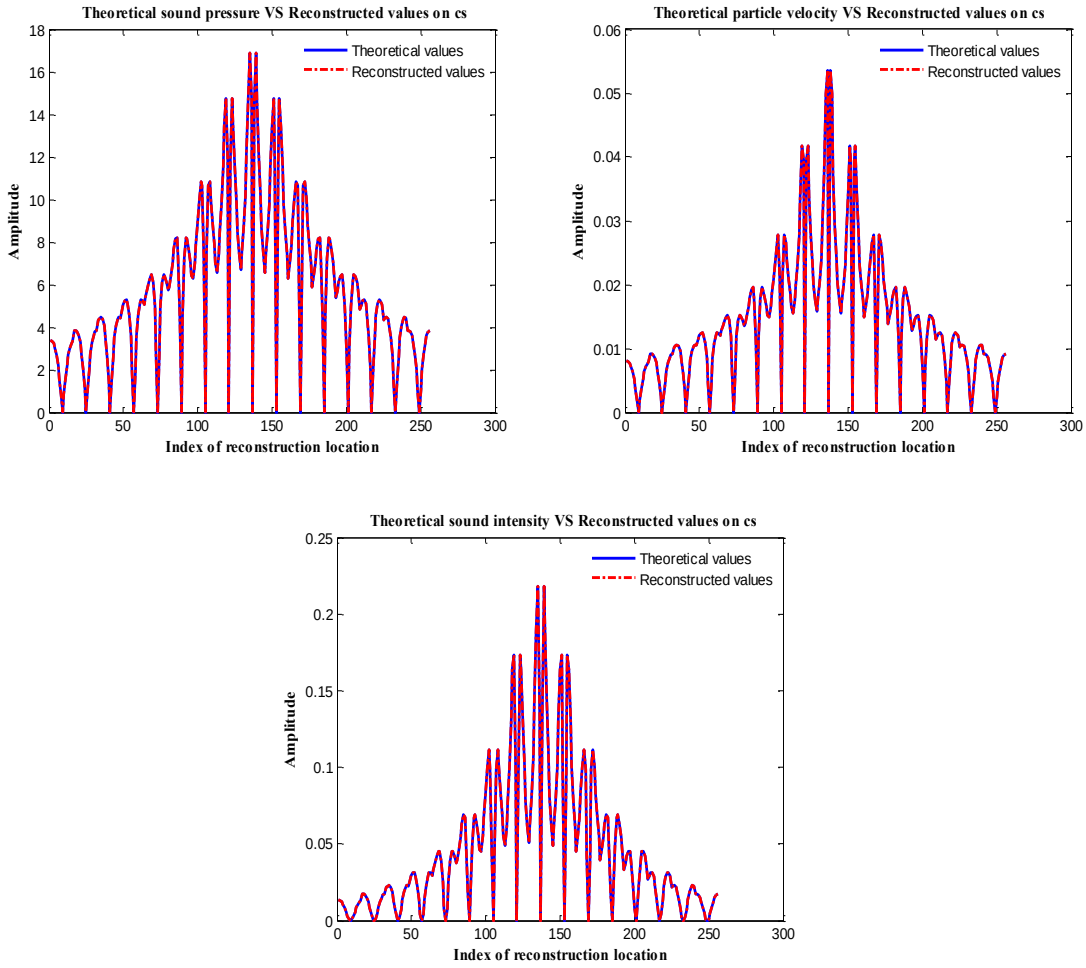

Figure 4.25 Comparison of reconstructed sound field from a dipole by point index (case 4: far field, back ground noise, frequency=50 Hz ;)

From the results of a monopole and a dipole in four different cases, it shows that HELS based NAH with laser has reconstructed sound field with a high level of accuracy in various working conditions for a dipole source. By way of the comparison between different cases, the modified HELS method demonstrates that it is applicable ranging from near-field to far-field and it is reliable even when the input is polluted.

4.3 Plate vibration problem

After the study of sound field reconstructions about two ideal sound sources, the next simulation example is to numerically verify the effectiveness of this HELS based NAH with laser in dealing with reconstruction of vibro-acoustic response for highly non-spherical structures.

For thin plates with side to thickness ratio greater than 30, the classical thin plate theory is developed based on Kirchhoff hypothesis [72, 76, 77]:

(1) Straight lines perpendicular to the mid-surface of the plate before deformation remain straight after deformation. Also, the length of straight lines keeps the same.

(2) The transverse normal remain perpendicular to the neutral plane after deformation, and there is no deformation which is parallel to the neutral surface.

(3) The stress components that perpendicular to the neutral plane are far smaller than other stress components. Therefore, there is not any elongation for planes in transversal directions.

(4) Effect of rotatory inertia is negligible.

The governor equation for free vibration of isotropic plates with uniform thickness is given by [78, 79]:

$$D\nabla^4 w + \rho h \frac{\partial^2 w}{\partial t^2} = 0 \tag{4.5}$$

where: w is the transverse displacement of the thin plate;

ρ is the density of the material of the thin plate;

h is the uniform thickness of the plate;

D is the flexural rigidity and $D = \frac{Eh^3}{12(1-\vartheta^2)}$;

E is the Young's modulus of elasticity;

ϑ is the Poisson's ratio;

t is time;

∇^4 is the biharmonic operator

$$\nabla^4 w = \frac{\partial^4 w}{\partial x^4} + 2\frac{\partial^4 w}{\partial x^2 \partial y^2} + \frac{\partial^4 w}{\partial y^4} \tag{4.6}$$

$\nabla^4 w = \nabla^2(\nabla^2 w)$ and ∇^2 is the Laplacian operator.

$$\nabla^2(\cdot) = \frac{\partial^2(\cdot)}{\partial x^2} + \frac{\partial^2(\cdot)}{\partial y^2} \tag{4.7}$$

The solution of governing equation can be written as:

$$w(x, y, t) = W(x, y)e^{i\omega t} \tag{4.8}$$

Substituting the above Eq. (4.8) into Eq. (4.5) yields

$$(\nabla^4 - k^2)W = 0 \tag{4.9}$$

$$k^2 = \frac{\rho h \omega^2}{D} \tag{4.10}$$

Eq. (4.9) can be rewritten as

$$(\nabla^2 - k^2)\ (\nabla^2 + k^2)W = 0 \tag{4.11}$$

Instead of solving Eq. (4.11) directly, the solution can be calculated in the form of two linear differential equations

$$(\nabla^2 - k^2)W_1 = 0 \tag{4.12}$$

$$(\nabla^2 + k^2)W_2 = 0 \tag{4.13}$$

Therefore, the complete solution of (4.11) is

$$W = W_1 + W_2 \tag{4.14}$$

To solve Eq. (4.9), the boundary conditions of the thin plate need to be defined. The boundary conditions can be classified into two kinds: essential and natural. The essential

boundary conditions are defined explicitly by deflection *w* and its slope with respect to normal direction $\partial w/\partial n$. While the natural boundary conditions are in weak forms and defined by the normal bending moment M and the effective shear force *V*.

$$M = -D\left(\frac{\partial^2 w}{\partial n^2} + \vartheta \frac{\partial^2 w}{\partial s^2}\right) \tag{4.15}$$

$$V = -D\left(\frac{\partial^3 w}{\partial n^3} + (2 - \vartheta)\frac{\partial^3 w}{\partial n \partial s^2}\right) \tag{4.16}$$

where *s* is the tangential direction of the thin plate edge.

The rectangular plate are simply supported on all edges and the origin of the coordinates is placed at the left bottom corner as shown in Fig.

The boundary conditions for a simply supported plate are listed as below:

$$w = 0|_{x=0,a};\ \frac{\partial^2 w}{\partial x^2} = 0\Big|_{x=0,a} \tag{4.17}$$

$$w = 0|_{y=0,b};\ \frac{\partial^2 w}{\partial y^2} = 0\Big|_{y=0,b} \tag{4.18}$$

In order to satisfy all the boundary conditions, it is convenient to assume the deflections in the form as below:

$$w(x,y) = \sum_{m=1}^{\infty}\sum_{n=1}^{\infty} w_{mn}\, sin\frac{m\pi x}{a} sin\frac{n\pi y}{b} \tag{4.19}$$

where w_{mn} is the unknown coefficient need to be determined.

Correspondingly, the transversal velocity of the plate is give by

$$V(x,y) = -i\omega w(x,y) \tag{4.20}$$

The acoustic pressures radiated by the thin plate can be calculated by Rayleigh integral [72, 77, 80, 81]

$$P(x',y',z') = -i\omega\rho_0 \int_0^a \int_0^b V(x,y,z)\frac{e^{ikR}}{2\pi R}dxdy \tag{4.21}$$

where $\rho_0$is density of media, point(x', y', z') is on the hologram surface, and point *(x, y)*is the thin plate surface.

$$R = \sqrt{(x - x')^2 + (y - y')^2 + (z - z')^2} \tag{4.22}$$

where *R* is the distance between a point on the hologram surface and a point on plate surface. Then, this modified HELS based NAH is employed to reconstruction the sound field radiated from the plate.

Case 1: assuming that only the mode (2, 2) of the plate is excited, the sound pressure and particle velocity field radiated from the plate are reconstructed based on the normal surface velocity of the plate.

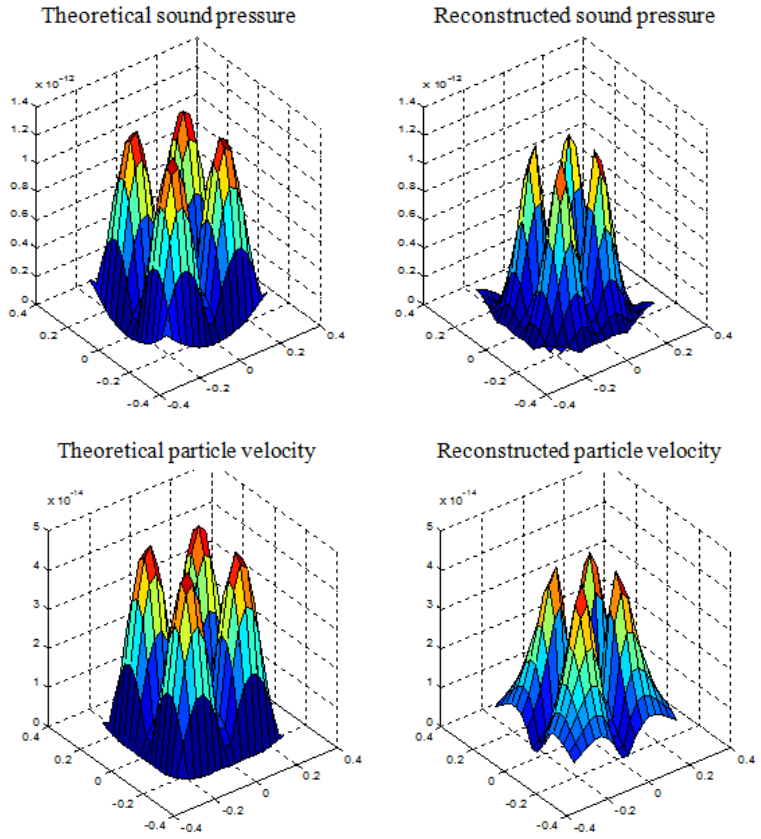

Figure 4.26 Analysis of reconstructed sound field from of a plate excited at mode (2, 2)

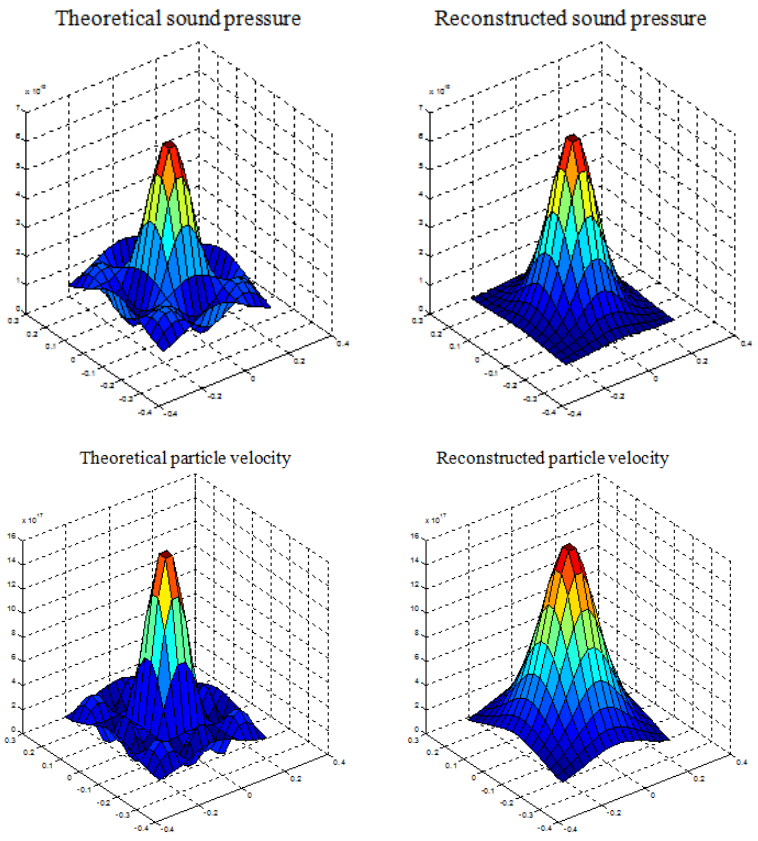

Figure 4.27 Analysis of reconstructed sound field from of a plate excited the first 10 modes

From the results of the simulation study of a plate vibration problem, it shows that HELS based NAH with laser reconstructs sound field accurately for a sound source with highly non-spherical geometry.

4.4 The impact of distance to sound field reconstruction

The distance from reconstruction surface to source surface is considered as a possible impact factor for the accuracy of sound filed reconstruction. Then, simulation study is designed to check the effects of different reconstruction distances.

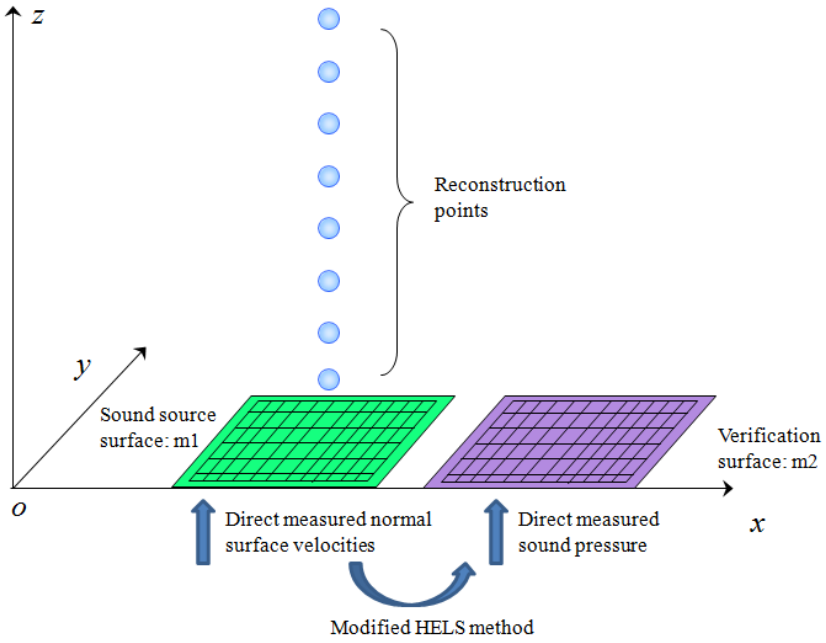

Figure 4.28 Impact of reconstruction distance to reconstruction accuracy

As illustrated on the above figure, a series of reconstruction points are selected with different distances to sound source surface. While, the verification surface is on the same plane as sound source surface.

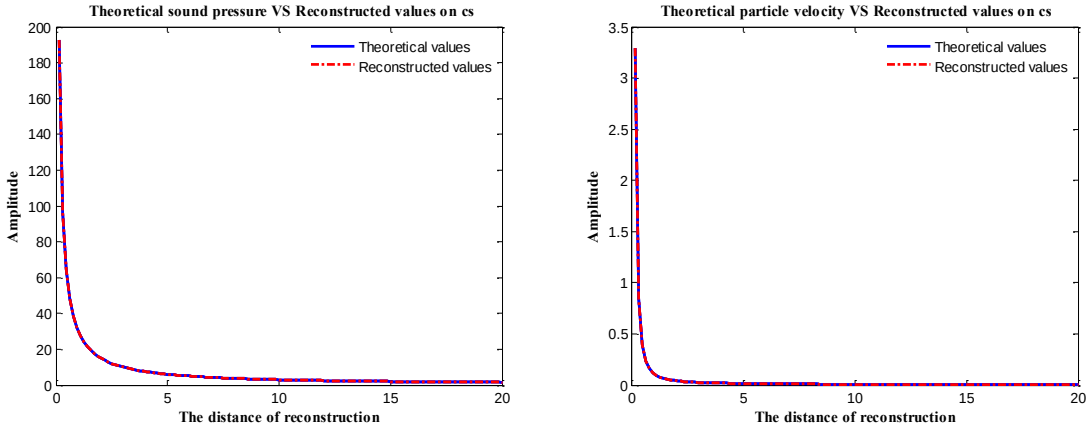

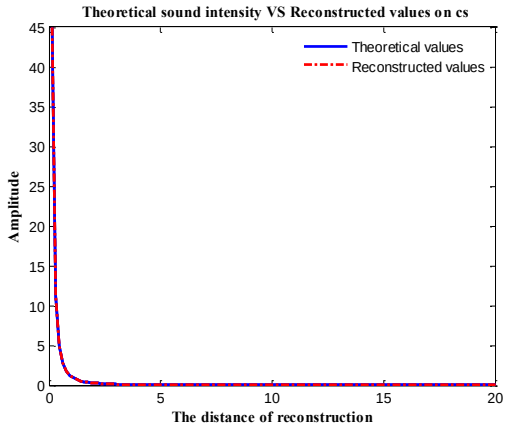

Figure 4.29 Analysis of reconstructed sound field with respect to distance for a monopole

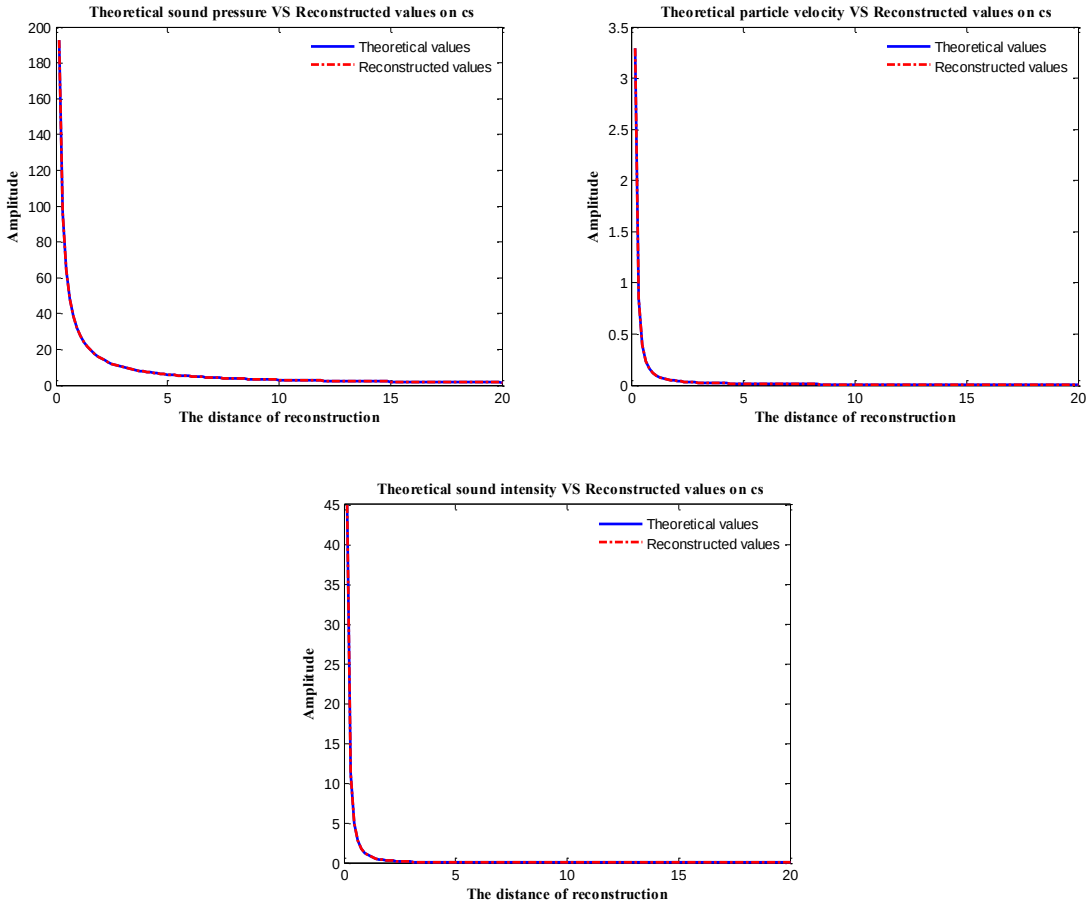

Figure 4.30 Analysis of reconstructed sound field from with respect to distance for a dipole

The results from figure 4.29 and 4.30 demonstrate that this modified HELS method is capable of obtaining high accurate reconstruction in both close and distant positions.

4.5 The optimal expansion term

Modified HELS based NAH uses the least square method to minimize the residuals, thus the optimal number of expansion term for sound pressure and particle velocity are decided by the following equations:

$$\min_{J} \sum_{i=1}^{M} \|\hat{p}(\vec{x}_m^{rec}; w) - \hat{p}(\vec{x}_m^{meas}; w)\|_2^2$$

$$\min_{J} \sum_{i=1}^{M} \|\hat{v}(\vec{x}_m^{rec}; w) - \hat{v}(\vec{x}_m^{meas}; w)\|_2^2$$

where$\hat{p}(\vec{x}_m^{rec}; w)$ and $\hat{v}(\vec{x}_m^{rec}; w)$are the reconstructed acoustic pressure and particle velocity at the m^{th} benchmark position $\vec{x}_m$, and $\hat{p}(\vec{x}_m^{meas}; w)$ and $\hat{v}(\vec{x}_m^{meas}; w)$are the measured values at the same position.

Theoretically, when the sound source is a monopole or dipole, HELS based NAH with laser only need a few expansion terms to achieve highly accurate reconstruction.

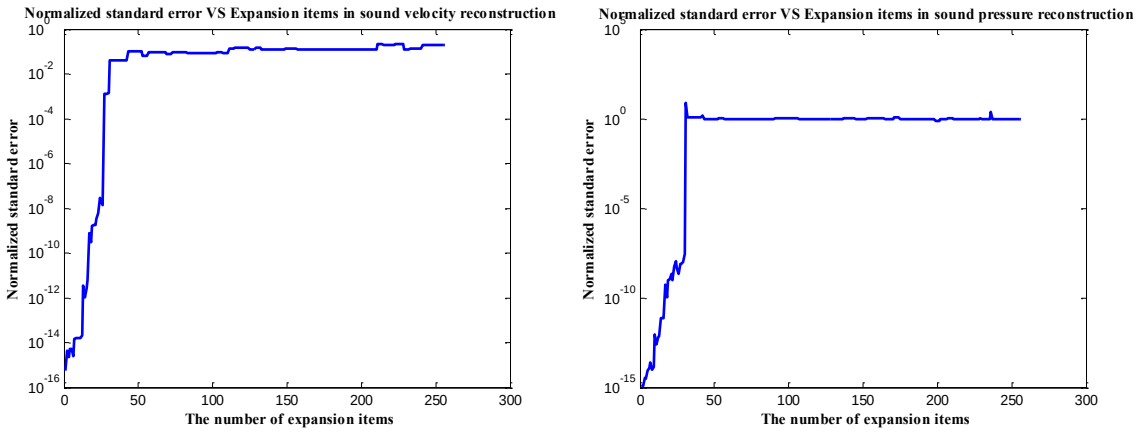

Figure 4.31 Analysis of reconstructed sound field with respect to number of expansion terms for a

monopole

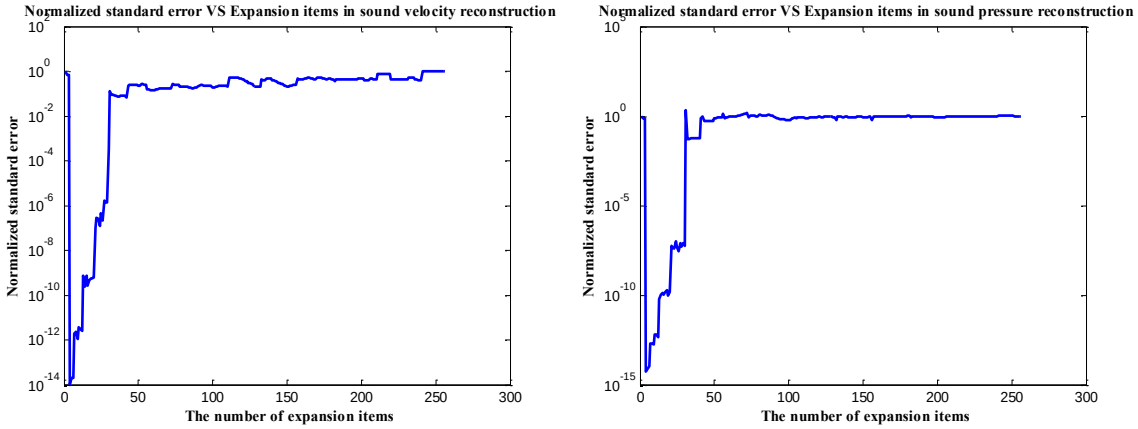

Figure 4.32 Analysis of reconstructed sound field with respect to number of expansion terms for a dipole

From figure 4.31 and figure 4.32, both the left side figures show the optimal expansion terms for sound pressure reconstruction, while the right side figures represent the optimal expansion for particle velocity reconstruction. The results testify that the HELS based NAH with laser is capable of reconstruct sound field from ideal source with only lower-order expansion terms. On the other hand, too many high order expansion terms will introduce significant errors into the reconstruction results. The study of optimal expansion term demonstrates that HELS based NAH with laser is able to minimize the reconstruction errors automatically and then obtain highly accurate reconstruction results.

CHAPTER 5

REGULARIZATIONS

Acoustic problems can be classified into two kinds: forward acoustic problem and inverse acoustic problem. As for sound field reconstruction problem, both backward problem and forward problem are involved in the process. From measured values, the information of sound source is decided. This process is a backward problem. While it turns out to be a forward problem when the information of sound source is used to reconstruct sound field quantities in other interested positions.

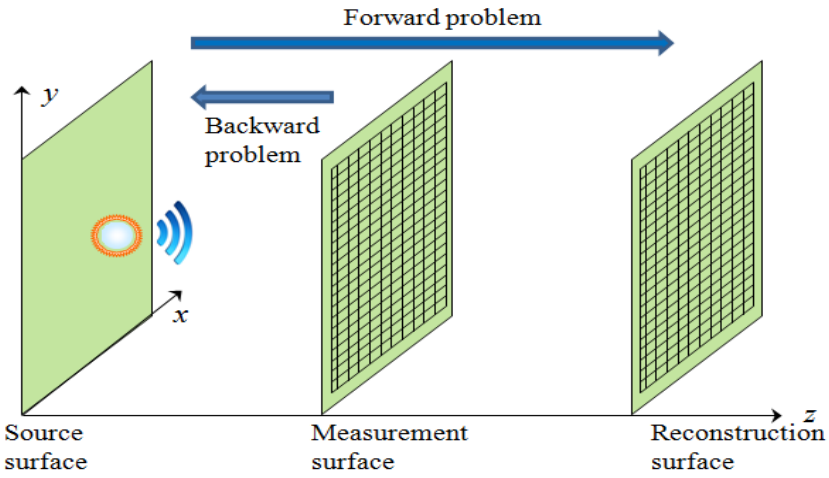

Figure 5.1 Backward progress and forward progress in HELS based NAH

5.1 Ill-posedness of the problem

Sound field reconstruction by NAH is a typical inverse problem [34, 82, 83]. According to Jacques Hadamard who gave the definition of well-posed problem in the beginning of the 1900's, a problem should satisfy the following three requirements to be qualified as a well-posed one [84-86].

1. Existence: There is a solution to the problem.

2. Uniqueness: There is only one solution to the problem.

3. Stability: The solution depends continuously on the problem data.

A well-posed problem that means there is a great chance to have a stable solution for this problem. On the contrary, if any problem fails to meet the above three criteria, it is classified into an ill-posed problem. Frequently, the basis function of HELS based NAH with laser is either noninvertible, or the inverse matrix has a very large condition number. Then, acoustic field reconstruction using HELS based NAH with laser is a discrete ill-posed problem. For an ill-posed problem, small perturbations in the input can lead to large errors of the solution. Therefore, regularization techniques are applied to HELS based NAH with laser to attain meaningful reconstructions.

For any matrix $A \in R^{m\times n}$, the singular value decomposition of A takes the following form [87-89]:

$$A = U\Sigma V^T = \sum_{i=1}^{n} u_i \sigma_i v_i^T \tag{5.1}$$

where $U = [u_1, \dots, u_n]$ and $V = [v_1, \dots, v_n]$ are orthogonal matrices whose columns are the singular vector of matrix A, diagonal matrix $\Sigma = diag(\sigma_1, \dots, \sigma_n)$. $\sigma_1, \dots, \sigma_n$ are the singular values of matrix and they satisfy a non-increasing order as follows:

$$\sigma_1 \geq \sigma_2 \geq \cdots \geq \sigma_n \geq 0 \tag{5.2}$$

The condition number of a matrix is the ratio between the largest singular value σ_1 and the smallest nonzero singular value σ_n:

$$Cond(A) = \frac{\sigma_1}{\sigma_n} \tag{5.3}$$

The condition number demonstrates the sensitivity of the output with respect to the perturbation of input in a function. When the condition number is large, it means that the ill-condition of the problem is severe.

According to theoretical background in chapter 3, the particle velocity can be calculated as:

$$[T_v(\vec{x}_m|\vec{x}_v)]_{M\times N}\{\hat{v}_v(\vec{x}_v;w)\}_{N\times 1} = \{\hat{v}_v(\vec{x}_m;w)\}_{M\times 1} \tag{5.4}$$

where $[T_v(\vec{x}_m|\vec{x}_v)]_{M\times N}$ is the transfer function that correlates measured normal surface velocity to particle velocity, which is given by

$$[T_v(\vec{x}_m|\vec{x}_v)]_{M\times N} = \left[\frac{\partial\Psi(\vec{x}_m;w)}{\partial n}\right]_{M\times J}\left[\frac{\partial\Psi(\vec{x}_v;w)}{\partial n}\right]^{\dagger}_{J\times N} \tag{5.5}$$

Similarly, the main formulation of this invention to reconstruct the radiated acoustic pressure in three-dimension space from any vibrating structure.

$$[G_v(\vec{x}_m|\vec{x}_v)]_{M\times N}\{\hat{p}_v(\vec{x}_v;w)\}_{N\times 1} = \{\hat{v}_v(\vec{x}_m;w)\}_{M\times 1} \tag{5.6}$$

where $[G_v(\vec{x}_v|\vec{x}_m)]_{N\times M}$stands for the transfer function that correlates the normal surface velocity to the field acoustic pressure, which is given by

$$[G_v(\vec{x}_m|\vec{x}_v)]_{M\times N} = \frac{1}{iw\rho_0}\left[\frac{\partial\Psi(\vec{x}_m;w)}{\partial n}\right]_{M\times J}[\Psi(\vec{x}_n;w)]^{\dagger}_{J\times N} \tag{5.7}$$

In this comparison study of regularization methods, a size of 8×8 reconstructed surface is used. Then, both N and M have a value of 64 and the size of transfer function T_v is 64×64.

Singular value decompositions are conducted on the transfer functions:

$$[T_v(\vec{x}_m|\vec{x}_v)]_{64\times 64} = (U\Sigma V^T)_{T_v} = (\textstyle\sum_{i=1}^{n} u_i\sigma_i v_i^T)_{T_v} \tag{5.8}$$

$$[G_v(\vec{x}_m|\vec{x}_v)]_{64\times 64} = (U\Sigma V^T)_{G_v} = (\textstyle\sum_{i=1}^{n} u_i\sigma_i v_i^T)_{G_v} \tag{5.9}$$

The condition number and graphs of singular values with respect to their index can be obtained.

$$Cond([T_v(\vec{x}_m|\vec{x}_v)]_{64\times64}) = \left(\frac{\sigma_1}{\sigma_{64}}\right)_{T_v} = 7.2204e+16 \tag{5.10}$$

$$Cond([G_v(\vec{x}_m|\vec{x}_v)]_{64\times64}) = \left(\frac{\sigma_1}{\sigma_{64}}\right)_{G_v} = 5.8939e+16 \tag{5.11}$$

The condition numbers of both transfer functions are very large, and they indicate that the outputs of sound field reconstruction are easily disturbed by errors and perturbations. Sound field reconstruction process is severely ill-posed.

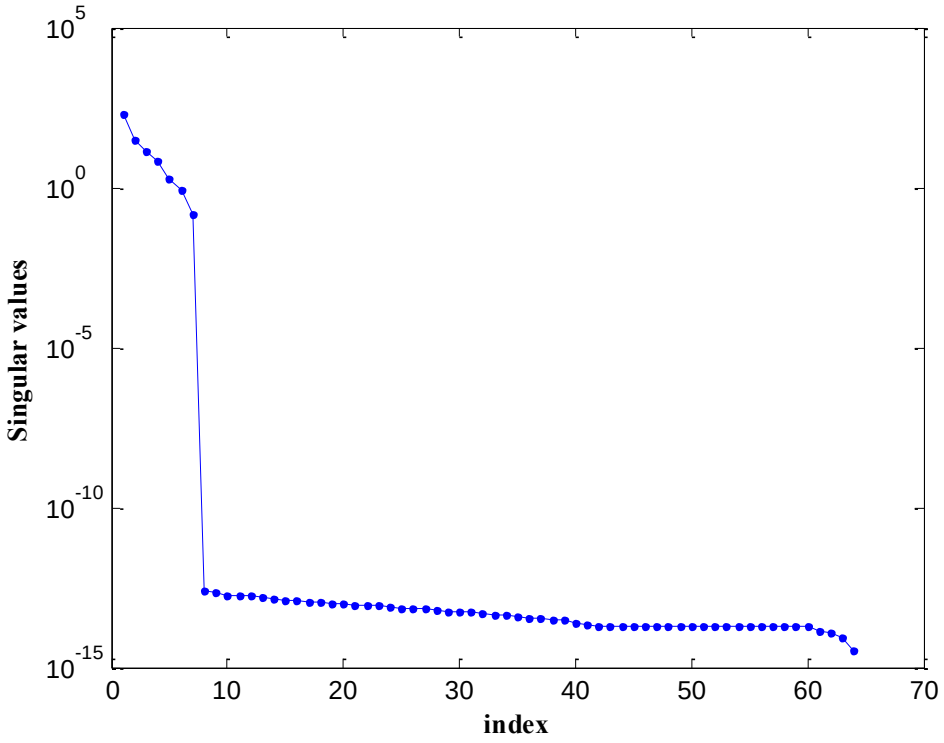

Figure 5.2 Singular values of $[T_v(\vec{x}_m|\vec{x}_v)]_{64\times64}$

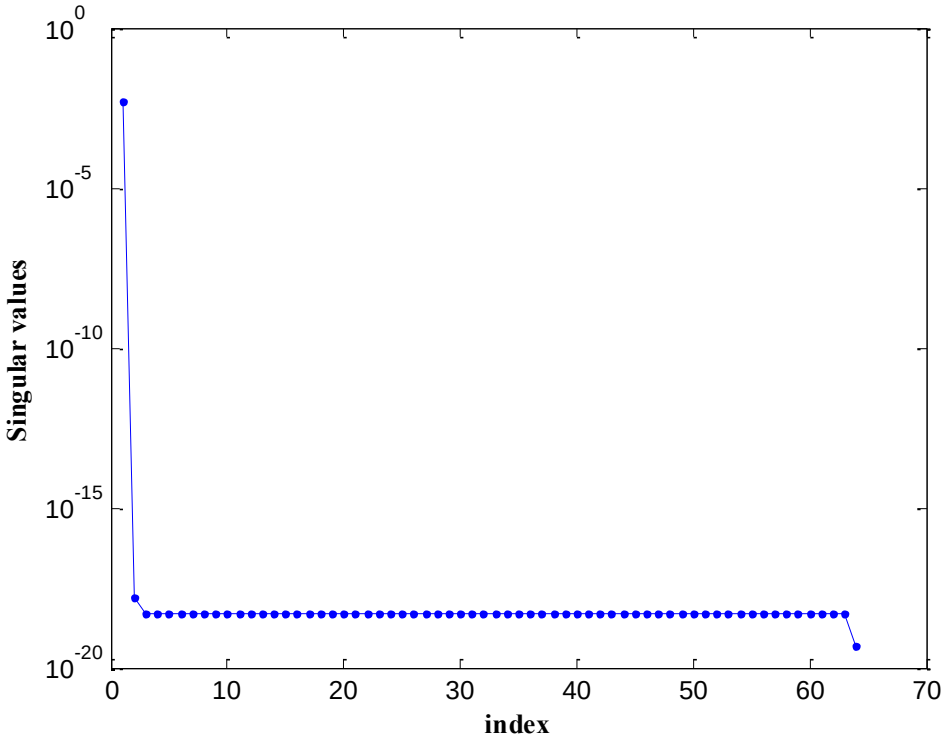

Figure 5.3 Singular values of $[G_v(\vec{x}_m|\vec{x}_v)]_{64\times64}$

The singular values of transfer functions decay constantly to zero. Another important feature of ill-posed problems needs to be introduced is Picard condition. According to Per Christian Hansen [90, 91], the discrete Picard condition is that the Fourier coefficients $|u_i^T \hat{v}_v|$ decay to zero faster than the generalized singular values. The Picard condition needs to be satisfied in order to get good regularized solutions.

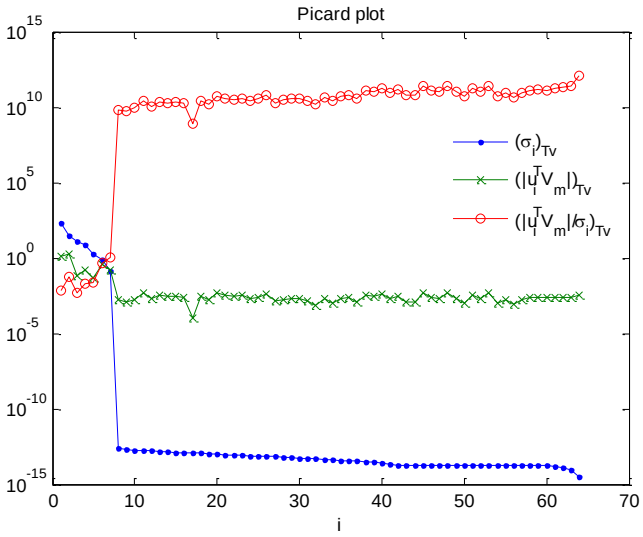

Figure 5.4 Picard plot of $[T_v(\vec{x}_m|\vec{x}_v)]_{64\times64}$

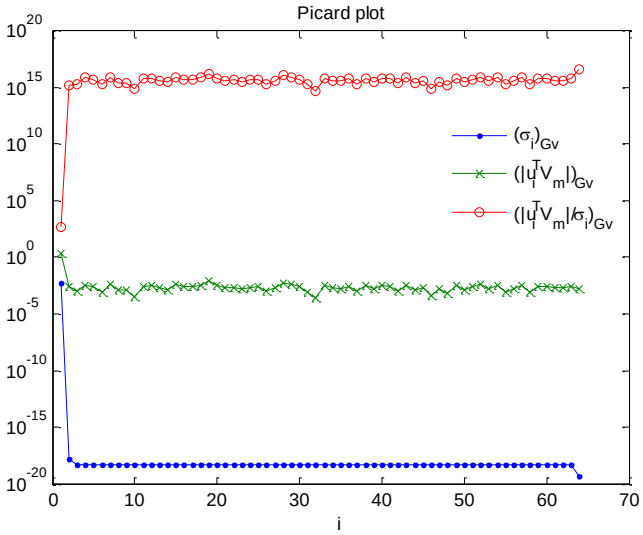

Figure 5.5 Picard plot of $[G_v(\vec{x}_m|\vec{x}_v)]_{64\times64}$

From figure 5.4 and 5.5, the transfer functions in HELS based NAH with laser are failed to meet the Picard condition. Vectors $\left|u_i^T \hat{v}_v\right|$ decrease to a level around 0.001, then just stay around that level. On the contrary, the singular values of both transfer functions decrease straight to a very low level. These features of transfer functions demonstrate the ill-condition of the problem.

Regularization methods are introduced to reformulate transfer functions to stabilize the solution and obtain a meaningful approximation. In this section, multiple regularization methods will be tested with HELS based NAH with laser to produce the most precise sound field reconstruction. The comparison and time-cost analysis will be conducted to single out the most proper regularization technique for HELS based NAH with laser. All the computations are based on reconstructing the sound field generated by a monopole source.

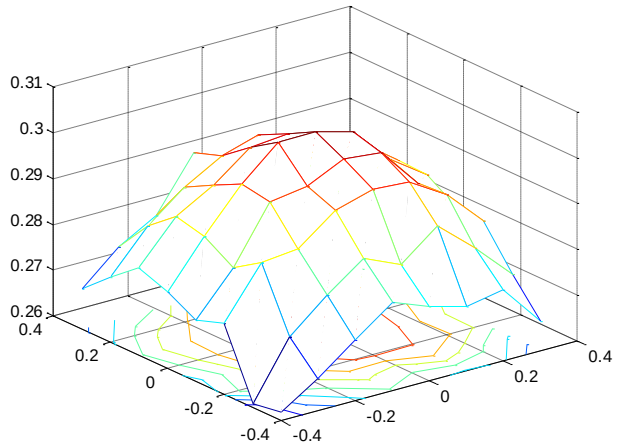

Figure 5.6 Polluted particle velocity array

All regularization techniques are tested using the same polluted particle velocity as showed in figure 5.6. The formula of errors between theoretical sound pressure and reconstructed values is listed as follows:

$$Error(P) = \frac{norm((P_t - P_r),1)}{norm((P_t),1)} \tag{5.12}$$

where P_t is the theoretical sound pressure, and P_r is the reconstructed sound pressure.

Similarly, the error between ideal particle velocity and reconstructed values is:

$$Error(V) = \frac{norm((V_t - V_r),1)}{norm((V_t),1)} \tag{5.13}$$

where V_t is the ideal sound particle velocity, and V_r is the reconstructed sound particle velocity.

5.2 Regularization techniques

5.2.1 Truncated singular value decomposition method [92-94]

The small singular values is believed to represent the noise, and then the truncated transfer function represents a filtered system and is able to deliver more precise results. Truncated singular value decomposition (TSVD) fulfills this goal by setting the small singular values to zeros. Therefore, closest approximate matrices instead of ill-conditioned transfer functions will be used in the process of sound field reconstruction. Assuming that rank *k* is the best approximation for both transfer functions, then we have:

$$[G_v(\vec{x}_m|\vec{x}_v)]_{64\times 64} = (U\Sigma_k V^T)_{G_v} = \left(\sum_{i=1}^{k} u_i \sigma_i v_i^T\right)_{G_v} \tag{5.14}$$

The diagonal matrices for both transfer functions have the same form: $\Sigma_k = diag[\sigma_1, \sigma_2, \dots, \sigma_k, 0, \dots, 0]$. Then, the inversion matrices can be calculated as follows:

$$[G_v(\vec{x}_m|\vec{x}_v)]^{\dagger} = \left(V\Sigma_k^{\dagger}U^T\right)_{G_v} = \left(\sum_{i=1}^{k} v_i \sigma_i^{-1} u_i^T\right)_{G_v} \tag{5.15}$$

Then, the particle velocity distributions can be calculated by TSVD method as follows:

$$\hat{v}_v(\vec{x}_v; w) = [G_v(\vec{x}_m|\vec{x}_v)]^{\dagger}\hat{v}_v(\vec{x}_m; w) = \left(\sum_{i=1}^{k} v_i \sigma_i^{-1} u_i^T\right)_{G_v} \hat{v}_v(\vec{x}_m; w) \tag{5.16}$$

Similarly, the pressure reconstruction has been derived as follows:

$$\hat{p}_v(\vec{x}_v; w) = [T_v(\vec{x}_m|\vec{x}_v)]^{\dagger}\hat{v}_v(\vec{x}_m; w) = \left(\sum_{i=1}^{k} v_i \sigma_i^{-1} u_i^T\right)_{T_v} \hat{v}_v(\vec{x}_m; w) \tag{5.17}$$

There is a challenge about choosing a proper truncation parameter *k*. When a higher rank *k* is chosen. Theoretically, a closer approximation to true solution will be obtained. However, when rank *k* is too large, large proportional measurement errors associated with large indices of transfer function will be added. On the other hand, when rank *k* is chosen at a too small value, most of details of the sound filed will be lost.

The following figure 5.7 shows the results by combining HELS based NAH with laser with TSVD method, and the reconstructed sound field quantities are compared with theoretical values.

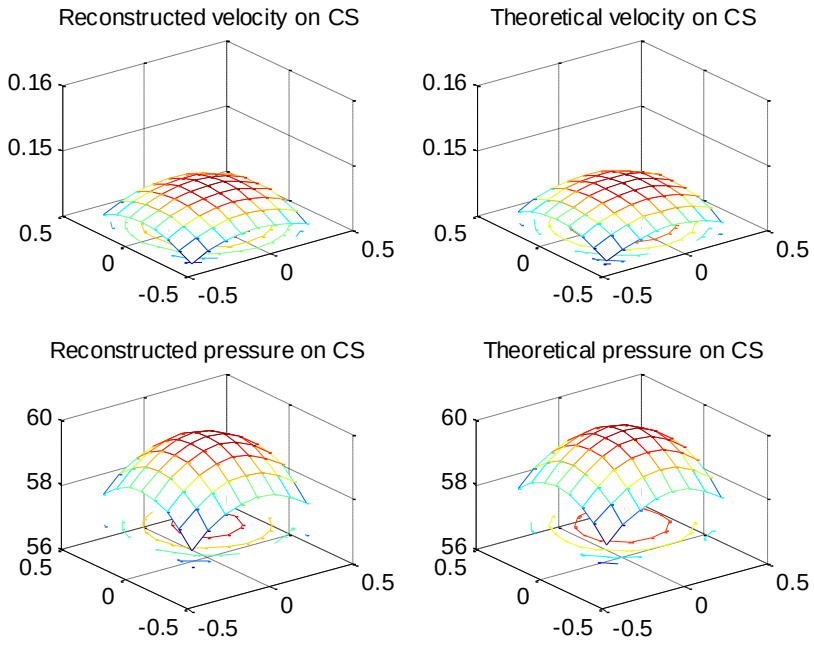

Figure 5.7 Reconstructed acoustic pressure and particle velocity by TSVD

5.2.2 Tikhonov regularization [95, 96]

For an ill-posed problem $Ax=b$, the linear least-squares minimization method seeks to an approximate solution by directly minimizing the sum of squared residuals:

$$min_{x\in R^n}\|Ax-b\|^2 \tag{5.18}$$

where $\|\cdot\|$ is the Euclidean norm. Tikhonov regularization method is one of the most popular regularization techniques used in discrete inverse problems. When the solution is known smooth in advance, a penalized factor is introduced into the problem by Tikhonov regularization method.

$$min_{x\in R^n}\{\|Ax-b\|^2+\mu^2\|Lx\|^2\} \tag{5.19}$$

where $\mu^2$is the regularization parameter, and L is referred to as the regularization operator. The simplest case is to use identity matrix as regularization operator, then the minimization problem has been changed into:

$$min_{x\in R^n}\{\|Ax-b\|^2+\mu^2\|x\|^2\} \tag{5.20}$$

The problem can be reformulated as a linear least squares problem:

$$\min_{x\in R^n}\left\|\begin{pmatrix}A\\ \mu I\end{pmatrix}x-\begin{pmatrix}b\\ 0\end{pmatrix}\right\|^2 \tag{5.21}$$

The equivalent linear system of equations of the above minimization problem can be set as:

$$x=(A^TA+\mu^2I)^{-1}A^Tb \tag{5.22}$$

Correspondingly, the condition number of matrix A is reduced from $\frac{\sigma_1}{\sigma_n}$ to $\frac{\sqrt{\sigma_1^2+\mu^2}}{\sqrt{\sigma_n^2+\mu^2}}$, then the ill-condition of matrix A is improved. When the SVD of A exists ($A=U\Sigma V^T$), the solution x is modified to:

$$x=V(\Sigma^2+\mu^2I)^{-1}\Sigma U^Tb=\sum_{i=1}^{n}v_i\frac{\sigma_i}{{\sigma_i}^2+\mu^2}u_i^Tb \tag{5.23}$$

The following figure 5.8 shows the results by combining HELS based NAH with laser with Tikhonov regularization method, and the reconstructed sound field quantities are compared with theoretical values.

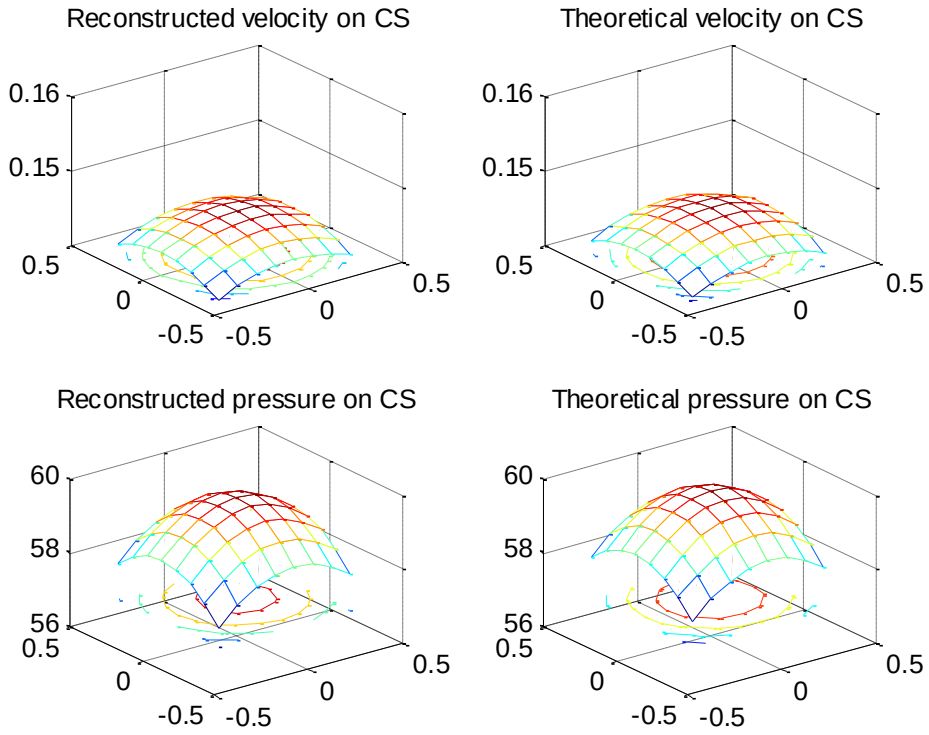

Figure 5.8 Reconstructed acoustic pressure and particle velocity array by Tikhonov regularization

5.2.3 Hybrid regularization method [53, 54, 82]

A hybrid regularization technique is developed to obtain highly accurate sound pressure and normal surface velocity reconstruction from HELS based NAH with laser. Using singular value decompositions of the transfer functions, the optimization target for particle velocity reconstruction is set as follows:

$$\left\|(U\Sigma V^H)_{T_v}\hat{v}_v^{rec}(\vec{x}_v;w)-\hat{v}_v^{meas.}(\vec{x}_m;w)\right\|+\alpha\|F_h^{\alpha}V^H\hat{v}_v^{rec}(\vec{x}_v;w)\| \tag{5.24}$$

The generalized cross validation method is used to determine the regularization parameter α:

$$\min_{\alpha}\left(\frac{\left\|F_h^{\alpha}U^H\hat{v}_v^{meas.}(\vec{x}_m;w)\right\|^2}{[Trace(F_h^{\alpha})]^2}\right) \tag{5.25}$$

The high-pass filter F_h^α is defined as:

$$F_h^\alpha = diag(I - F^\alpha) \tag{5.26}$$

where I is an identity matrix with the same size of transfer function T_v. F^α is a low-pass filter and it is defined as below:

$$F^\alpha = diag(\dots, \frac{\sigma_i^2 \cdot (\alpha + \sigma_i^2)^2}{\alpha^3 + \sigma_i^2 \cdot (\alpha + \sigma_i^2)^2}, \dots) \tag{5.27}$$

When the pass filters are decided, the regularized particle velocity can be obtained as:

$$\hat{v}_v^{rec}(\vec{x}_v; w) = (VF^\alpha \Sigma^{-1} U^H)_{T_v} \cdot \hat{v}_v^{meas.}(\vec{x}_m; w) \tag{5.28}$$

Following the same procedures, the regularized acoustic pressure can be decided as:

$$\hat{P}_v^{rec}(\vec{x}_v; w) = (VF^\alpha \Sigma^{-1} U^H)_{G_v} \cdot \hat{v}_v^{meas.}(\vec{x}_m; w) \tag{5.29}$$

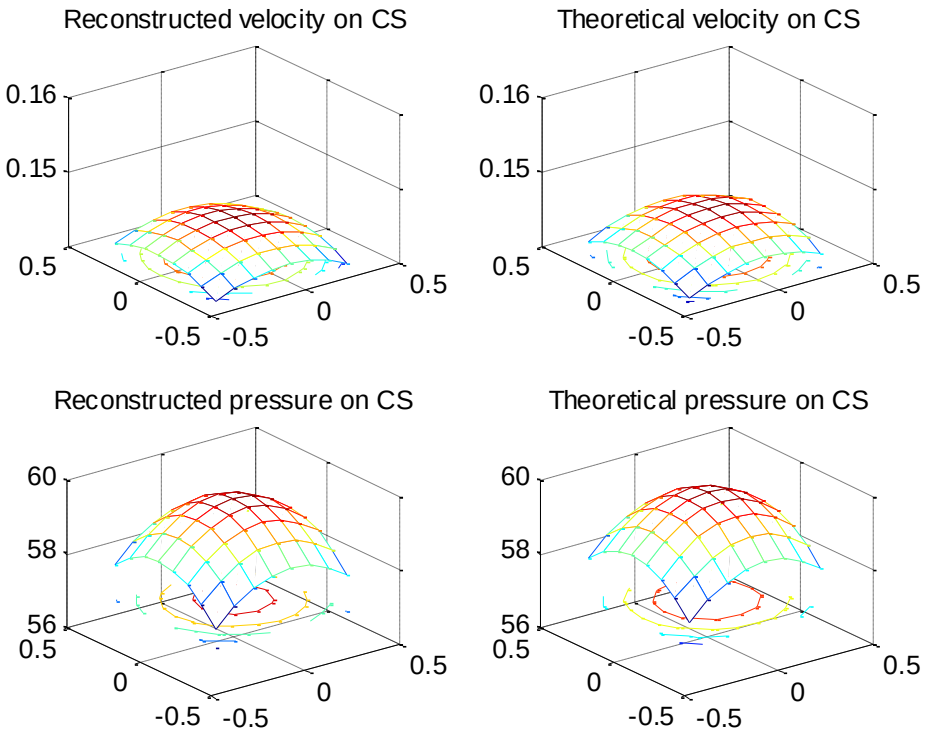

Figure 5.9 Reconstructed acoustic pressure and particle velocity array by hybrid regularization method

The figure 5.9 shows the results by combining HELS based NAH with laser with hybrid regularization method, and the reconstructed sound field quantities are compared with theatrical values.

5.2.4 Multilevel method [97, 98]

Multilevel method is developed from multigrid method and it turns out to be an effective tool for ill-posed problems. The paramount steps for multigrid method are smoothing, restriction and interpolation or prolongation. Similarly, the multilevel method follows these steps. Firstly, an approximate solution is composed based on the fine-scale system and the high frequency errors can be reduced. Secondly, the residual of solution is obtained and then the residual errors are down sampled from fine to a coarser grid. Following the procedure, the approximate solution is decided on the coarsest level. Finally, the iterations are used to get a computed approximate solution inversely from a coarser grid to a finer grid, and then it serves as initial guess for the next level calculation.

For an ill-posed problem $Ax=b$, it can be transformed to be a smaller size problem as below:

$$A^i x^i = b^i, 0 \le i \le n \tag{5.36}$$

The operator at certain level is defined as:

$$A^{i+1} = R^i A^i P^i \tag{5.37}$$

where R- the restriction operator; P- The prolongation operator.

The flow chart of multilevel method can be listed as follow:

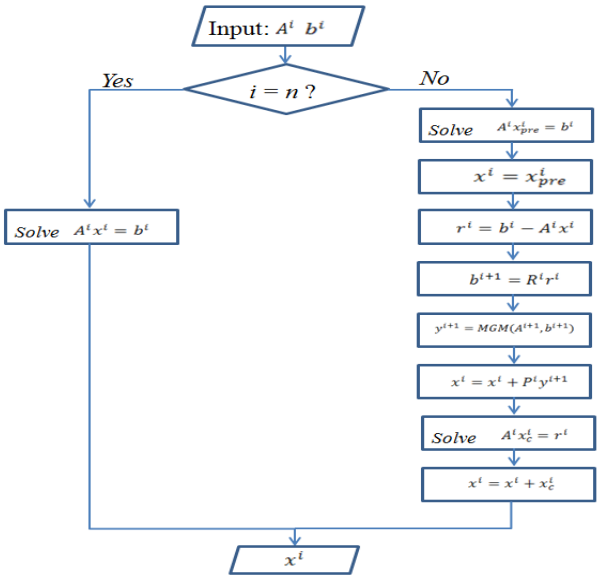

Figure 5.10 Flow chart of multilevel method [98]

The figure 5.11 shows the results by combining modified HELS method with multilevel method, and the reconstructed sound field quantities are compared with theatrical values.

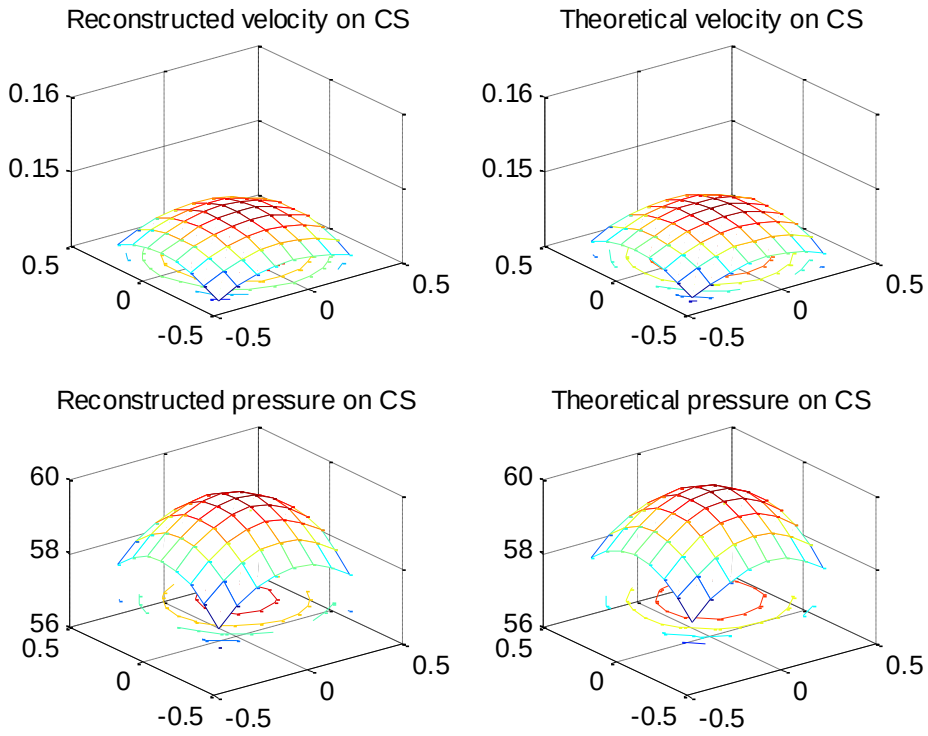

Figure 5.11 Reconstructed acoustic pressure and particle velocity array by multilevel method

Table 5.1. Comparisons of regularization techniques

Regularization technique	TSVD	Tikhonov regularization	Hybrid regularization method	Multilevel method
$Error(P)$	0.0079	0.0070	0.0038	0.0036
$Error(V)$	0.0074	0.0038	0.0035	0.0035
Time-cost (s)	193.827751	16.621714	15.961669	2541.319452

5.3 Summary

The table 5.1 is the summary of comparisons between different regularization techniques. It shows that all of methods can produce relative good reconstruction results. However, there exists big differences in time-cost. Considering that modified HELS method is used to reconstruct sound field in a large frequency range, the efficiency of regularization technique is a high priority. Therefore, the hybrid regularization method is selected as the most proper regularization technique for HELS based NAH with laser.

CHAPTER 6

EXPERIMENTAL VALIDATIONS

The HELS based NAH with laser has been verified in both theoretical derivation and numerical simulations. On the other hand, experiment verification is also indispensable to validate the theory. Experiments utilizing HELS based NAH with laser are conducted in a fully anechoic chamber at college of engineering, Wayne State University.

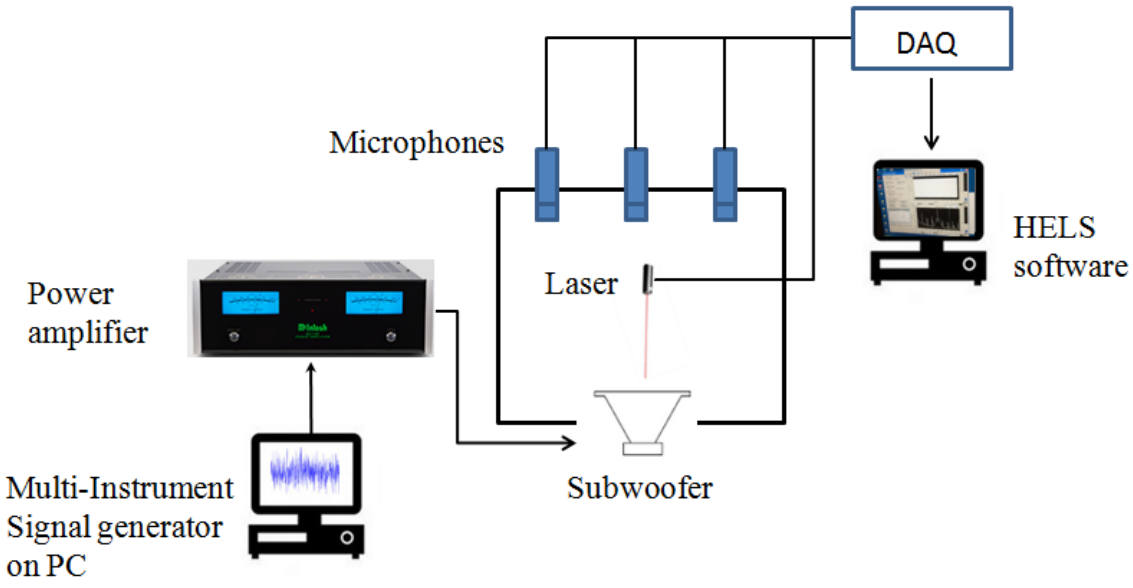

Figure 6.1 The schematic diagram of experiment

6.1 Laser Doppler vibrometer (LDV)

LDV is a highly accurate optical transducer and it is capable of measuring the normal surface velocity with high accuracy [18, 99].

In the test, the measurement points are labeled by reflective paper that is able to reflect the laser beam like a mirror. The whole measurement process can be divided into two parts.

Firstly, the laser beam emitted from the laser head shoots at those points vertically on the test target. Secondly, the wave is reflected by the moving surface and received by a photo detector in vibrometer. Optical Doppler Effect produces a frequency shift between the original emitted laser beam and the backscattered beam [16, 17].

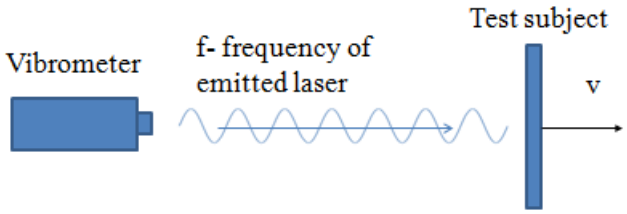

Figure 6.2 Laser travelling from vibrometer to test subject

When the test subject is moving away relative to source with velocity v, the frequency observed at the test subject due to Doppler Effect can be calculated as:

$$f' = \frac{(c-v)}{c} f \tag{6.1}$$

where c is travelling speed of laser beam; v is the velocity of test subject.

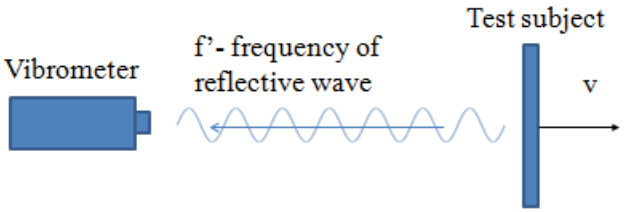

Figure 6.3 Laser travelling from test subject back to vibrometer

When the wave is reflected by test subject, the vibrometer is served as a receiver. Then the frequency observed at vibrometer position is described as:

$$f'' = \frac{c}{c+v} f' \tag{6.2}$$

Then, the relationship between the original frequency of emitted laser beam and reflective one can be defined as:

$$f'' = \frac{c}{(c+v)} f' = \frac{c}{(c+v)} \frac{(c-v)}{c} f = (1 - \frac{2v}{c}) f \tag{6.3}$$

Therefore, the total frequency shift caused by the optical Doppler Effect can be listed as follows:

$$\Delta f = f - f'' = \frac{2v}{c} f = \frac{2v}{\lambda} \tag{6.4}$$

where λ is the wavelength of the emitted laser wave.

In Eq. (6.4), the wavelength needs to be a known value and then the frequency shift can be measured by the LDV by a laser interferometer. There is a beam splitter in an interferometer, the laser beam is divided into a signal beam and a reference beam. The backscattered laser beam is compared with the reference beam, and the relative changes in frequency of laser beam can be detected by using an interferometer. Then, the velocity of target surface can be decided by Eq. (6.4).

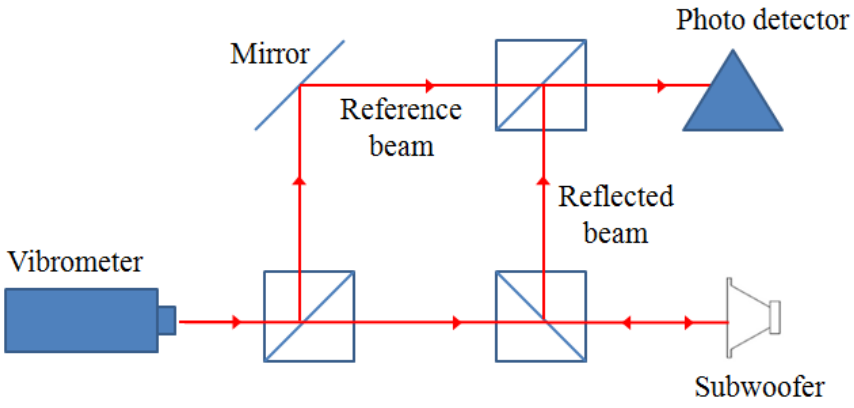

Figure 6.4 LDV operating principle

The advantages of LDV can be summed as follows [100-107]:

1. LDV is an accurate and versatile non-contact vibration measurement tool. When the test object has soft surface or very small mass, traditional measurement methods need to add accelerometers on the target which inevitably will change the natural frequency and damping ratio of the system. On the contrary, non-contact vibration measurement enables measurements without affecting the vibration characteristics of the object. Moreover, since the diameter of the laser beam is very small, it has a great advantage for LDV to measure the vibration on small structures. For those targets having complex shapes, LDV is able to do the measurements which are difficult or even impossible to access for traditional accelerometers.

2. The experimental instruments is easy to set up. When the laser head is placed vertically to the measurement surface and the laser is directed to a measurement point using optical stands or tripods, the laser beam can be focused automatically by adjusting the lens with a remote controller. The displacement or velocity of the surface can be measured with high accuracy, consistency and reliability. Also, the operation software and frontend of the measuring system is user-friendly and it enables engineers to master this tool without any difficulty.

6.2 The test procedures

The whole test setup of the experiment can be demonstrated as follows:

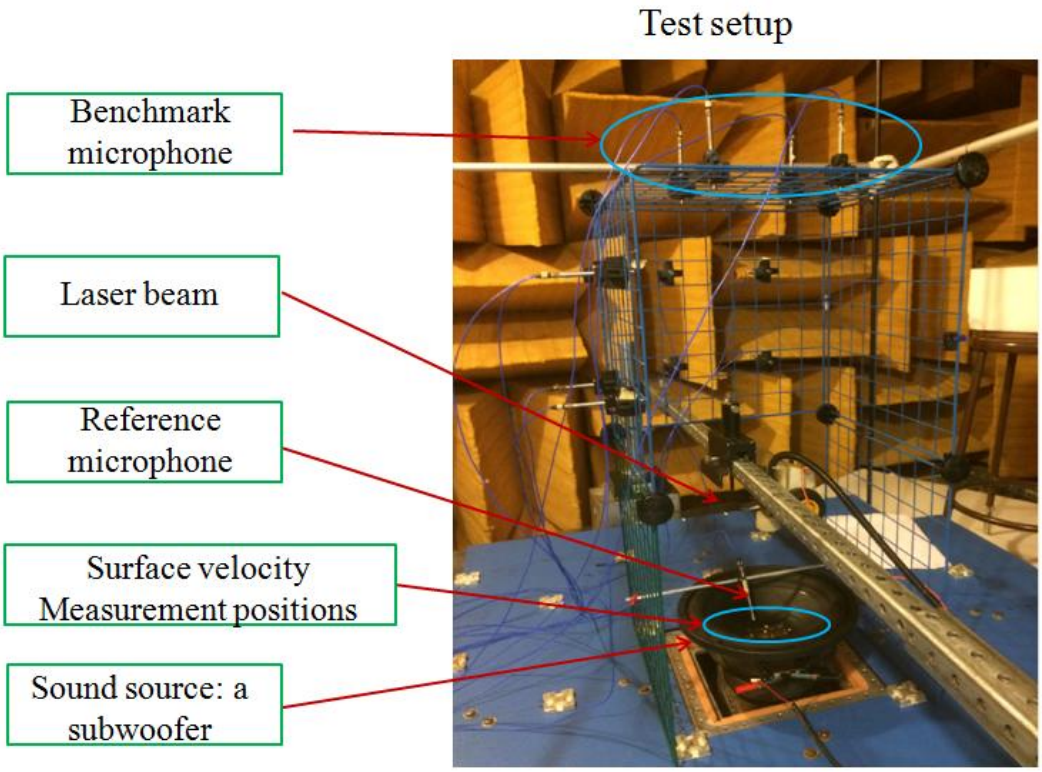

Figure 6.5 Test setup for HELS based NAH with laser

The experimental setup is placed in the anechoic chamber of Acoustics, Vibration and Noise Control laboratory. There are twelve microphones are attached on the metal framework. Four microphones are placed on the top surface, while the other eight microphone are fixed on the side surfaces. From the reconstruction results, it turns out that the results from the top four microphones are far better than other microphones. The reason for that is those top microphones are facing the sound source directly while the rest microphones have some angle toward the sound source. Therefore, only the experiment results from the top four microphones will be discussed further.

In the stage of preparation, all microphones are carefully calibrated at 250 Hz and the SPL value of sound produced by calibrator is set as 114 dB. Based on their sensitivity, all

microphones are labeled and sorted in order. The most two sensitive microphones are selected as reference microphones, and then they are used to correct the phase difference.

The Multi-Instrument is a powerful multi-function virtual instrument software and it supports a variety of signal generators. In the experiment, the noise generator is used to produce white noise signal continuously. Then, the signal is introduced into a power amplifier. A round subwoofer is chosen as the test object since it has relative flat top surface, and then measuring points can be marked on the surface easily. Moreover, the LDV is able to provide more accurate normal surface velocity measurements on objects with flat surface than test bodies with ruffled or curved surface. The subwoofer is fixed on a solid steel base. The coordinates of microphones and laser measured positions are measured by 3D digitizer.

Another important point needed to discuss for the experimental setup is the rule to decide the origin of the coordinate system. Since HELS based NAH uses the spherical wave functions to reconstruct the sound quantities on a highly non-spherical surface like the subwoofer, the errors are introduced unavoidably in the reconstruction process by this approximation. For the sound fields reconstruction of a non-spherical sound source, the accuracy will deteriorate when coordinate system is placed either too far away or too close to the source. Only when the coordinate system is arranged properly, the discrepancies between reconstructed acoustic quantities and true values could be controlled in a reasonable range.

Based on numerical simulation results and the process of trial and error, an empirical formula is put forward to select the origin of the coordinate system:

$$d_{origin} = (1.1\sim1.3)Q \tag{6.5}$$

where $Q = \sqrt{2}r$, and r is the radius of the subwoofer.

A LDV is used to measure the normal surface velocity, and it is able to provide a quick and flexible surface velocity measurement over the vibrating structure. The measured normal surface velocity is the input of this HELS based NAH with laser.

According to the manual of LDV, the optimal stand−off distances from the subwoofer surface to the laser head are set as follows:

$$Optimal\ stand-off\ distance = 135\ mm + (n * l)\ mm \qquad (6.6)$$

where n =0, 1, 2..., and $l = 204\ mm\ \pm 1\ mm$ [108].

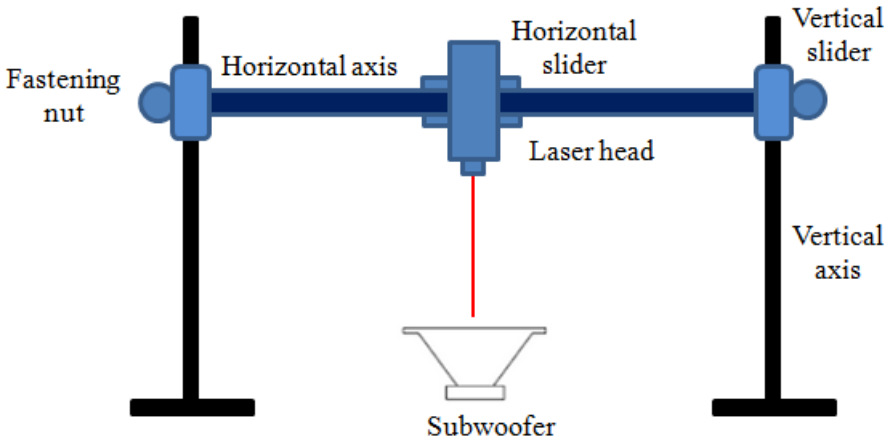

Figure 6.6 Positioning device of LDV

The positioning device of laser is illustrated as figure 6.6, the height of laser head can be adjusted by changing the position of vertical sliders along vertical axis, and the horizontal position can be changed similarly.

When the stand-off distance is in the optimal range, the signal window on Polytec fiber interferometer will demonstrate high level of signal strength. Therefore, highly accurate experimental results are achievable in this kind of ideal test condition.

6.3 Experimental results

From the LDV, the normal surface velocities are measured as follows:

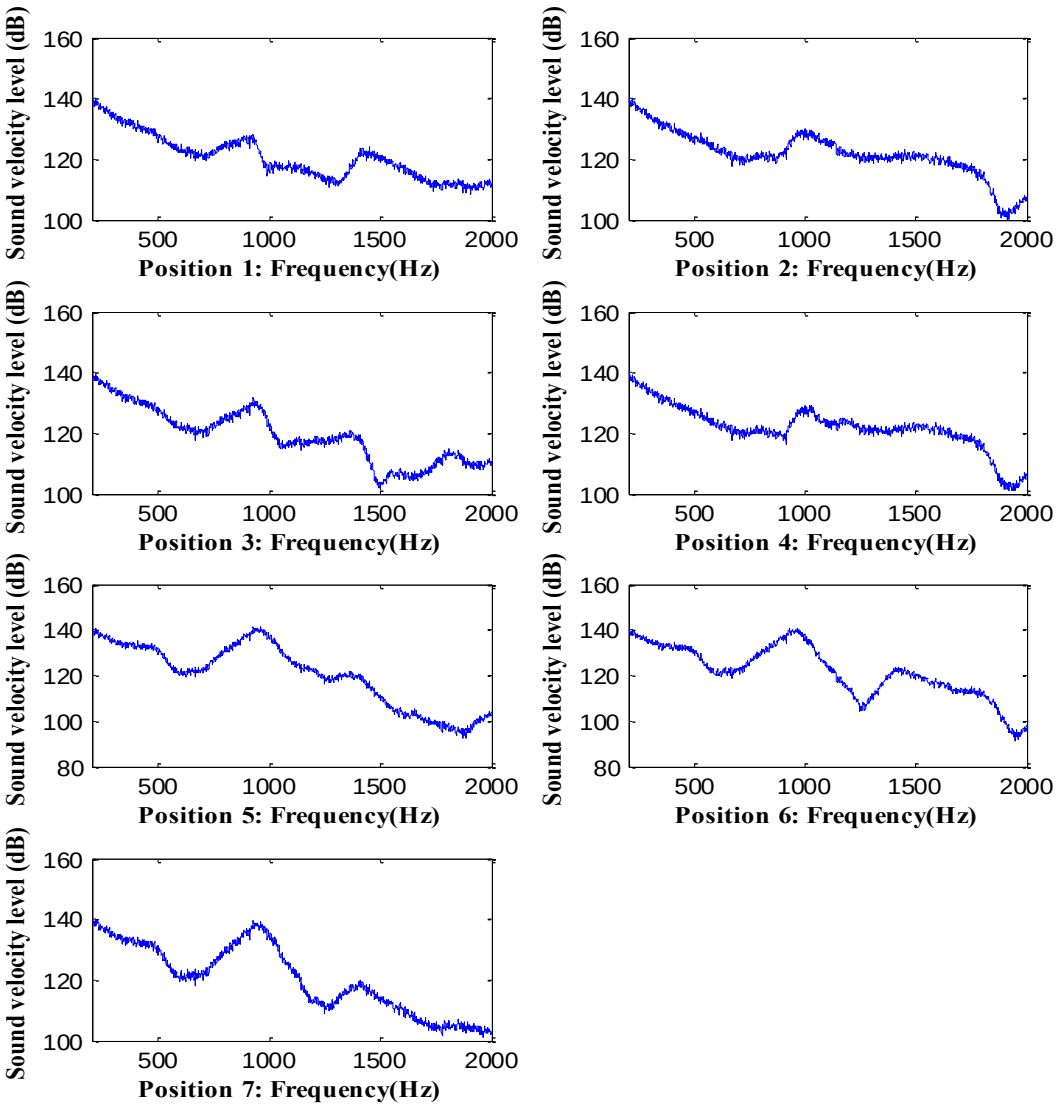

Figure 6.7 Measured normal surface sound velocity

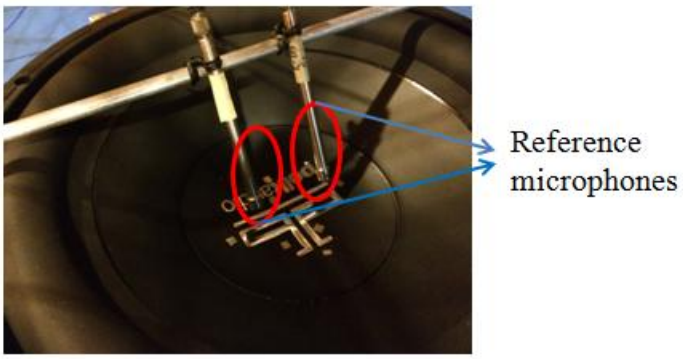

Figure 6.8 Reference microphones

The LDV in the lab only can measure the surface velocity at one single point, the position of laser head is manually moved to the next measuring point by adjusting the horizontal slider and position of vertical axis. Since the experiment is not finished in an automatic and continuous mode and each time experimenter is needed to enter the anechoic chamber and adjust the experiment setup, the variations in environmental conditions such as temperature and humidity have been changed inevitably. Meanwhile, the seven points of surface velocities are measured at different time. Therefore, there exist phase differences between different measurements. A phase transfer function is introduced between different measurements using the same reference microphone to alleviate the phase discrepancy.

$$|\hat{v}|_{f,m} = \frac{|\hat{v}|_{f,m}}{|\hat{p}|_{r,m}} |\hat{p}|_{r,n} \tag{6.7}$$

where $|\hat{v}|_{f,m}$ is the amplitude of surface velocity at measurement m and m=1,2, ..., 7;

$|\hat{p}|_{r,m}$ is the amplitude of sound pressure of reference microphone at measurement m;

$|\hat{p}|_{r,n}$ is the amplitude of sound pressure of reference microphone at measurement n, and n is the picked measurement serving as reference for all other measurements.

Ideally, in order to eliminate the phase discrepancy of different surface velocity measurements, the optimal reference should use a surface velocity signal measured at a fixed position. However, sound pressure measured by reference microphone is used instead in the setup of experimental validation of modified HELS method based on laser. Therefore, the phase error, though alleviate in a large degree, is still existing unavoidably. The problem is caused by the limitations of hardware, and only one single point of surface velocity can be measured each time. A quickly scanning LDV or a LDV that can measure surface velocity in multiply positions at the same time is a perfect solution for this problem.

In the experiment verification of modified HELS method based on laser, the benchmark surface m2 and reconstruction surface on the same plane. However, the nodes on m2 used for finding optimal expansion items and the nodes on reconstruction surface have different coordinate values.The measured surface velocities are used as input in HELS based NAH with laser to reconstruct sound pressure at 4 different positions to decide the optimal expansion term.

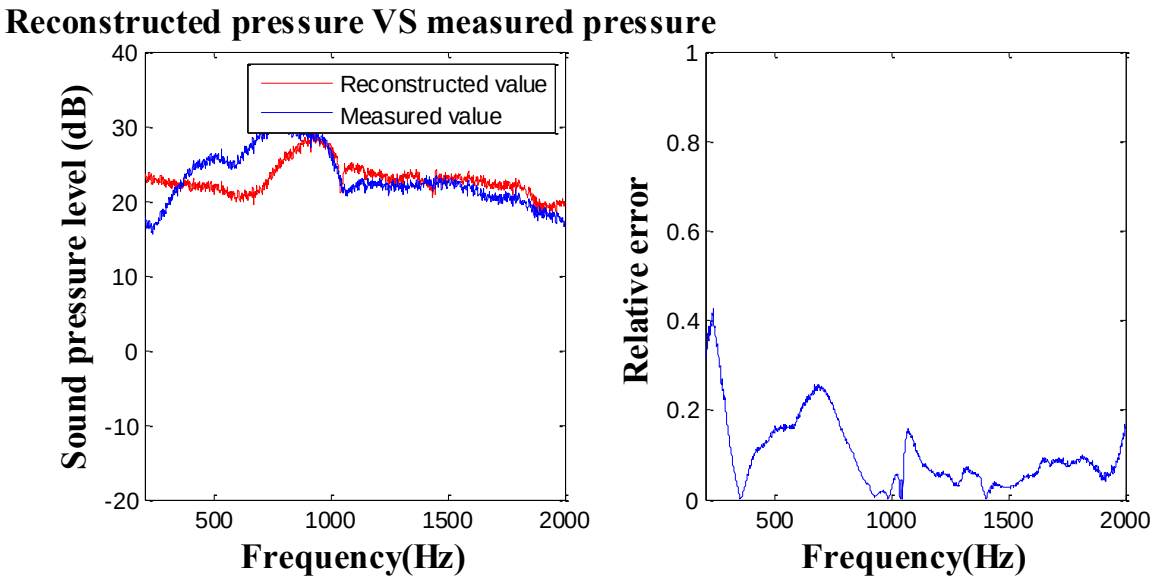

Figure 6.9 Analysis of reconstructed acoustic pressure at node 1 on m2 surface

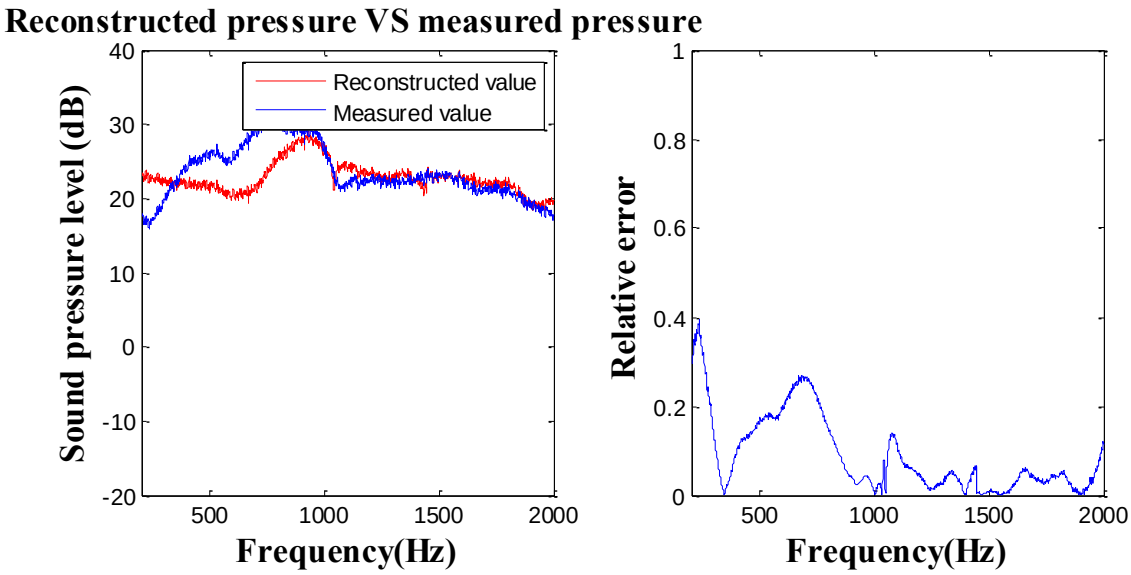

Figure 6.10 Analysis of reconstructed acoustic pressure at node 2 on m2 surface

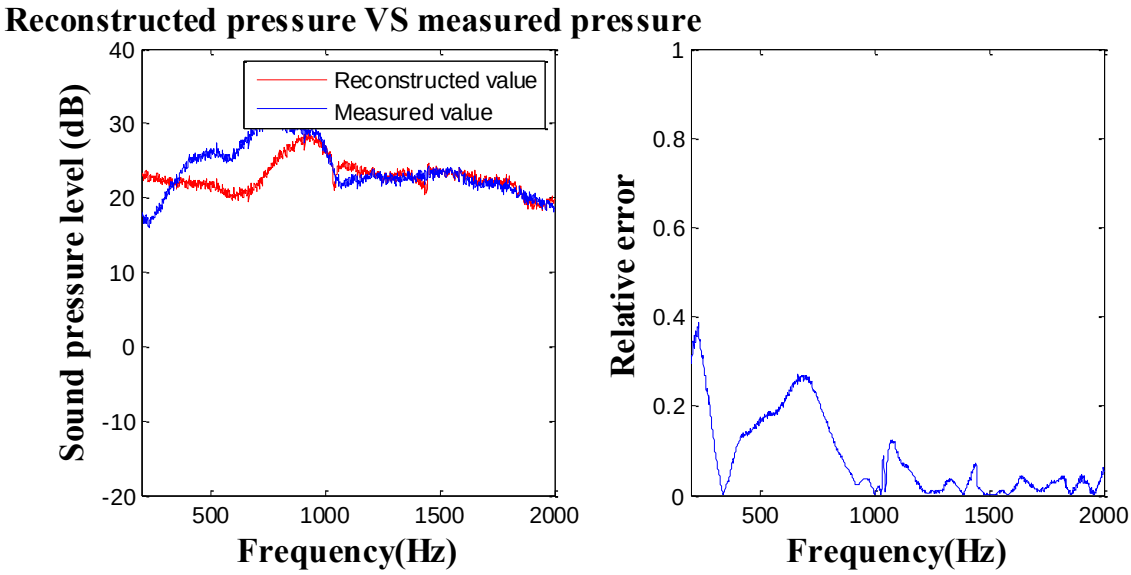

Figure 6.11 Analysis of reconstructed acoustic pressure at node 3 on m2 surface

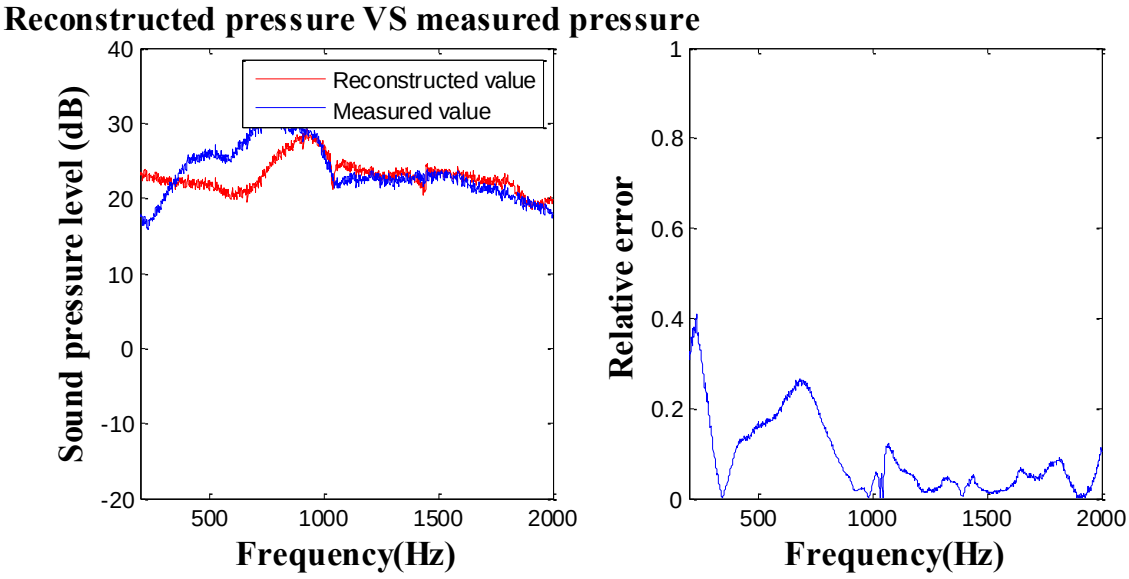

Figure 6.12 Analysis of reconstructed acoustic pressure at node 4 on m2 surface

By way of comparing the reconstructed sound pressure with the measured sound pressure, the optimal expansion terms have been decided in each frequency. Therefore, the sound pressure at reconstruction surface could be obtained by applying the modified HELS based NAH with laser.

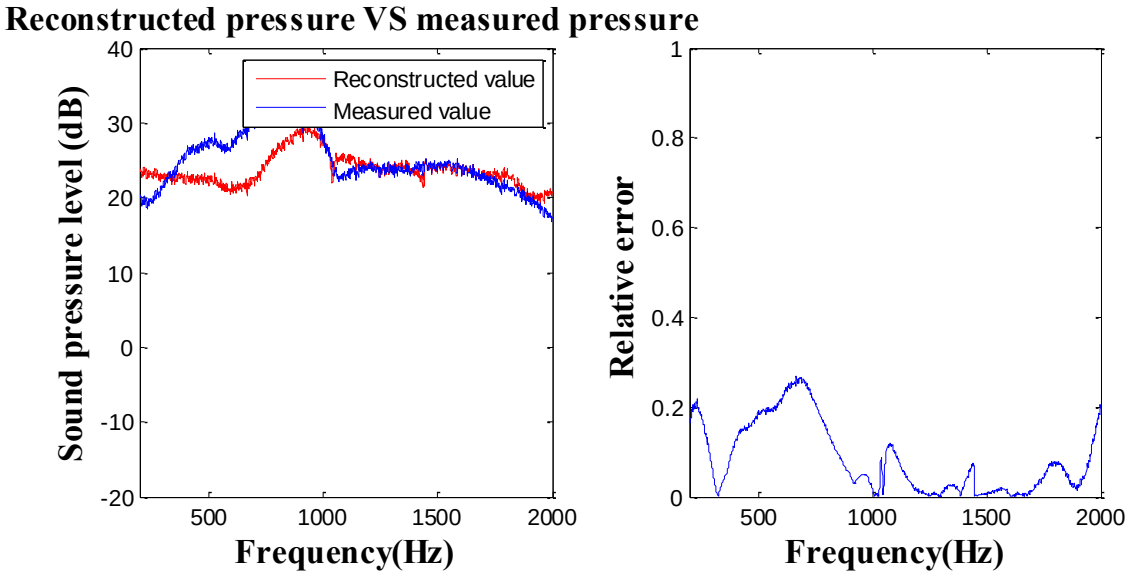

Figure 6.13 Analysis of reconstructed acoustic pressure at node 1 on reconstruction surface

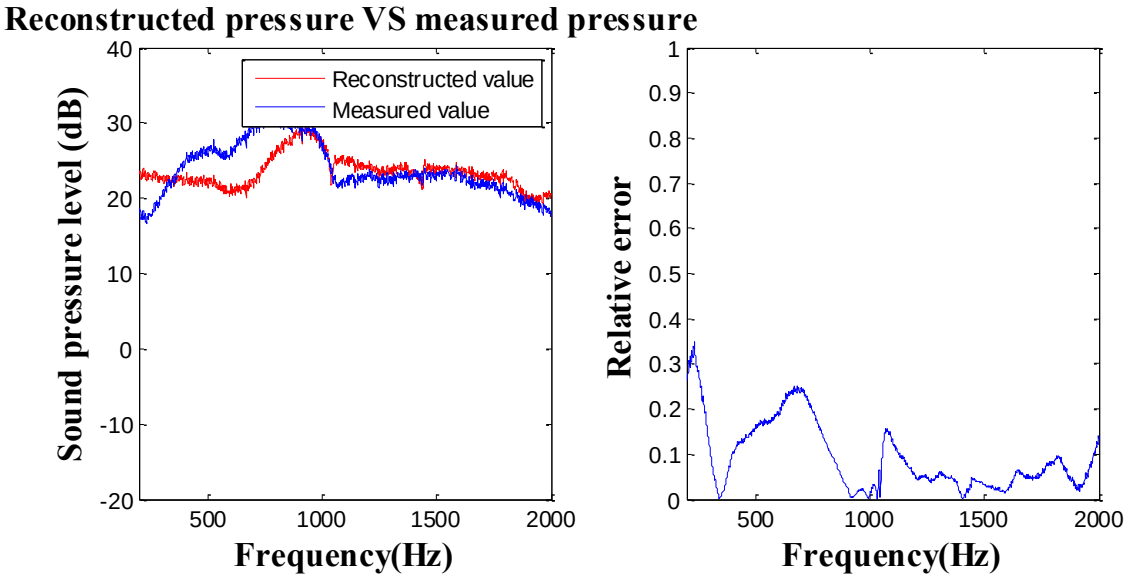

Figure 6.14 Analysis of reconstructed acoustic pressure at node 2 on reconstruction surface

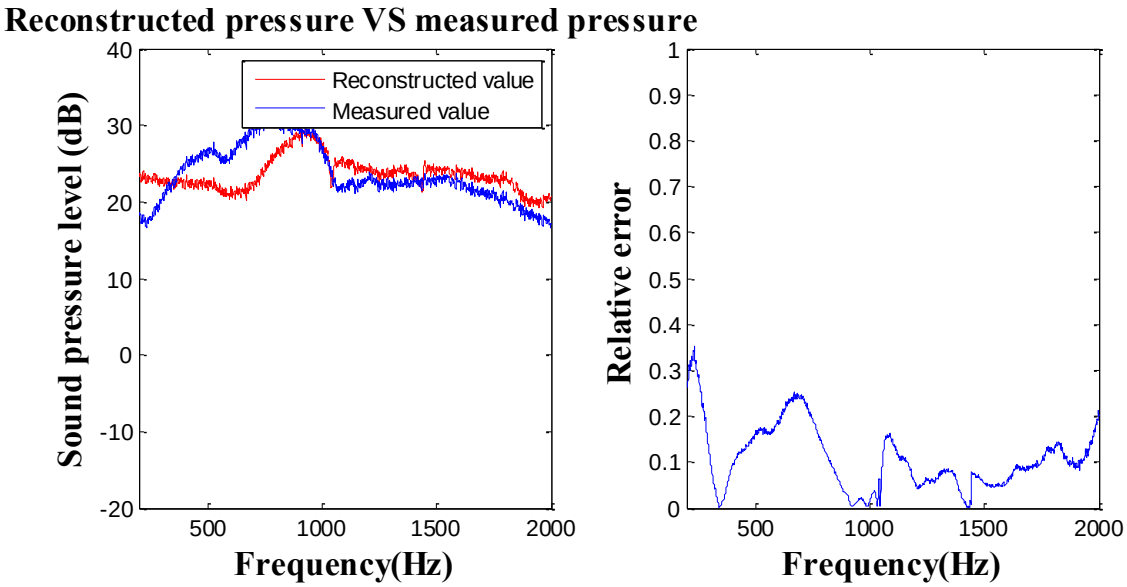

Figure 6.15 Analysis of reconstructed acoustic pressure at node 3 on reconstruction surface

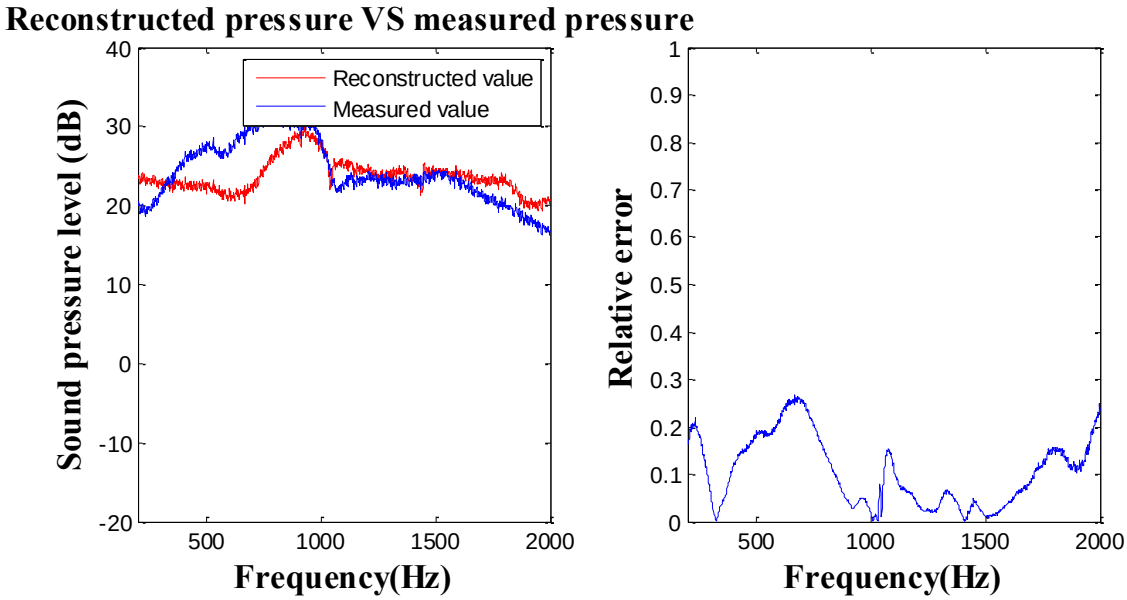

Figure 6.16 Analysis of reconstructed acoustic pressure at node 4 on reconstruction surface

As shown from figure 6.13 to 6.16, HELS based NAH with laser demonstrates its ability in reconstructing sound pressure based on normal surface velocity input. Especially for sound pressure at the frequency range from 800 Hz to 1800 Hz, the relative errors between reconstructed sound pressure and measured values are much smaller than 10%. However, the accuracy of reconstruction deteriorates at low frequency range. The root cause is that the background noise is mainly in low frequency, and the measured sound pressure is polluted by the background noise. Meanwhile, the reconstructed sound pressure using HELS based NAH with laser has contained all the near-field information. While, the benchmark microphones are incapable of capturing all the evanescent waves. It turns out that large discrepancy exists in low frequency range.

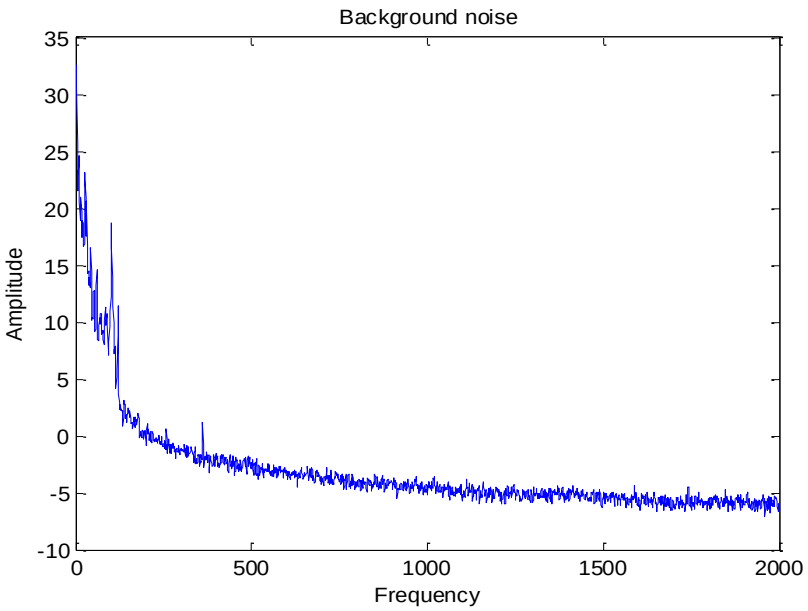

Figure 6.17 Background noise

CHAPTER 7

CONCLUSIONS AND FUTURE WORK

7.1 Conclusions

In this chapter, a brief summary of the work in this thesis is presented. Meanwhile the possible developments and research directions of the HELS based NAH with laser are discussed.

The primary purpose of this thesis is to develop the HELS based NAH with laser and use normal surface velocity as input in near-field acoustic holography. The conventional HELS based NAH uses acoustic pressure as input to reconstruct sound field quantities, while this modified HELS based NAH with laser utilizes the normal surface velocities measured by LDV to reconstruct the acoustic quantities at interested positions. The main differences between this new-created method and conventional NAH methods have been summed up as: 1. the transfer function of this HELS based NAH with laser contains both the basis functions and their normal derivatives, while the conventional NAH methods only employs the basis functions; 2. the HELS based NAH with laser uses the normal surface velocities measured directly on the source surface by a LDV, therefore the input data includes all the necessary near field information for an accurate reconstruction of sound field, while the conventional NAH methods use the acoustic pressure as input.

Theoretical principles of the HELS based NAH with laser have been fully developed and the method has been verified in theoretical perspective. Two theoretical examples of a dilating sphere and an oscillating sphere have been studied. The reconstructed acoustic pressure using HELS based NAH with laser is exactly the same as analytic solution. Moreover, an in-depth examination has been conducted to study the impacts of the errors imbedded in measured normal

surface velocities on the resultant reconstructed acoustic pressure. The error analysis shows that the magnitudes of errors are bounded and the HELS based NAH with laser is robust and reliable.

Numerical simulations have been conducted on ideal sound sources including a monopole and a dipole. The accuracy of reconstruction is verified in different conditions. It turns out that HELS based NAH with laser is capable of reconstructing sound field in a highly accurate manner. Another numerical study has been conducted on some special cases of a transverse vibration problem of thin plates. The reconstructed sound pressure field is compared with the theoretical sound pressure values, and it testifies that HELS based NAH with laser is also applicable to complex sound sources.

Experimental validation was finished by reconstructing acoustic pressure generated by a subwoofer. A LDV was employed to measure the normal surface velocity at seven measurement points on the subwoofer surface. We also discussed the working theory of LDV. Through comparing the reconstructed sound pressure at 4 different positions with measured values from microphones, it demonstrates that the HELS based NAH with laser demonstrates succeed in reconstructing sound pressure based on normal surface velocity input. In the frequency range from 800 Hz to 1800 Hz, the relative errors between reconstructed sound pressure and measured values are smaller than 10%. Therefore, HELS based NAH with laser is effective and efficient in acoustic pressure reconstruction using normal surface velocity as input data.

This HELS based NAH with laser is advantageous in following reasons:

(1) Since HELS based NAH with laser is developed from conventional HELS method, it has the same characteristics ranging from mathematically rigorous, uniqueness of solutions to high efficiency of numerical computations;

(2) It enables one to collect input data in the far field. LDV does not require the measuring laser head placed close to the source and then offers non-intrusive vibration measurements;

(3) Measurement setup is very simple. LDV with a positioning system that allows the laser beam to move from one measuring point to another position at a very quick pace. Moreover, LDV is able to measure the normal surface velocity in a no-contact manner, then conformal array is not necessary in this case. Therefore, the measurement procedure could be finished in a short time period even for a large structure with complex shape;

(4) The normal surface velocity contains all near-field information for reconstruction of an acoustic field. The acoustic field in three-dimensional space can be reconstructed with a high level of accuracy;

(5) This modified HELS method is applicable to both exterior and interior problems. The measurements of sound velocity will not contaminated by echo. For interior problems, HELS based NAH with laser is a perfect alternative for conventional HELS or other NAH methods.

7.2 Future work

Future effort could be put on several directions:

1. In this dissertation, a simple sound source was used to verify the modified HELS method based on laser. The modified HELS method can be applied on more complex sound sources or even realistic NVH problems.

2. There were only a few surface velocity measurements in the experiment. For complex sound sources or large measurement apertures, more measurements are necessary for an accurate reconstruction. Then, a more flexible and convenient positioning system need to be designed for

LDV. When normal surface velocity measurement can be finished in a fast and consistent way, smaller phase discrepancy will be expectable for input data. Therefore, HELS based NAH with laser can reproduce the sound field with better accuracy.

3. Patch HELS method is another direction to apply HELS method on complex sound source. In particular, the sound velocity measured over a finite number of positions. In order to extend the range of sound reconstruction out of the measurement aperture, an iterative patch HELS method is capable of extrapolating normal surface velocity data and increase the aperture size to successfully reconstruct the sound field over the whole sound source.

REFERENCES

1. Williams, E.G., J.D. Maynard, and E. Skudrzyk, Sound source reconstructions using a microphone array. The Journal of the Acoustical Society of America, 1980. **68**(1): p. 340-344.

2. Williams, E.G., H.D. Dardy, and R.G. Fink, Underwater-nearfield acoustical holography using a robotic controlled scanner. The Journal of the Acoustical Society of America, 1984. **75**(S1): p. S64-S64.

3. Williams, E.G., H.D. Dardy, and R.G. Fink, Nearfield acoustical holography using an underwater, automated scanner. The Journal of the Acoustical Society of America, 1985. **78**(2): p. 789-798.

4. Veronesi, W.A. and J.D. Maynard, Nearfield acoustic holography (NAH) II. Holographic reconstruction algorithms and computer implementation. The Journal of the Acoustical Society of America, 1987. **81**(5): p. 1307-1322.

5. Roozen, N., et al., New developments in near-field acoustic holography. 2007.

6. Wang, Z., et al. Approximate model of sound source in consideration of evanescent waves in far-field acoustical holography. in INTER-NOISE and NOISE-CON Congress and Conference Proceedings. 2014. Institute of Noise Control Engineering.

7. Goodman, R. and R. Bunney, Sound Intensity in Evanescent Waves. The Journal of the Acoustical Society of America, 1971. **49**(1A): p. 77-77.

8. Plotnick, D.S., T.M. Marston, and P.L. Marston, Comparisons of evanescent wave and propagating wave scattering based on circular synthetic aperture sonar and spectroscopy. The Journal of the Acoustical Society of America, 2011. **129**(4): p. 2686-2686.

9. Alippi, A., et al., Propagation features of evanescent acoustic waves. the Journal of the Acoustical Society of America, 1999. **105**(2): p. 1147-1147.

10. Russell, D.A. and D.O. Ludwigsen, Apparatus for demonstrating evanescent waves in acoustic waveguides. The Journal of the Acoustical Society of America, 2014. **135**(4): p. 2249-2249.

11. Lin, D. and A. Powell, Choked jet edge tones, continued again: Scattering of evanescent waves as the sound source. The Journal of the Acoustical Society of America, 1992. **92**(4): p. 2309-2309.

12. Williams, E.G., Fourier acoustics: sound radiation and nearfield acoustical holography. 1999: Academic press.

13. Wang, Z. and S.F. Wu, Helmholtz equation–least-squares method for reconstructing the acoustic pressure field. The Journal of the Acoustical Society of America, 1997. **102**(4): p. 2020-2032.

14. Wall, A.T., K.L. Gee, and T.B. Neilsen, Multisource statistically optimized near-field acoustical holography. The Journal of the Acoustical Society of America, 2015. **137**(2): p. 963-975.

15. Semenova, T. and S.F. Wu, The Helmholtz equation least-squares method and Rayleigh hypothesis in near-field acoustical holography. The Journal of the Acoustical Society of America, 2004. **115**(4): p. 1632-1640.

16. Castellini, P., M. Martarelli, and E.P. Tomasini, Laser Doppler Vibrometry: Development of advanced solutions answering to technology's needs. Mechanical Systems and Signal Processing, 2006. **20**(6): p. 1265-1285.

17. Castellini, P., G. Revel, and E. Tomasini, Laser Doppler vibrometry: a review of advances and applications. The Shock and vibration digest, 1998. **30**(6): p. 443-456.

18. Esposito, E., Laser Doppler Vibrometry. Handbook of the Use of Lasers in Conservation and Conservation Science, 2008.

19. Jeong, T.H., Basic principles and applications of holography. Lake Forest College, Lake Forest, llinois, 1999.

20. Williams, E.G. and J.D. Maynard, Holographic Imaging without the Wavelength Resolution Limit. Physical Review Letters, 1980. **45**(7): p. 554-557.

21. Williams, E.G. and J.D. Maynard, Numerical evaluation of the Rayleigh integral for planar radiators using the FFT. The Journal of the Acoustical Society of America, 1982. **72**(6): p. 2020-2030.

22. Maynard, J.D., E.G. Williams, and Y. Lee, Nearfield acoustic holography: I. Theory of generalized holography and the development of NAH. The Journal of the Acoustical Society of America, 1985. **78**(4): p. 1395-1413.

23. Williams, E.G., H.D. Dardy, and K.B. Washburn, Generalized nearfield acoustical holography for cylindrical geometry: Theory and experiment. The Journal of the Acoustical Society of America, 1987. **81**(2): p. 389-407.

24. Williams, E.G., B.H. Houston, and J.A. Bucaro, Broadband nearfield acoustical holography for vibrating cylinders. The Journal of the Acoustical Society of America, 1989. **86**(2): p. 674-679.

25. Lee, M., J.S. Bolton, and L. Mongeau, Application of cylindrical near-field acoustical holography to the visualization of aeroacoustic sources. The Journal of the Acoustical Society of America, 2003. **114**(2): p. 842-858.

26. Borgiotti, G.V., et al., Conformal generalized near-field acoustic holography for axisymmetric geometries. The Journal of the Acoustical Society of America, 1990. **88**(1): p. 199-209.

27. Mann, J.A., et al., Time-domain analysis of the energy exchange between structural vibrations and acoustic radiation using near-field acoustical holography measurements. The Journal of the Acoustical Society of America, 1991. **90**(3): p. 1656-1664.

28. Tomlinson, M.A., Partial source discrimination in near field acoustic holography. Applied Acoustics, 1999. **57**(3): p. 243-261.

29. Nam, K.-U. and Y.-H. Kim, Visualization of multiple incoherent sources by the backward prediction of near-field acoustic holography. The Journal of the Acoustical Society of America, 2001. **109**(5): p. 1808-1816.

30. Ruhala, R.J. and D.C. Swanson, Planar near-field acoustical holography in a moving medium. The Journal of the Acoustical Society of America, 2002. **112**(2): p. 420-429.

31. Lee, J.C., Spherical acoustical holography of low-frequency noise sources. Applied Acoustics, 1996. **48**(1): p. 85-95.

32. Devries, L.A. and J.S. Bolton, Acoustical holography in spherical coordinates for noise source identification. The Journal of the Acoustical Society of America, 1994. **95**(5): p. 2921-2921.

33. Hayek, S.I. and T.W. Luce, Aperture Effects in Planar Nearfield Acoustical Imaging. Journal of Vibration, Acoustics, Stress, and Reliability in Design, 1988. **110**(1): p. 91-96.

34. Williams, E.G., B.H. Houston, and P.C. Herdic, Fast Fourier transform and singular value decomposition formulations for patch nearfield acoustical holography. The Journal of the Acoustical Society of America, 2003. **114**(3): p. 1322-1333.

35. Sarkissian, A., Extension of measurement surface in near-field acoustic holography. The Journal of the Acoustical Society of America, 2004. **115**(4): p. 1593-1596.

36. Sarkissian, A., Method of superposition applied to patch near-field acoustic holography. The Journal of the Acoustical Society of America, 2005. **118**(2): p. 671-678.

37. Lee, M. and J.S. Bolton, Patch near-field acoustical holography in cylindrical geometry. The Journal of the Acoustical Society of America, 2005. **118**(6): p. 3721-3732.

38. Wu, S.F., Techniques for implementing near-field acoustical holography. Sound and Vibration, 2010. **44**(2): p. 12.

39. Wu, S.F., Transient sound radiation from impulsively accelerated bodies. The Journal of the Acoustical Society of America, 1993. **94**(1): p. 542-553.

40. Wu, S.F. and J. Yu, Reconstructing interior acoustic pressure fields via Helmholtz equation least-squares method. The Journal of the Acoustical Society of America, 1998. **104**(4): p. 2054-2060.

41. Rayess, N. and S.F. Wu, Experimental validations of the HELS method for reconstructing acoustic radiation from a complex vibrating structure. The Journal of the Acoustical Society of America, 2000. **107**(6): p. 2955-2964.

42. Wu, S.F., On reconstruction of acoustic pressure fields using the Helmholtz equation least squares method. The Journal of the Acoustical Society of America, 2000. **107**(5): p. 2511-2522.

43. Semenova, T. and S.F. Wu, On the choice of expansion functions in the Helmholtz equation least-squares method. The Journal of the Acoustical Society of America, 2005. **117**(2): p. 701-710.

44. Wu, S. and X. Zhao, Combined Helmholtz equation–least squares (CHELS) method for reconstructing radiated acoustic pressure fields. The Journal of the Acoustical Society of America, 2000. **107**(5): p. 2799-2799.

45. Isakov, V. and S.F. Wu, On theory and application of the Helmholtz equation least squares method in inverse acoustics. Inverse Problems, 2002. **18**(4): p. 1147.

46. Zhao, X. and S.F. Wu, Reconstruction of vibro-acoustic fields using hybrid nearfield acoustic holography. Journal of Sound and Vibration, 2005. **282**(3–5): p. 1183-1199.

47. Wu, S.F., Hybrid near-field acoustic holography. The Journal of the Acoustical Society of America, 2004. **115**(1): p. 207-217.

48. Zhao, X. and S.F. Wu, Reconstruction of vibroacoustic fields in half-space by using hybrid near-field acoustical holography. The Journal of the Acoustical Society of America, 2005. **117**(2): p. 555-565.

49. Moondra, M.S. and S.F. Wu, Visualization of vehicle interior sound field using Nearfield Acoustical Holography based on the Helmholtz-Equation Least-Squares (HELS) method. Noise Control Engineering Journal, 2005. **53**(4): p. 145-154.

50. Lu, H. and S.F. Wu, Reconstruction of vibroacoustic responses of a highly nonspherical structure using Helmholtz equation least-squares method. The Journal of the Acoustical Society of America, 2009. **125**(3): p. 1538-1548.

51. Natarajan, L.M., S.;Wu, S., Reconstruction of Vibro-Acoustic Responses of a Complex Vibrating Structure Using Helmholtz Equation Least Squares. SAE Technical Paper, 2011. **1670**(01).

52. LU, H., S.F. WU, and D.B. KEELE, RECONSTRUCTING ACOUSTIC RADIATION PATTERNS OF AN ELONGATED, BAFFLED PLATE AT HIGH FREQUENCIES WITH THE NYQUIST SPATIAL SAMPLING RATE SIGNIFICANTLY RELAXED. Journal of Computational Acoustics, 2012. **20**(04): p. 1250015.

53. Wu, S.F. and L. Kumar Natarajan, Panel acoustic contribution analysis. The Journal of the Acoustical Society of America, 2013. **133**(2): p. 799-809.

54. Natarajan, L.K. and S.F. Wu, Reconstructing the vibro-acoustic quantities on a highly non-spherical surface using the Helmholtz equation least squares method. The Journal of the Acoustical Society of America, 2012. **131**(6): p. 4570-4583.

55. de Bree, H.-E., et al., The μ-flown: a novel device for measuring acoustic flows. Sensors and Actuators A: Physical, 1996. **54**(1): p. 552-557.

56. Bree, H.-E., et al., The μ-flown: A Novel Device Measuring Acoustical Flows. 1995.

57. de Bree, H.-E., An overview of microflown technologies. Acta acustica united with Acustica, 2003. **89**(1): p. 163-172.

58. Lanoye, R., et al., a practical device to determine the reflection coefficient of acoustic materials in-situ based on a Microflown and microphone sensor. ISMA, Leuven, 2004.

59. Van Der Eerden, F., H. De Bree, and H. Tijdeman, Experiments with a new acoustic particle velocity sensor in an impedance tube. Sensors and Actuators A: Physical, 1998. **69**(2): p. 126-133.

60. Jacobsen, F. and Y. Liu, Near field acoustic holography with particle velocity transducersa). The Journal of the Acoustical Society of America, 2005. **118**(5): p. 3139-3144.

61. Liu, Y. and F. Jacobsen, Measurement of absorption with a pu sound intensity probe in an impedance tube. The Journal of the Acoustical Society of America, 2005. **118**(4): p. 2117-2120.

62. Jacobsen, F. and V. Jaud, A note on the calibration of pressure-velocity sound intensity probesa). The Journal of the Acoustical Society of America, 2006. **120**(2): p. 830-837.

63. Jacobsen, F., X. Chen, and V. Jaud, A comparison of statistically optimized near field acoustic holography using single layer pressure-velocity measurements and using double layer pressure measurementsa). The Journal of the Acoustical Society of America, 2008. **123**(4): p. 1842-1845.

64. de Bree, H.-E. and T. Basten. A full bandwidth calibrator for a sound pressure and particle velocity sensor. in German Annual Conference on Acoustics. 2008.

65. Zhang, Y.-B., et al., Near field acoustic holography based on the equivalent source method and pressure-velocity transducers. The Journal of the Acoustical Society of America, 2009. **126**(3): p. 1257-1263.

66. Zhang, Y.-B., X.-Z. Chen, and F. Jacobsen, A sound field separation technique based on measurements with pressure-velocity probes. The Journal of the Acoustical Society of America, 2009. **125**(6): p. 3518-3521.

67. Zhang, Y.-B., et al., Patch near field acoustic holography based on particle velocity measurements. The Journal of the Acoustical Society of America, 2009. **126**(2): p. 721-727.

68. Fernandez Comesana, D., Cereijo Grana, Iban and Grosso, Andrea, Particle velocity sensors for enhancing vehicle simulations. AIA-DAGA 2013 Merano, 2013: p. 18-21.

69. Wu, S.F., Advanced Acoustic Radiation (ME7460 Course Pack Part II HELS Theory. Wayne State University, Winter 2005.

70. Pierce, A.D., Acoustics: an introduction to its physical principles and applications. 1991: Acoustical Society of America Melville, NY.

71. Russell, D.A., J.P. Titlow, and Y.-J. Bemmen, Acoustic monopoles, dipoles, and quadrupoles: An experiment revisited. American Journal of Physics, 1999. **67**(8): p. 660-664.

72. Kirkup, S., et al. Fortran codes for computing the acoustic field surrounding a vibrating plate by the Rayleigh integral method. in WSEAS International Conference. Proceedings. Mathematics and Computers in Science and Engineering. 2008. WSEAS.

73. Kim, G.T. and B.H. Lee, 3-D sound source reconstruction and field reprediction using the Helmholtz integral equation. Journal of Sound and Vibration, 1990. **136**(2): p. 245-261.

74. Morse, P.M. and K.U. Ingard, Theoretical acoustics. 1968: Princeton university press.

75. Jacobsen, F. and P. Juhl, Radiation of sound. DTU, Lyngby, 2010.

76. Ventsel, E. and T. Krauthammer, Thin plates and shells: theory: analysis, and applications. 2001: CRC press.

77. Kirkup, S., Computational solution of the acoustic field surrounding a baffled panel by the Rayleigh integral method. Applied mathematical modelling, 1994. **18**(7): p. 403-407.

78. van Engelen, A., Sound radiation of a baffled plate; theoretical and numerical approach. Eindhoven University of Technology, Eindhoven, The Netherlands, Research Report No. DCT, 2009.

79. Mindlin, R.D., et al., An introduction to the mathematical theory of vibrations of elastic plates. 2006: World Scientific.

80. Currey, M.N. and K.A. Cunefare, The radiation modes of baffled finite plates. The Journal of the Acoustical Society of America, 1995. **98**(3): p. 1570-1580.

81. Seybert, A., D. Hamilton, and P. Hayes, Prediction of radiated noise from engine components using the BEM and the rayleigh integral. 1997, SAE Technical Paper.

82. Williams, E.G., Regularization methods for near-field acoustical holography. The Journal of the Acoustical Society of America, 2001. **110**(4): p. 1976-1988.

83. Williams, E.G., Regularization of inverse problems with evanescent waves. The Journal of the Acoustical Society of America, 2000. **108**(5): p. 2503-2503.

84. Tarantola, A., Inverse problem theory and methods for model parameter estimation. 2005: siam.

85. Colton, D. and B. Sleeman, Uniqueness theorems for the inverse problem of acoustic scattering. IMA journal of applied mathematics, 1983. **31**(3): p. 253-259.

86. Majda, A., High frequency asymptotics for the scattering matrix and the inverse problem of acoustical scattering. Communications on Pure and Applied Mathematics, 1976. **29**(3): p. 261-291.

87. Xiang, H. and J. Zou, Regularization with randomized SVD for large-scale discrete inverse problems. Inverse Problems, 2013. **29**(8): p. 085008.

88. Maciejewski, A.A. and C.A. Klein, The singular value decomposition: Computation and applications to robotics. The International journal of robotics research, 1989. **8**(6): p. 63-79.

89. Klema, V.C. and A.J. Laub, The singular value decomposition: Its computation and some applications. Automatic Control, IEEE Transactions on, 1980. **25**(2): p. 164-176.

90. Hansen, P.C., The discrete picard condition of discrete ill-posed problems. BIT, 1990. **30**(4): p. 658-672.

91. Hansen, P.C., Discrete inverse problems: insight and algorithms. Vol. 7. 2010: Siam.

92. Hansen, P., The truncatedSVD as a method for regularization. BIT Numerical Mathematics, 1987. **27**(4): p. 534-553.

93. Hansen, P.C., Truncated Singular Value Decomposition Solutions to Discrete Ill-Posed Problems with Ill-Determined Numerical Rank. SIAM Journal on Scientific and Statistical Computing, 1990. **11**(3): p. 503-518.

94. Hansen, P.C., T. Sekii, and H. Shibahashi, The Modified Truncated SVD Method for Regularization in General Form. SIAM Journal on Scientific and Statistical Computing, 1992. **13**(5): p. 1142-1150.

95. Golub, G.H., P.C. Hansen, and D.P. O'Leary, Tikhonov regularization and total least squares. SIAM Journal on Matrix Analysis and Applications, 1999. **21**(1): p. 185-194.

96. Hansen, P., REGULARIZATION TOOLS: A Matlab package for analysis and solution of discrete ill-posed problems. Numerical Algorithms, 1994. **6**(1): p. 1-35.

97. Espanol, M.I. and M.E. Kilmer, Multilevel approach for signal restoration problems with Toeplitz matrices. SIAM Journal on Scientific Computing, 2010. **32**(1): p. 299-319.

98. Espanol, M.I., Multilevel methods for discrete ill-posed problems: application to deblurring. 2009, TUFTS UNIVERSITY.

99. Sriram, P., J. Craig, and S. Hanagud, A scanning laser Doppler vibrometer for modal testing. International Journal of Analytical and Experimental Modal Analysis;(USA), 1990. **5**.

100. Stasche, N., et al., Middle ear transmission disorders-tympanic membrane vibration analysis by laser-Doppler-vibrometry. Acta oto-laryngologica, 1994. **114**(1): p. 59-63.

101. Roos, P., M. Stephens, and C. Wieman, Laser vibrometer based on optical-feedback-induced frequency modulation of a single-mode laser diode. Applied optics, 1996. **35**(34): p. 6754-6761.

102. Ball, G., A. Huber, and R. Goode, Scanning laser Doppler vibrometry of the middle ear ossicles. Ear, nose, & throat journal, 1997. **76**(4): p. 213-8, 220, 222.

103. Stanbridge, A. and D. Ewins, Modal testing using a scanning laser Doppler vibrometer. Mechanical Systems and Signal Processing, 1999. **13**(2): p. 255-270.

104. Bell, J.R. and S. Rothberg, Rotational vibration measurements using laser Doppler vibrometry: comprehensive theory and practical application. Journal of Sound and Vibration, 2000. **238**(4): p. 673-690.

105. Scalise, L. and N. Paone, Laser Doppler vibrometry based on self-mixing effect. Optics and lasers in Engineering, 2002. **38**(3): p. 173-184.

106. Sracic, M.W., A new experimental modal analysis method using continuous scan laser doppler vibrometry and impact excitation. 2008, UNIVERSITY OF WISCONSIN-MADISON.

107. Potter, J.L., Comparison of modal analysis results of laser vibrometry and nearfield acoustical holography measurements of an aluminum plate. The Journal of the Acoustical Society of America, 2011. **129**(4): p. 2491-2491.

108. Polytec, Laser Doppler Vibrometer User Manual. p. 61-65.

ABSTRACT

HELMHOLTZ EQUATION LEAST SQUARES BASED NEAR-FIELD ACOUSTIC HOLOGRAPHY WITH LASER

by

WU ZHU

December 2015

Advisor: Dr. Sean F. Wu

Major: Mechanical Engineering

Degree: Doctor of Philosophy

This dissertation presents an innovative NAH approach: HELS based NAH with laser. The conventional HELS based NAH uses acoustic pressure as input to reconstruct sound field quantities, while HELS based NAH with laser utilizes the normal surface velocities measured by LDV to reconstruct the acoustic quantities at interested positions. Theoretical principles of the HELS based NAH with laser have been fully developed and the method has been verified in theoretical perspective. Two theoretical examples verify that HELS based NAH with laser can obtain exactly the same results as analytic solutions. Meanwhile, the error analysis demonstrates that errors of sound field reconstruction are bounded and the HELS based NAH with laser is robust and reliable.

Numerical simulations have been conducted on ideal sound sources including monopole and dipole sound sources. Another numerical study has been conducted on sound field radiated by the transverse vibration of thin plates. The reconstructed acoustic field quantities are compared with the theoretical values, and it testifies that HELS based NAH with laser is

applicable to both ideal sound sources and complex sound sources. Experimental validation is investigated by reconstructing acoustic pressure generated by a subwoofer. Through comparing the reconstructed sound pressure with measured values from microphones, it demonstrates that the HELS based NAH with laser is able to reconstruct sound pressure based on normal surface velocity with a highly accuracy. This HELS based NAH with laser is testified to improve the efficiency and broaden the application range of NAH methods.

AUTOBIOGRAPHICAL STATEMENT

WU ZHU

EDUCATION

2011-present Ph.D. of Mechanical Engineering; Wayne State University, Detroit, MI

2008-2011 Master of Mechanical Engineering, Hunan University, Changsha, China

2004-2008 Bachelor of Automotive Engineering, Hunan University, Changsha, China

PUBLICATIONS

Wu Zhu and S. F. Wu, "Reconstruction acoustic field based on the normal surface velocity input data," presented at169th Meeting Acoustic Society of America, April 2015

S. F. Wu and W. Zhu, "Modified HELS method using normal surface velocity as input," in preparation

W. Zhu and S. F. Wu, "Simulation study and experimental validation of Modified HELS method based on laser," in preparation

SCHOLARSHIPS

2011-2012 University Graduate Research Fellowship

2012 Summer Research Scholarship

2014‐2015 Thomas C. Rumble University Graduate Fellowship